Detonation and hypersonics simulation with AMROC – Part I

Ralf Deiterding

Aerodynamics and Flight Mechanics Research Group
University of Southampton
Highfield Campus
Southampton SO17 1BJ, UK
Email: r.deiterding@soton.ac.uk

Xiamen
23rd July, 2019

Outline

Adaptive Cartesian finite volume methods
- Block-structured AMR with complex boundaries
- Parallelization approach

Combustion modeling
- Governing equations
- Finite volume schemes

Detonation simulation
- Shock induced combustion from projectile flight
- Thermal ignition
- Propagation of regular detonations in 2d
- Cellular structures in 3d and their ignition
- Detonation-boundary layer interaction

Summary
- Conclusions

Collaboration with

Detonations

- Bok Jik Lee (Gwangju Institute of Science and Technology, South Korea)
- Xiaodong Cai, Jiang Liang, Zhiyong Lin (National University of Defense Technology, Changsha)
- Jack Ziegler (now Northrop Grumman), Dale Pullin, Joe Shepherd (Graduate Aeronautical Laboratory, California Institute of Technology)
- Yong Sun, Matthias Ihme (Stanford University)

Hypersonics simulation

- Chay Atkins, Adriano Cerminara, Neil Sandham (University of Southampton)

Block-structured adaptive mesh refinement (SAMR)

For simplicity $\partial_t \mathbf{q}(x,y,t) + \partial_x \mathbf{f}(\mathbf{q}(x,y,t)) + \partial_y \mathbf{g}(\mathbf{q}(x,y,t)) = 0$

- Refined blocks overlay coarser ones
- Refinement in space *and time* by factor r_l [Berger and Colella, 1988]
- Block (aka patch) based data structures
- \+ Numerical scheme

$$\mathbf{Q}_{jk}^{n+1} = \mathbf{Q}_{jk}^{n} - \frac{\Delta t}{\Delta x}\left[\mathbf{F}_{j+\frac{1}{2},k} - \mathbf{F}_{j-\frac{1}{2},k}\right] - \frac{\Delta t}{\Delta y}\left[\mathbf{G}_{j,k+\frac{1}{2}} - \mathbf{G}_{j,k-\frac{1}{2}}\right]$$

only for single patch necessary

- \+ Efficient cache-reuse / vectorization possible
- \- Cluster-algorithm necessary
- Papers: [Deiterding, 2011a, Deiterding et al., 2009b, Deiterding et al., 2007]

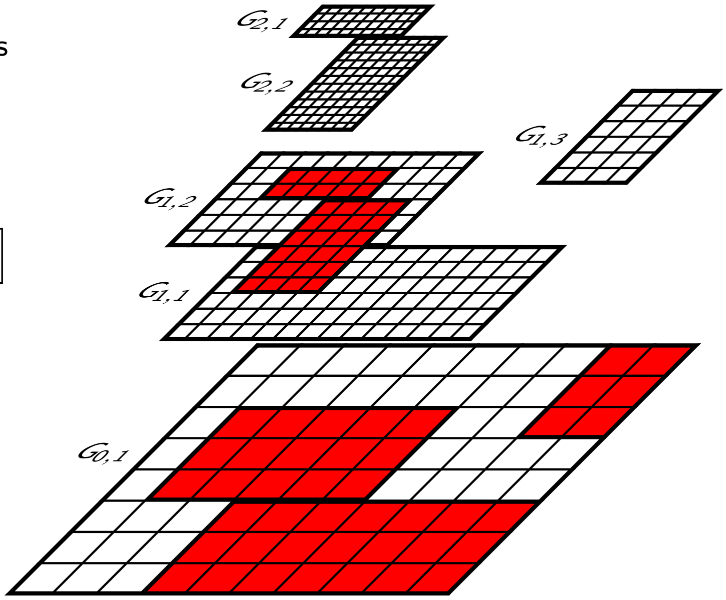

Level transfer / setting of ghost cells

Conservative averaging (restriction):

$$\hat{\mathbf{Q}}^{l}_{jk} := \frac{1}{(r_{l+1})^2} \sum_{\kappa=0}^{r_{l+1}-1} \sum_{\iota=0}^{r_{l+1}-1} \mathbf{Q}^{l+1}_{v+\kappa,w+\iota}$$

Bilinear interpolation (prolongation):

$$\check{\mathbf{Q}}^{l+1}_{vw} := (1-f_1)(1-f_2)\,\mathbf{Q}^{l}_{j-1,k-1} + f_1(1-f_2)\,\mathbf{Q}^{l}_{j,k-1} + (1-f_1)f_2\,\mathbf{Q}^{l}_{j-1,k} + f_1 f_2\,\mathbf{Q}^{l}_{jk}$$

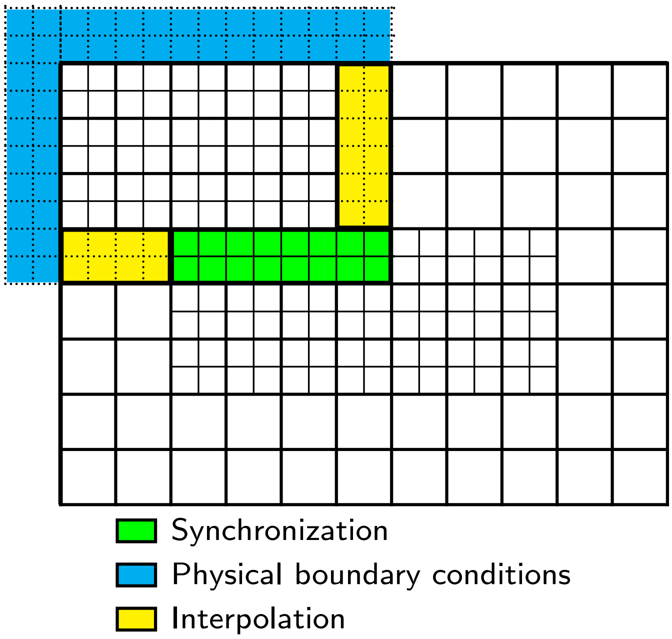

For boundary conditions: linear time interpolation

$$\tilde{\mathbf{Q}}^{l+1}(t+\kappa\Delta t_{l+1}) := \left(1-\frac{\kappa}{r_{l+1}}\right)\check{\mathbf{Q}}^{l+1}(t)+\frac{\kappa}{r_{l+1}}\check{\mathbf{Q}}^{l+1}(t+\Delta t_l) \quad \text{for } \kappa=0,\ldots r_{l+1}$$

Recursive integration order

- Space-time interpolation of coarse data to set I_l^s, $l > 0$
- Regridding:
  - Creation of new grids, copy existing cells on level $l > 0$
  - Spatial interpolation to initialize new cells on level $l > 0$

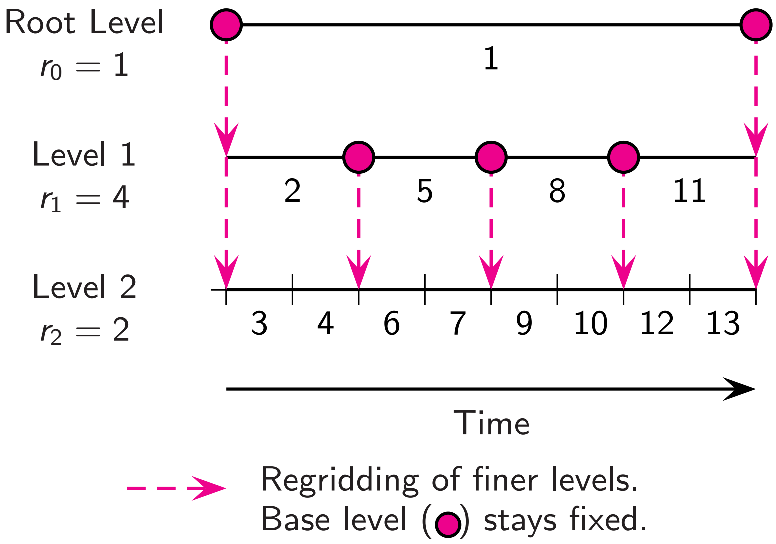

Conservative flux correction

Example: Cell j, k

$$\check{\mathbf{Q}}^l_{jk}(t+\Delta t_l) = \mathbf{Q}^l_{jk}(t) - \frac{\Delta t_l}{\Delta x_{1,l}} \left(\mathbf{F}^l_{j+\frac{1}{2},k} - \frac{1}{r^2_{l+1}} \sum_{\kappa=0}^{r_{l+1}-1} \sum_{\iota=0}^{r_{l+1}-1} \mathbf{F}^{l+1}_{v+\frac{1}{2},w+\iota}(t+\kappa\Delta t_{l+1}) \right) - \frac{\Delta t_l}{\Delta x_{2,l}} \left(\mathbf{G}^l_{j,k+\frac{1}{2}} - \mathbf{G}^l_{j,k-\frac{1}{2}} \right)$$

Correction pass:

1. $\delta\mathbf{F}^{l+1}_{j-\frac{1}{2},k} := -\mathbf{F}^l_{j-\frac{1}{2},k}$
2. $\delta\mathbf{F}^{l+1}_{j-\frac{1}{2},k} := \delta\mathbf{F}^{l+1}_{j-\frac{1}{2},k} + \frac{1}{r^2_{l+1}} \sum_{\iota=0}^{r_{l+1}-1} \mathbf{F}^{l+1}_{v+\frac{1}{2},w+\iota}(t+\kappa\Delta t_{l+1})$
3. $\check{\mathbf{Q}}^l_{jk}(t+\Delta t_l) := \mathbf{Q}^l_{jk}(t+\Delta t_l) + \frac{\Delta t_l}{\Delta x_{1,l}}\,\delta\mathbf{F}^{l+1}_{j-\frac{1}{2},k}$

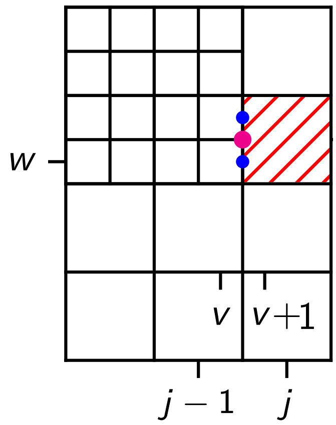

Level-set method for boundary embedding

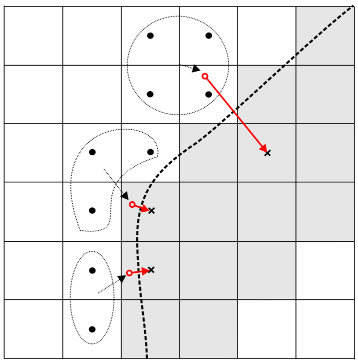

- Implicit boundary representation via distance function φ, normal $\mathbf{n} = \nabla\varphi/|\nabla\varphi|$
- Complex boundary moving with local velocity $\mathbf{w}$, treat interface as moving rigid wall [Deiterding et al., 2007]
- Construction of values in embedded boundary cells by interpolation / extrapolation [Deiterding, 2009, Deiterding, 2011a]
- Creation of level set from triangulated surface data with closest-point-transform (CPT) algorithm [Mauch, 2003, Deiterding et al., 2006]

Interpolate / constant value extrapolate values at

$$\tilde{\mathbf{x}} = \mathbf{x} + 2\varphi\mathbf{n}$$

Velocity in ghost cells (slip):

$$\mathbf{u}' = (2\mathbf{w}\cdot\mathbf{n} - \mathbf{u}\cdot\mathbf{n})\mathbf{n} + (\mathbf{u}\cdot\mathbf{t})\mathbf{t}$$
$$= 2\left((\mathbf{w}-\mathbf{u})\cdot\mathbf{n}\right)\mathbf{n} + \mathbf{u}$$

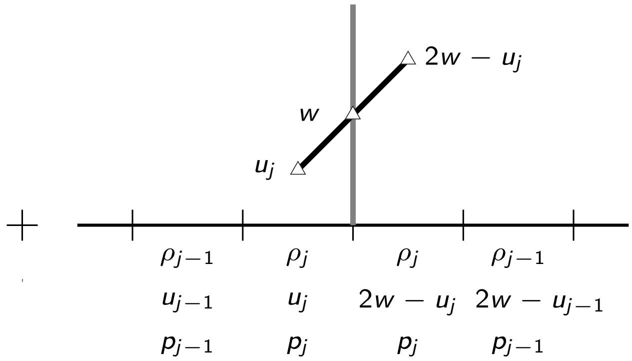

Parallelization

Rigorous domain decomposition

- Data of all levels resides on same node
- Grid hierarchy defines unique "floor-plan"
- Workload estimation

$$\mathcal{W}(\Omega) = \sum_{l=0}^{l_{\max}} \left[\mathcal{N}_l(G_l \cap \Omega) \prod_{\kappa=0}^{l} r_\kappa \right]$$

- Parallel operations
  - Synchronization of ghost cells
  - Redistribution of data blocks within regridding operation
  - Flux correction of coarse grid cells
- Dynamic partitioning with space-filling curve

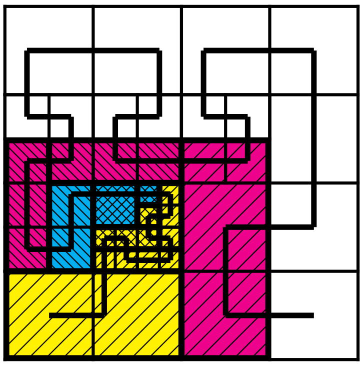

[Deiterding, 2005, Deiterding, 2011a]

AMROC framework and most important patch solvers

- Implements described algorithms and facilitates easy exchange of the block-based numerical scheme
- Shock-induced combustion with detailed chemistry: [Deiterding, 2003, Deiterding and Bader, 2005, Deiterding, 2011b, Cai et al., 2016, Cai et al., 2018]
- Hybrid WENO methods for LES and DNS: [Pantano et al., 2007, Lombardini and Deiterding, 2010, Ziegler et al., 2011, Cerminara et al., 2018]
- Lattice Boltzmann method for LES: [Fragner and Deiterding, 2016, Feldhusen et al., 2016, Deiterding and Wood, 2016]
- FSI deformation from water hammer: [Cirak et al., 2007, Deiterding et al., 2009a, Perotti et al., 2013, Wan et al., 2017]
- Level-set method for Eulerian solid mechanics: [Barton et al., 2013]
- Ideal magneto-hydrodynamics: [Gomes et al., 2015, Souza Lopes et al., 2018]
- $\sim 500,000$ LOC in C++, C, Fortran-77, Fortran-90
- V2.0 plus FSI coupling routines as open source at http://www.vtf.website
- Used here V3.0 with significantly enhanced parallelization (V2.1 not released)

AMROC strong scalability tests

3D wave propagation method with Roe scheme: spherical blast wave

- Tests run IBM BG/P (mode VN)

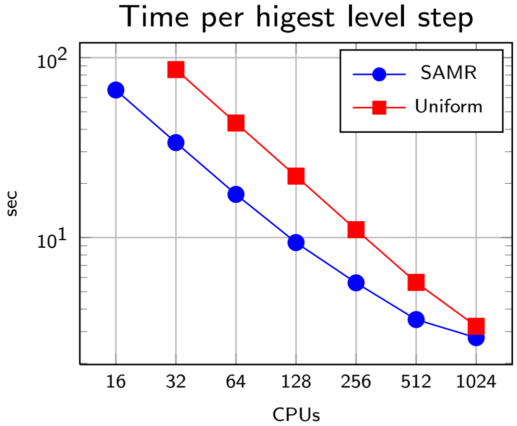

$64 \times 32 \times 32$ base grid, 2 additional levels with factors 2, 4; uniform $512 \times 256 \times 256 = 33.6 \cdot 10^6$ cells

Level	Grids	Cells
0	1709	65,536
1	1735	271,048
2	2210	7,190,208

3D SRT-lattice Boltzmann scheme: flow over rough surface of $19 \times 13 \times 2$ spheres

- Tests run Cray XC30m (Archer)

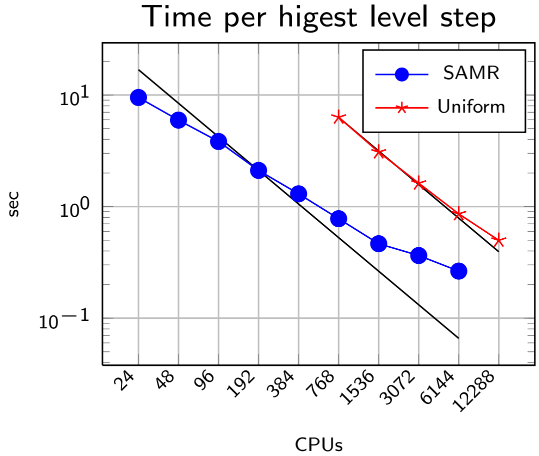

$360 \times 240 \times 108$ base grid, 2 additional levels with factors 2, 4; uniform $1440 \times 1920 \times 432 = 1.19 \cdot 10^9$ cells

Level	Grids	Cells
0	788	9,331,200
1	21367	24,844,504
2	1728	10,838,016

Axisymmetric Navier-Stokes equations with chemical reaction

$$\frac{\partial \mathbf{q}}{\partial t} + \frac{\partial(\mathbf{f}-\mathbf{f}_v)}{\partial x} + \frac{\partial(\mathbf{g}-\mathbf{g}_v)}{\partial y} = \frac{\alpha}{y}(\mathbf{c}-\mathbf{g}+\mathbf{g}_v) + \mathbf{s}$$

$$\mathbf{q} = \begin{bmatrix} \rho_i \\ \rho u \\ \rho v \\ \rho E \end{bmatrix}, \quad \mathbf{f} = \begin{bmatrix} \rho_i u \\ \rho u^2 + p \\ \rho u v \\ u(\rho E + p) \end{bmatrix}, \quad \mathbf{g} = \begin{bmatrix} \rho_i v \\ \rho u v \\ \rho v^2 + p \\ v(\rho E + p) \end{bmatrix}, \quad \mathbf{c} = \begin{bmatrix} 0 \\ 0 \\ p - \tau_{\theta\theta} \\ 0 \end{bmatrix}, \quad \mathbf{s} = \begin{bmatrix} \dot{\omega}_i \\ 0 \\ 0 \\ 0 \end{bmatrix}$$

$$\mathbf{f}_v = \begin{bmatrix} \rho D_i \dfrac{\partial Y_i}{\partial x} \\ \tau_{xx} \\ \tau_{xy} \\ k\dfrac{\partial T}{\partial x} + \rho \sum h_j D_j \dfrac{\partial Y_j}{\partial x} + u\tau_{xx} + v\tau_{xy} \end{bmatrix}$$

$$\mathbf{g}_v = \begin{bmatrix} \rho D_i \dfrac{\partial Y_i}{\partial y} \\ \tau_{xy} \\ \tau_{yy} \\ k\dfrac{\partial T}{\partial y} + \rho \sum h_j D_j \dfrac{\partial Y_j}{\partial y} + u\tau_{xy} + v\tau_{yy} \end{bmatrix}$$

$$\tau_{xx} = -\frac{2}{3}\mu(\nabla\cdot\mathbf{v}) + 2\mu\frac{\partial u}{\partial x}$$

$$\tau_{yy} = -\frac{2}{3}\mu(\nabla\cdot\mathbf{v}) + 2\mu\frac{\partial v}{\partial y}$$

$$\tau_{\theta\theta} = -\frac{2}{3}\mu(\nabla\cdot\mathbf{v}) + 2\mu\frac{v}{y}$$

$$\tau_{xy} = \mu\left(\frac{\partial u}{\partial y} + \frac{\partial v}{\partial x}\right)$$

$$\nabla\cdot\mathbf{v} = \left(\frac{\partial u}{\partial x} + \frac{\partial v}{\partial y} + \alpha\frac{v}{y}\right)$$

Equation of state

Ideal gas law and Dalton's law for gas-mixtures

$$p(\rho_1,\dots,\rho_K,T)=\sum_{i=1}^K p_i=\sum_{i=1}^K \rho_i \frac{\mathcal{R}}{W_i}T=\rho\frac{\mathcal{R}}{W}T \quad \text{with} \quad \sum_{i=1}^K \rho_i=\rho\,,\, Y_i=\frac{\rho_i}{\rho}$$

Caloric equation

$$h(Y_1,\dots,Y_K,T)=\sum_{i=1}^K Y_i h_i(T) \quad \text{with} \quad h_i(T)=h_i^0+\int_0^T c_{pi}(s)ds$$

Computation of $T=T(\rho_1,\dots,\rho_K,e)$ from implicit equation

$$\sum_{i=1}^K \rho_i\, h_i(T)-\mathcal{R}T\sum_{i=1}^K \frac{\rho_i}{W_i}-\rho e=0$$

for *thermally perfect* gases with $\gamma_i(T)=c_{pi}(T)/c_{vi}(T)$ using an iterative Newton or bisection method

Chemistry and transport properties

Arrhenius-kinetics:

$$\dot\omega_i = \sum_{j=1}^{M} (\nu_{ji}^r - \nu_{ji}^f) \left[k_j^f \prod_{n=1}^{K} \left(\frac{\rho_n}{W_n} \right)^{\nu_{jn}^f} - k_j^r \prod_{n=1}^{K} \left(\frac{\rho_n}{W_n} \right)^{\nu_{jn}^r} \right] \quad i = 1, \dots, K$$

- Parsing of mechanisms and evaluation of $\dot\omega_i$ with Chemkin-II
- $c_{pi}(T)$ and $h_i(T)$ tabulated, linear interpolation between values

Mixture viscosity $\mu = \mu(T, Y_i)$ with Wilke formula

$$\mu = \sum_{i=1}^{K} \frac{Y_i \mu_i}{W_i \sum_{m=1}^{K} Y_m \Phi_{im} / W_m} \text{ with } \Phi_{im} = \frac{1}{\sqrt{8}} \left(1 + \frac{W_i}{W_m} \right)^{-\frac{1}{2}} \left(1 + \left(\frac{\mu_i}{\mu_m} \right)^{\frac{1}{2}} \left(\frac{W_m}{W_j} \right)^{\frac{1}{4}} \right)^2$$

Mixture thermal conductivity $k = k(T, Y_i)$ following Mathur

$$k = \frac{1}{2} \left(W \sum_{i=1}^{K} \frac{Y_i k_i}{W_i} + \frac{1}{W \sum_{i=1}^{K} Y_i / (W_i k_i)} \right)$$

Mixture diffusion coefficients $D_i = D_i(T, p, Y_i)$ from binary diffusion $D_{mi}(T, p)$ as

$$D_i = \frac{1 - Y_i}{W \sum_{m \neq i} Y_m / (W_m D_{mi})}$$

- Evaluation with Chemkin-II Transport library

Splitting methods

$$\partial_t \mathbf{q} + \partial_x(\mathbf{f} - \mathbf{f}_v) + \partial_y(\mathbf{g} - \mathbf{g}_v) = \frac{\alpha}{y}(\mathbf{c} - \mathbf{g} + \mathbf{g}_v) + \mathbf{s}$$

Dimensional splitting for PDE

$$\mathcal{X}^{(\Delta t)}: \quad \partial_t \mathbf{q} + \partial_x(\mathbf{f}(\mathbf{q}) - \mathbf{f}_v(\mathbf{q})) = 0\,, \qquad \text{IC: } \mathbf{Q}(t_m) \stackrel{\Delta t}{\Longrightarrow} \tilde{\mathbf{Q}}^{1/2}$$

$$\mathcal{Y}^{(\Delta t)}: \quad \partial_t \mathbf{q} + \partial_y(\mathbf{g}(\mathbf{q}) - \mathbf{g}_v(\mathbf{q})) = 0\,, \qquad \text{IC: } \tilde{\mathbf{Q}}^{1/2} \stackrel{\Delta t}{\Longrightarrow} \tilde{\mathbf{Q}}$$

Treat right-hand side as source term

$$\mathcal{C}^{(\Delta t)}: \quad \partial_t \mathbf{q} = \tfrac{\alpha}{y}(\mathbf{c}(\mathbf{q}) - \mathbf{g}(\mathbf{q}) + \mathbf{g}_v(\mathbf{q}))\,, \qquad \text{IC: } \tilde{\mathbf{Q}} \stackrel{\Delta t}{\Longrightarrow} \bar{\mathbf{Q}}$$

Chemical source term

$$\mathcal{S}^{(\Delta t)}: \quad \partial_t \mathbf{q} = \mathbf{s}(\mathbf{q})\,, \qquad \text{IC: } \bar{\mathbf{Q}} \stackrel{\Delta t}{\Longrightarrow} \mathbf{Q}(t_m + \Delta t)$$

Formally 1st-order algorithm

$$\mathbf{Q}(t_m + \Delta t) = \mathcal{S}^{(\Delta t)}\mathcal{C}^{(\Delta t)}\mathcal{Y}^{(\Delta t)}\mathcal{X}^{(\Delta t)}(\mathbf{Q}(t_m))$$

but all sub-operators 2nd-order accurate or higher.

Finite volume discretization

Time discretization $t_n = n\Delta t$, discrete volumes $I_{jk} =$
$[x_j - \frac{1}{2}\Delta x, x_j + \frac{1}{2}\Delta x[\times[y_k - \frac{1}{2}\Delta y, y_k + \frac{1}{2}\Delta y[\times =: [x_{j-1/2}, x_{j+1/2}[\times[y_{k-1/2}, y_{k+1/2}[$

Approximation $\mathbf{Q}_{jk}(t) \approx \frac{1}{|I_{jk}|} \int\limits_{I_{jk}} \mathbf{q}(\mathbf{x}, t)\, dx$ and numerical fluxes

$$\mathbf{F}\left(\mathbf{Q}_{jk}(t), \mathbf{Q}_{j+1,k}(t)\right) \approx \mathbf{f}(\mathbf{q}(x_{j+1/2}, y_k, t)),$$

$$\mathbf{F}_v\left(\mathbf{Q}_{jk}(t), \mathbf{Q}_{j+1,k}(t)\right) \approx \mathbf{f}_v(\mathbf{q}(x_{j+1/2}, y_k, t), \nabla\mathbf{q}(x_{j+1/2}, y_k, t))$$

yield (for simplicity)

$$\mathbf{Q}_{jk}^{n+1} = \mathbf{Q}_{kj}^{n} - \frac{\Delta t}{\Delta x}\left[\mathbf{F}\left(\mathbf{Q}_{jk}^{n}, \mathbf{Q}_{j+1,k}^{n}\right) - \mathbf{F}\left(\mathbf{Q}_{j-1,k}^{n}, \mathbf{Q}_{jk}^{n}\right)\right] + \frac{\Delta t}{\Delta x}\left[\mathbf{F}_v\left(\mathbf{Q}_{jk}^{n}, \mathbf{Q}_{j+1,k}^{n}\right) - \mathbf{F}_v\left(\mathbf{Q}_{j-1,k}^{n}, \mathbf{Q}_{jk}^{n}\right)\right]$$

- Riemann solver to approximate $\mathbf{F}\left(\mathbf{Q}_{jk}^{n}, \mathbf{Q}_{j+1,k}^{n}\right)$
- 1st-order finite differences for $\mathbf{F}_v\left(\mathbf{Q}_{jk}^{n}, \mathbf{Q}_{j+1,k}^{n}\right)$ yield 2nd-order accurate central differences in $(*)$

Stability condition used:

$$\max_{i,j,k}\left\{\frac{\Delta t}{\Delta x}(|u_{jk}| + c_{jk}) + \frac{8}{3}\frac{\mu_{jk}\Delta t}{\rho_{jk}\Delta x^2}, \frac{\Delta t}{\Delta x}(|u_{jk}| + c_{jk}) + \frac{2k_j\Delta t}{c_{v,jk}\rho_j\Delta x^2}, \frac{\Delta t}{\Delta x}(|u_{jk}| + c_{jk}) + D_{i,jk}\frac{\Delta t}{\Delta x^2}\right\} \leq 1$$

Finite volume discretization – cont.

Symmetry source term $\mathcal{C}^{(\Delta t)}$: Use

$$\mathbf{Q}_{jk}^{n+1} = \mathbf{Q}_{jk}^{n} + \Delta t \left(\frac{\alpha}{y} (\mathbf{c}(\mathbf{Q}_{jk}^{n}) - \mathbf{g}(\mathbf{Q}_{jk}^{n}) + \frac{1}{2} \left(\mathbf{G}_v \left(\mathbf{Q}_{jk}^{n}, \mathbf{Q}_{j,k+1}^{n} \right) + \mathbf{G}_v \left(\mathbf{Q}_{j,k-1}^{n}, \mathbf{Q}_{jk}^{n} \right) \right) \right)$$

within explicit 2nd-order accurate Runge-Kutta method

- Gives 2nd-order central difference approximation of $\mathbf{G}_v$
- Transport properties μ, k, D_i are stored in vector of state $\mathbf{Q}$ and kept constant throughout entire time step

Chemical source term $\mathcal{S}^{(\cdot)}$:

- 4th-order accurate semi-implicit ODE-solver subcycles within each cell
- ρ, e, u, v remain unchanged!

$$\partial_t \rho_i = W_i \dot{\omega}_i(\rho_1, \dots, \rho_K, T) \qquad i = 1, \dots, K$$

Riemann solver for combustion

(S1) Calculate standard Roe-averages $\hat{\rho} = \frac{\sqrt{\rho_L}\rho_R + \sqrt{\rho_R}\rho_L}{\sqrt{\rho_L}+\sqrt{\rho_R}} = \sqrt{\rho_L \rho_R}$ and $\hat{w} = \frac{\sqrt{\rho_L}w_L + \sqrt{\rho_R}w_R}{\sqrt{\rho_L}+\sqrt{\rho_R}}$ for $\hat{u}$, $\hat{v}$, $\hat{H}$, $\hat{Y}_i$, $\hat{T}$.

(S2) Compute $\hat{\gamma} := \hat{c}_p/\hat{c}_v$ with $\hat{c}_{\{p/v\}i} = \dfrac{1}{T_R - T_L}\displaystyle\int_{T_L}^{T_R} c_{\{p,v\}i}(\tau)\, d\tau$.

(S3) Calculate $\hat{\phi}_i := (\hat{\gamma}-1)\left(\frac{\hat{\mathbf{u}}^2}{2} - \hat{h}_i\right) + \hat{\gamma} R_i \hat{T}$ with standard Roe-averages $\hat{e}_i$ or $\hat{h}_i$.

(S4) Calculate $\hat{c} := \left(\sum_{i=1}^K \hat{Y}_i \hat{\phi}_i - (\hat{\gamma}-1)\hat{\mathbf{u}}^2 + (\hat{\gamma}-1)\hat{H}\right)^{1/2}$.

(S5) Use $\Delta\mathbf{q} = \mathbf{q}_R - \mathbf{q}_L$ and Δp to compute the wave strengths a_m.

(S6) Calculate $\mathcal{W}_1 = a_1 \hat{\mathbf{r}}_1$, $\mathcal{W}_2 = \displaystyle\sum_{\iota=2}^{K+d} a_\iota \hat{\mathbf{r}}_\iota$, $\mathcal{W}_3 = a_{K+d+1}\hat{\mathbf{r}}_{K+d+1}$.

(S7) Evaluate $s_1 = \hat{u} - \hat{c}$, $s_2 = \hat{u}$, $s_3 = \hat{u} + \hat{c}$.

(S8) Evaluate $\rho^\star_{L/R}$, $u^\star_{L/R}$, $e^\star_{L/R}$, $c^\star_{L/R}$ from $\mathbf{q}^\star_L = \mathbf{q}_L + \mathcal{W}_1$ and $\mathbf{q}^\star_R = \mathbf{q}_R - \mathcal{W}_3$.

(S9) If $\rho^\star_{L/R} \le 0$ or $e^\star_{L/R} \le 0$ use $\mathbf{F}_{HLL}(\mathbf{q}_L, \mathbf{q}_R)$ and go to (S12).

(S10) Entropy correction: Evaluate $|\tilde{s}_\iota|$.
$\mathbf{F}_{Roe}(\mathbf{q}_L, \mathbf{q}_R) = \frac{1}{2}\left(\mathbf{f}(\mathbf{q}_L) + \mathbf{f}(\mathbf{q}_R) - \sum_{\iota=1}^3 |\tilde{s}_\iota| \mathcal{W}_\iota\right)$

(S11) Positivity correction: Replace $\mathbf{F}_i$ by

$$\mathbf{F}_i^\star = \mathbf{F}_\rho \cdot \begin{cases} Y_i^l\,, & \mathbf{F}_\rho \ge 0\,, \\ Y_i^r\,, & \mathbf{F}_\rho < 0\,. \end{cases}$$

(S12) Evaluate maximal signal speed by $S = \max(|s_1|, |s_3|)$.

Shock-induced combustion around a sphere

- Spherical projectile of radius $1.5\,\mathrm{mm}$ travels with constant velocity $v_I = 2170.6\,\mathrm{m/s}$ through $\mathrm{H_2} : \mathrm{O_2} : \mathrm{Ar}$ mixture (molar ratios 2:1:7) at $6.67\,\mathrm{kPa}$ and $T = 298\,\mathrm{K}$
- Mechanism by [Westbrook, 1982]: 34 forward reactions, 9 species
- Axisymmetric Euler simulation on AMR base mesh of 70×40 cells
- Comparison of 3-level computation with refinement factors 2,2 ($\sim 5\,\mathrm{Pts}/l_{ig}$) and a 4-level computation with refinement factors 2,2,4 ($\sim 19\,\mathrm{Pts}/l_{ig}$) at $t = 350\,\mu\mathrm{s}$
- Higher resolved computation captures combustion zone visibly better and at slightly different position (see below)

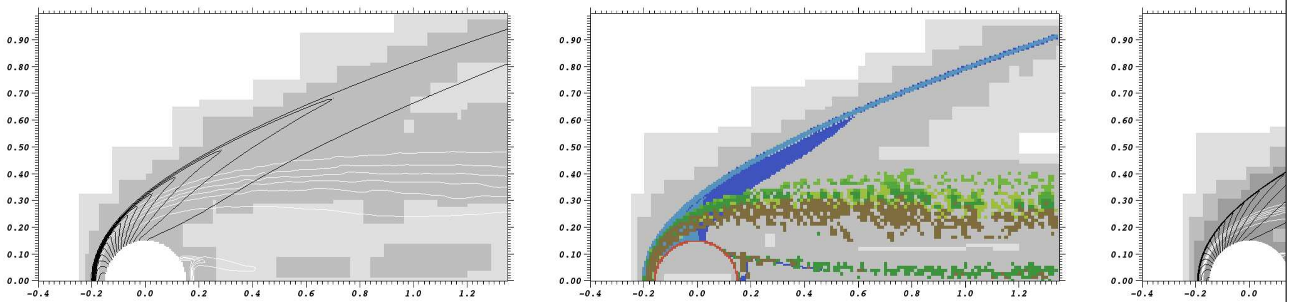

Iso-contours of p (black) and Y_{H_2} (white) on refinement domains for 3-level (left) and 4-level computation (right)

Lehr's ballistic range experiments

- Spherical-nosed projectile of radius 1.5 mm travels with constant velocity through stoichiometric $\mathrm{H_2} : \mathrm{O_2} : \mathrm{N_2}$ mixture (molar ratios 2:1:3.76) at 42.663 kPa and $T = 293\,\mathrm{K}$ [Lehr, 1972]
- Mechanism by [Jachimowski, 1988]: 19 equilibrium reactions, 9 species. Chapman Jouguet velocity $\sim 1957\,\mathrm{m/s}$.
- Axisymmetric Navier-Stokes and Eulers simulations on AMR base mesh of 400×200 cells, physical domain size $6\,\mathrm{cm} \times 3\,\mathrm{cm}$
- 4-level computations with refinement factors 2,2,4 to final time $t = 170\,\mu\mathrm{s}$. Refinement downstream removed.
- Main configurations
  - Velocity $v_I = 1931\,\mathrm{m/s}$ ($M = 4.79$), $\sim 40\,\mathrm{Pts}/l_{ig}$
  - Velocity $v_I = 1806\,\mathrm{m/s}$ ($M = 4.48$), $\sim 60\,\mathrm{Pts}/l_{ig}$
- Various previous studies with not entirely consistent results. E.g. [Yungster and Radhakrishnan, 1996], [Axdahl et al., 2011]
- Stagnation point location and pressure tracked in every time step
- All computations were on 32 cores requiring $\sim 1500\,\mathrm{h}$ CPU each

Viscous case – $M = 4.79$

- 5619 iterations with CFL=0.9 to $t = 170\,\mu\mathrm{s}$
- Oscillation frequency in last $20\,\mu\mathrm{s}$: $\sim 722\,\mathrm{kHz}$ (viscous), $\sim 737\,\mathrm{kHz}$ (inviscid)
- Experimental value: $\sim 720\,\mathrm{kHz}$

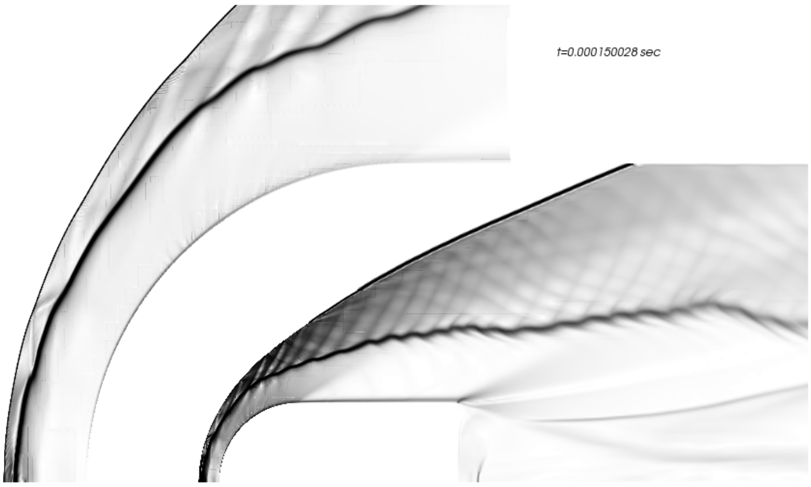

Schlieren plot of density

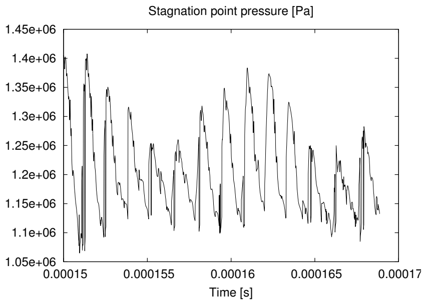

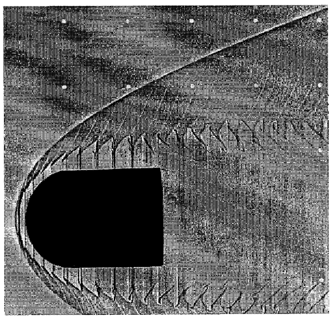

Viscous case – $M = 4.79$ – mesh adaptation

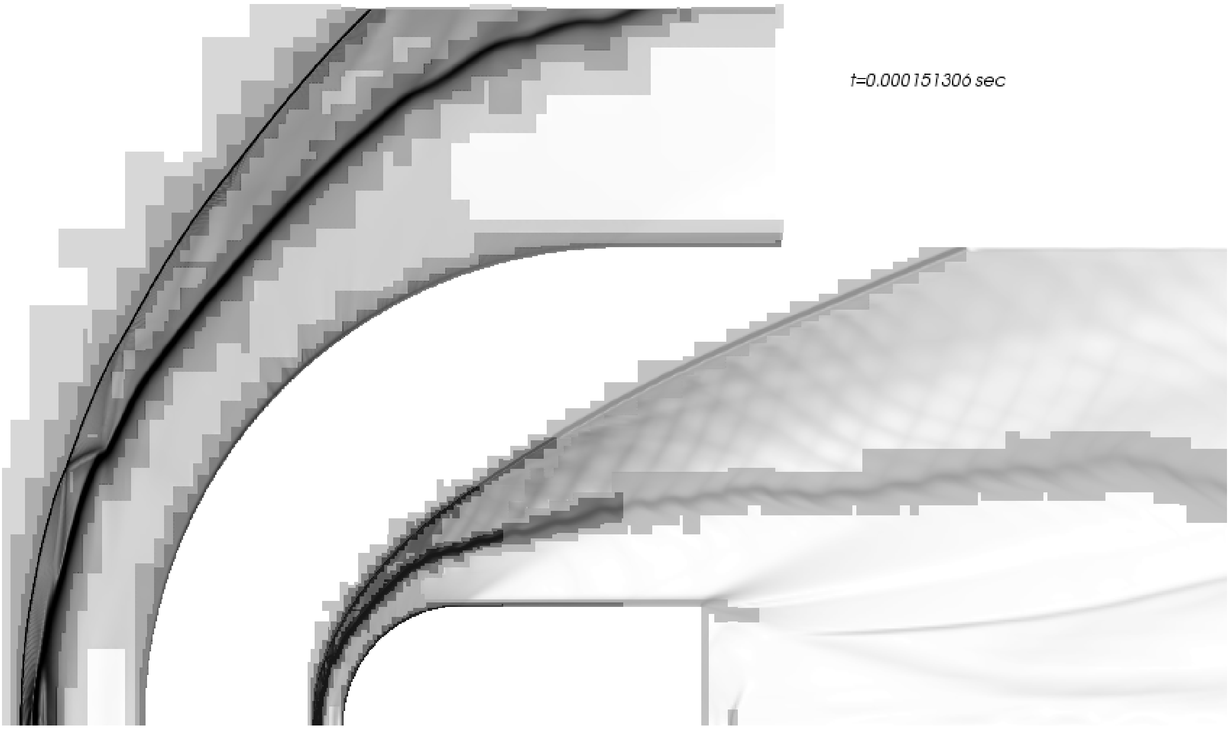

Comparison of temperature field

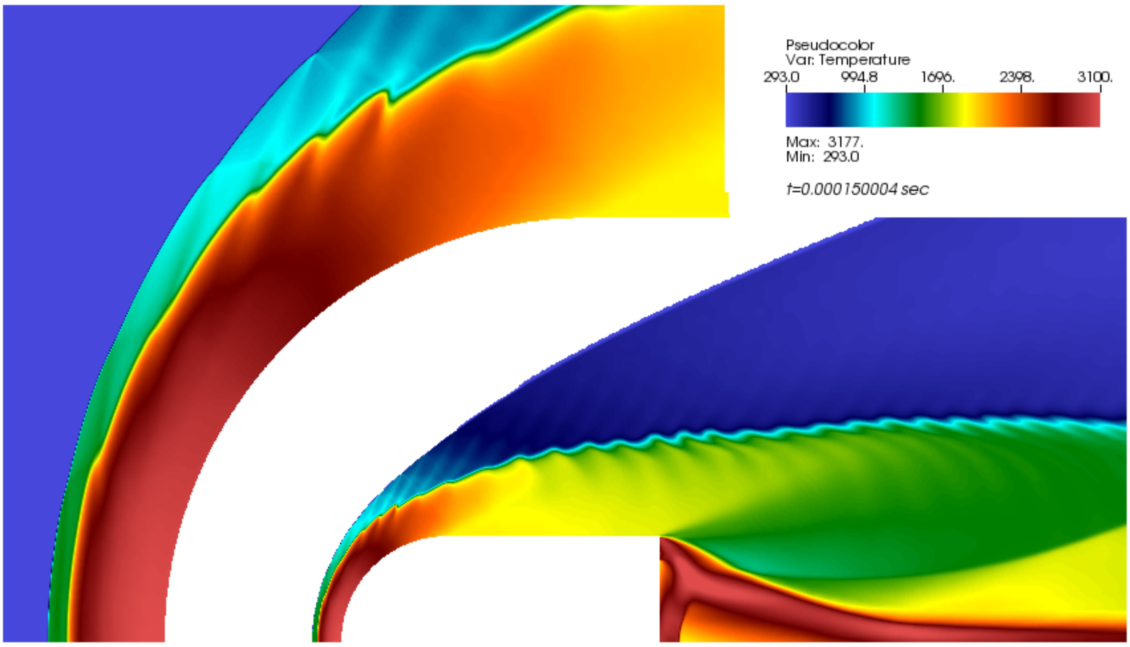

Inviscid

Viscous case – $M = 4.48$

- 5432 iterations with CFL=0.9 to $t = 170\,\mu\mathrm{s}$
- Oscillation frequency in last $20\,\mu\mathrm{s}$: $\sim 417\,\mathrm{kHz}$
- Experimental value: $\sim 425\,\mathrm{kHz}$

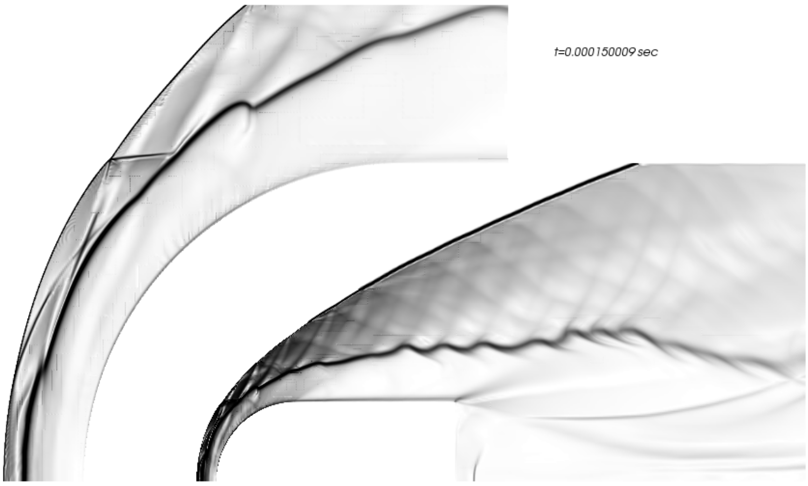

Schlieren plot of density

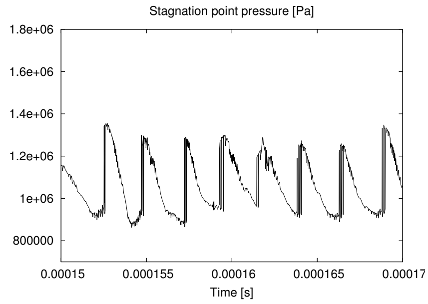

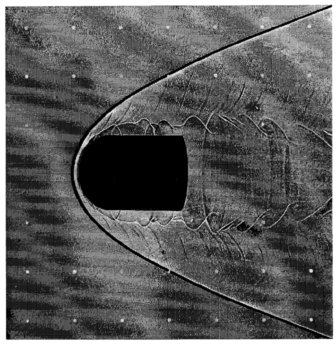

Oscillation mechanism

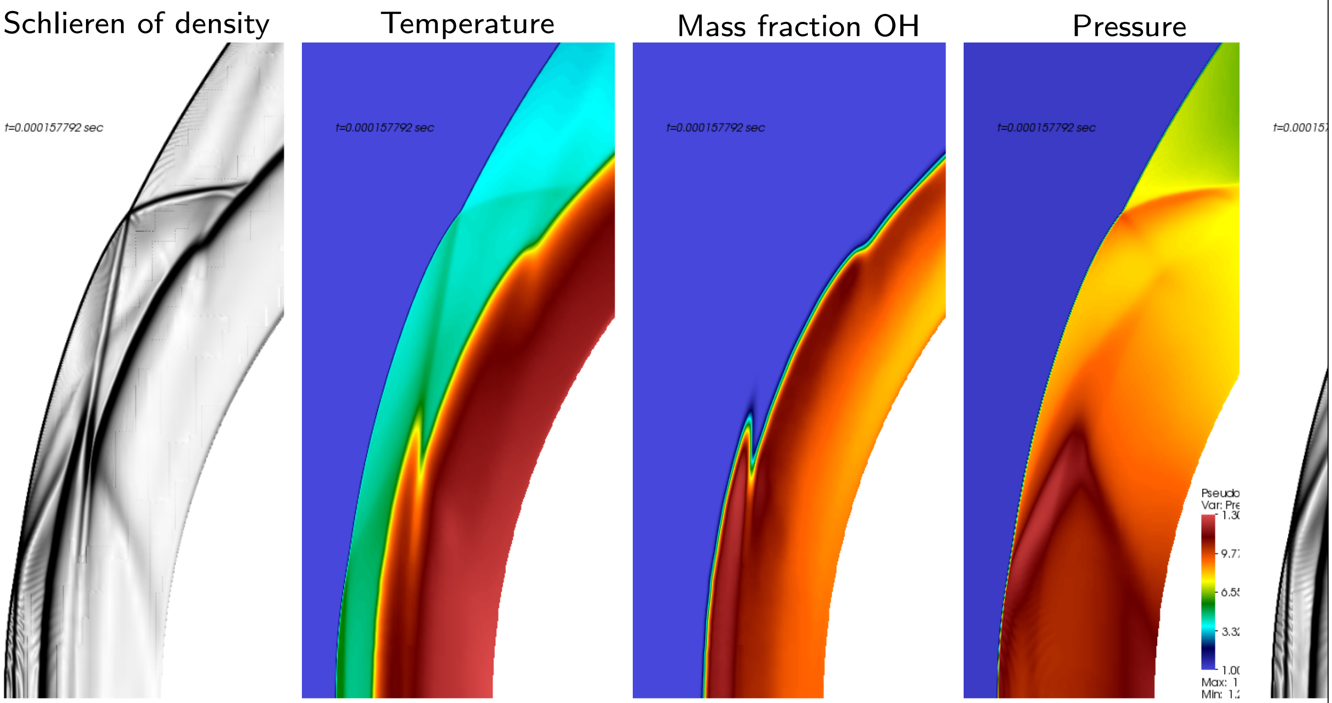

- Oscillation created by accelerated reaction due to slip line from previous triple point

Inviscid case – $M = 4.48$

- 4048 iterations with CFL=0.9 to $t = 170\,\mu\mathrm{s}$
- Oscillation frequency in last 20 $\mu\mathrm{s}$: $\sim 395\,\mathrm{kHz}$
- Experimental value: $\sim 425\,\mathrm{kHz}$

Schlieren plot of density

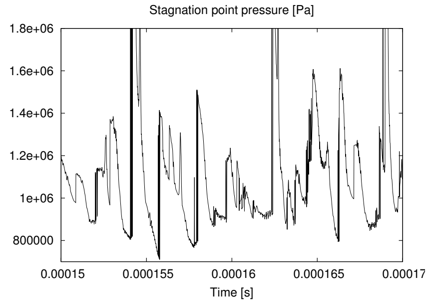

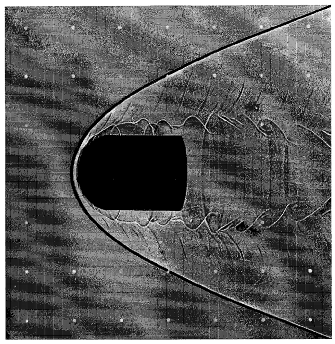

Deflagration to detonation transition in 2d

Hot sphere of 2500 K in stoichiometric $\mathrm{H_2/O_2}$ in closed-end chamber of $2\,\mathrm{cm}$ diameter

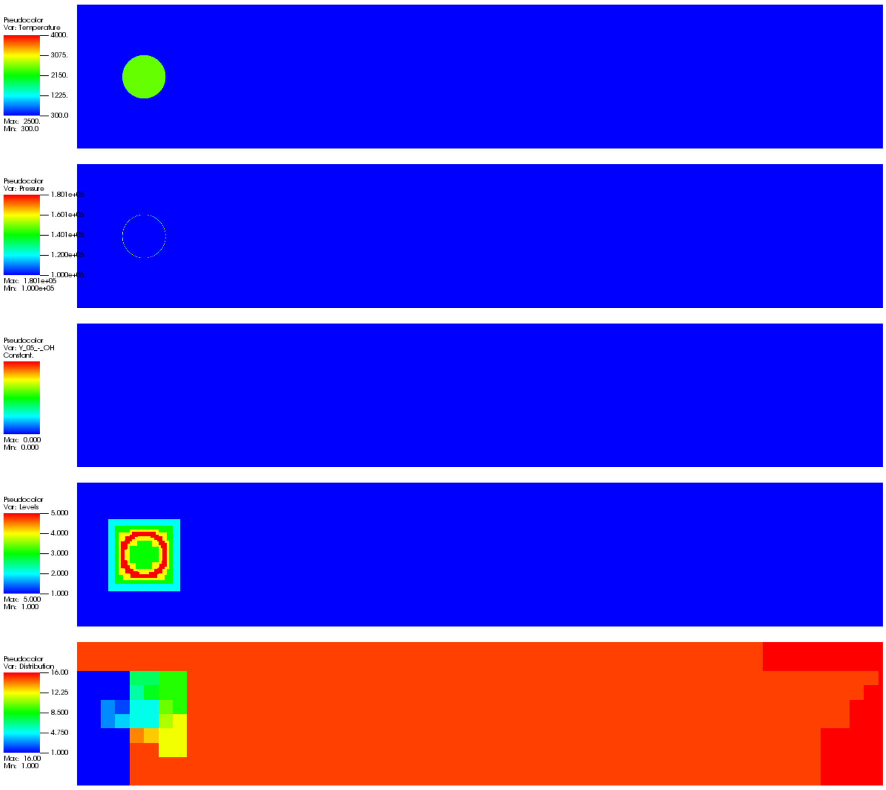

Simulation of regular structures

- CJ detonation for $\mathrm{H_2 : O_2 : Ar}$ (2:1:7) at $T_0 = 298\,\mathrm{K}$ and $p_0 = 10\,\mathrm{kPa}$, cell width $1.6\,\mathrm{cm}$
- Perturb 1d solution with unreacted high-pressure pocket behind front
- Triple point trajectories by tracking max $|\omega|$ on auxiliary mesh shifted through grid with CJ velocity. $\omega = \dfrac{\partial v}{\partial x} - \dfrac{\partial u}{\partial y}$
- SAMR simulation with 4 additional levels (2,2,2,4), $67.6\,\mathrm{Pts}/l_{ig}$
- Configuration similar to Oran et al., J. Combustion and Flame 113, 1998.

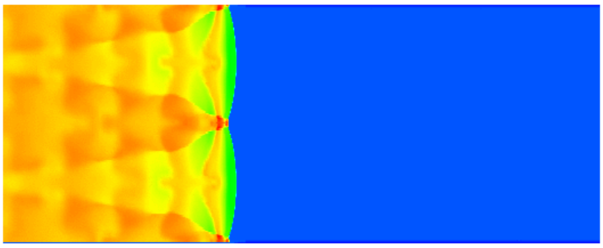

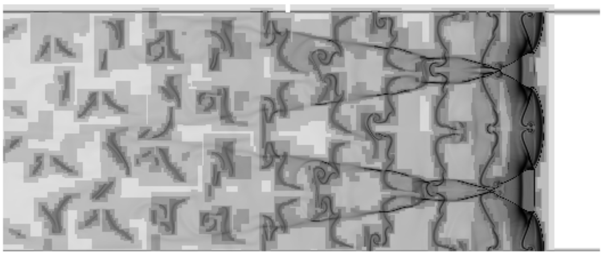

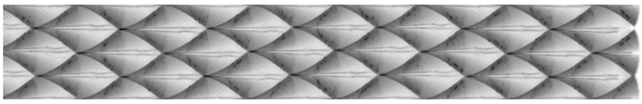

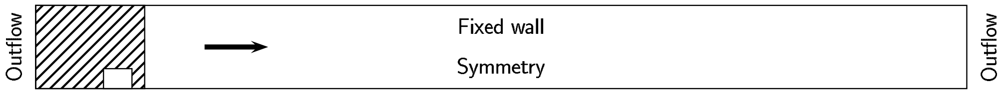

Triple point analysis

Double Mach reflection structure shortly before the next collision

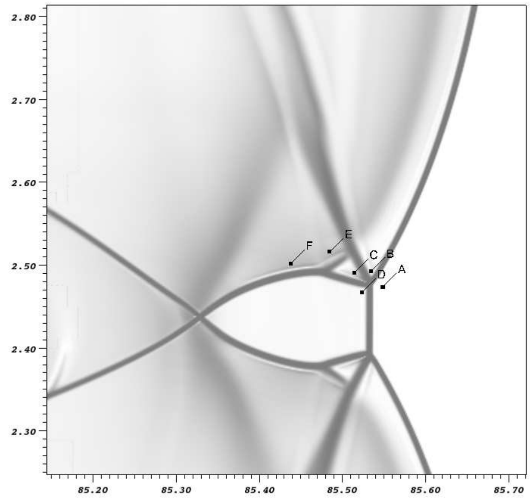

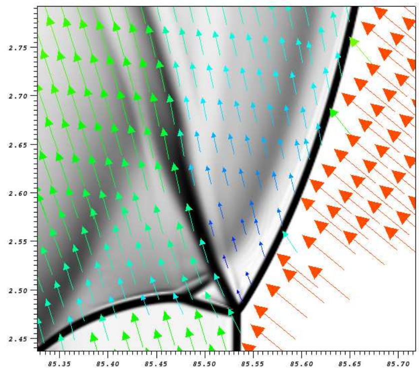

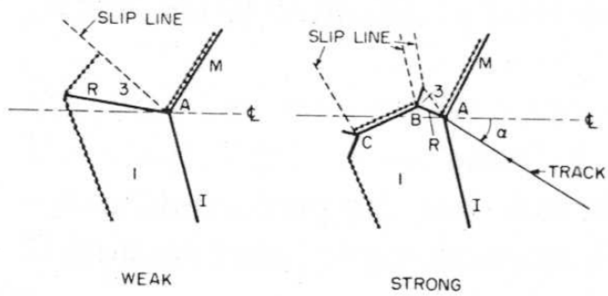

	p/p_0	ρ/ρ_0	T [K]	u[m/s]	M
A	1.00	1.00	298	1775	5.078
B	31.45	4.17	2248	447	0.477
C	31.69	5.32	1775	965	1.153
D	19.17	3.84	1487	1178	1.533
E	35.61	5.72	1856	901	1.053
F	40.61	6.09	1987	777	0.880

Detonation propagation through pipe bends

- 2D Simulation of CJ detonation for $\mathrm{H_2 : O_2 : Ar}/2:1:7$ at $T_0 = 298\,\mathrm{K}$ and $p_0 = 10\,\mathrm{kPa}$. Tube width of 5 detonation cells
- AMR base grid 1200×992. 4 additional refinement levels (2,2,2,4). $67.6\,\mathrm{Pts}/l_{ig}$
- Adaptive computations use up to $7.1 \cdot 10^6$ cells ($4.8 \cdot 10^6$ on highest level) instead of $1.22 \cdot 10^9$ cells (uniform grid)
- $\sim 70,000\,\mathrm{h}$ CPU on 128 CPUs Pentium-4 2.2GHz

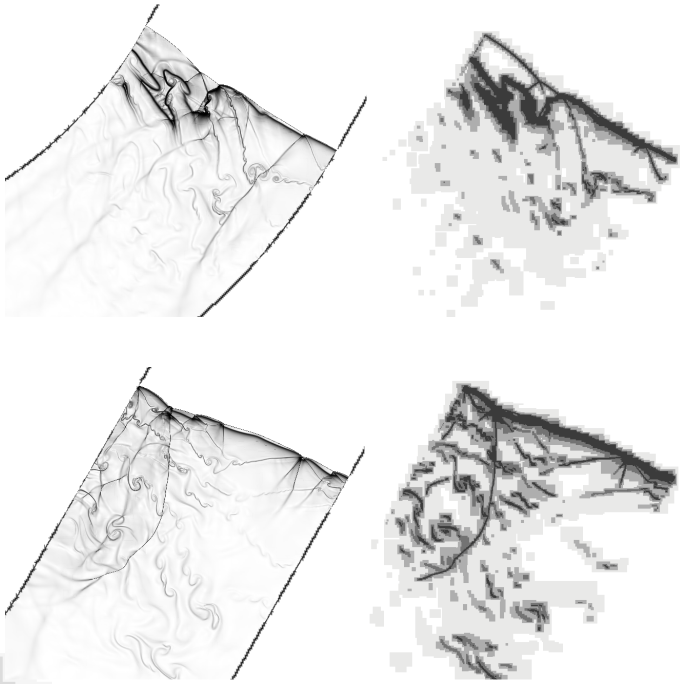

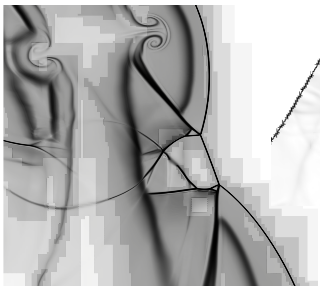

Triple point tracks

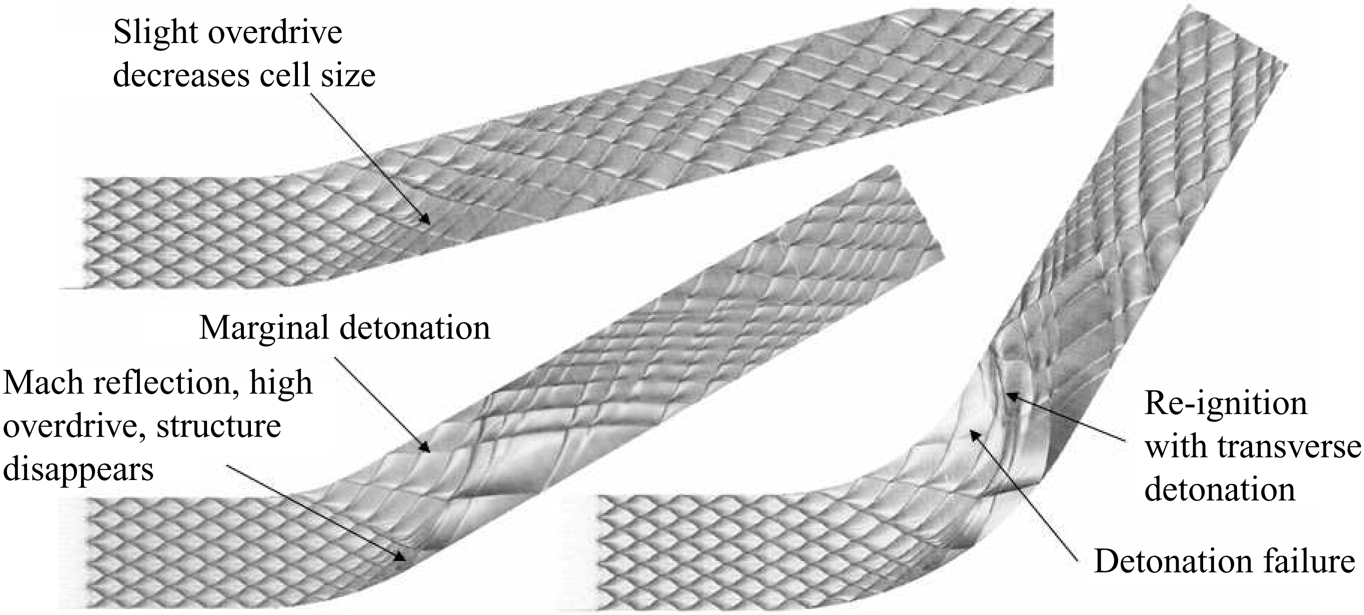

$\varphi = 15^o$ (left, top), $\varphi = 30^o$ (left, bottom), and $\varphi = 60^o$ (right)

The effect of resolution - $\varphi = 15^o$

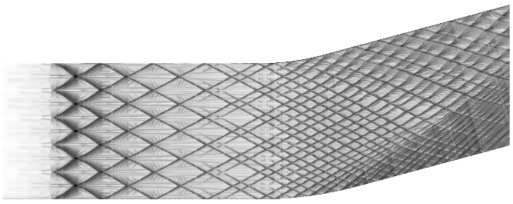

$14.05\,\mathrm{Pts}/l_{ig}$

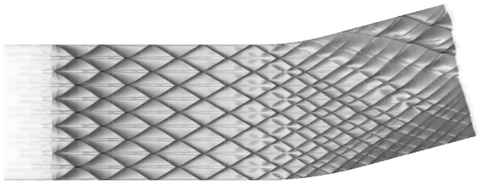

$28.1\,\mathrm{Pts}/l_{ig}$

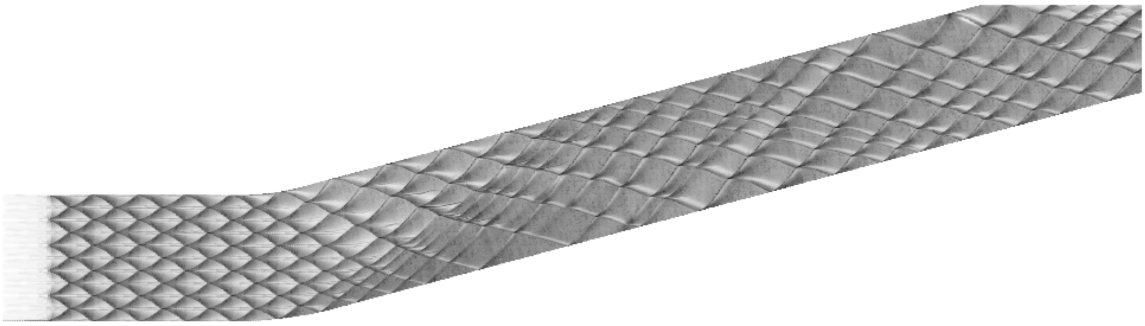

$56.2\,\mathrm{Pts}/l_{ig}$

- On coarse meshes, the high energy release in triple points cannot be captured
- Under sufficient resolution, the oscillation frequency is recovered after the bend

Triple point structures – $\varphi = 15^{\mathrm{o}}$

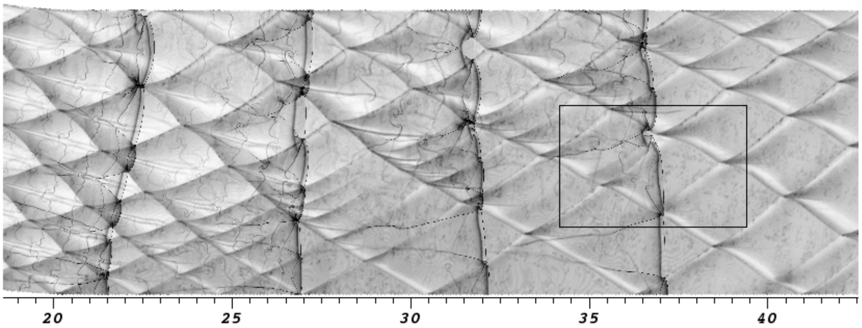

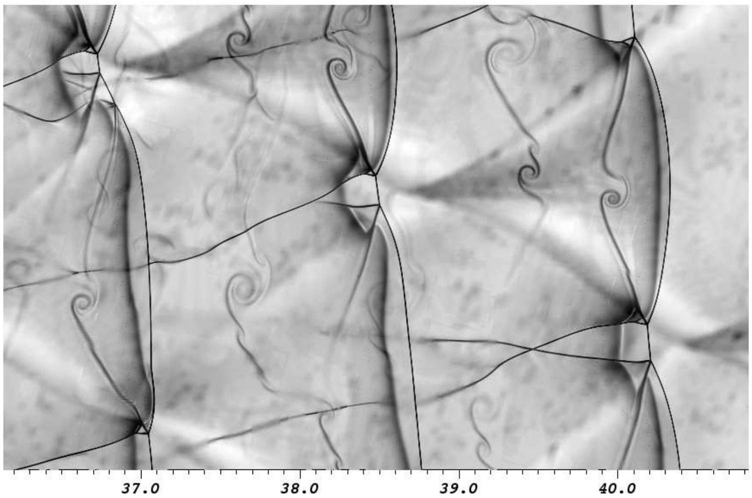

- Triple point re-initiation after bend with change from transitional to Double Mach reflection

Triple point structures – $\varphi = 30^{\mathrm{o}}$

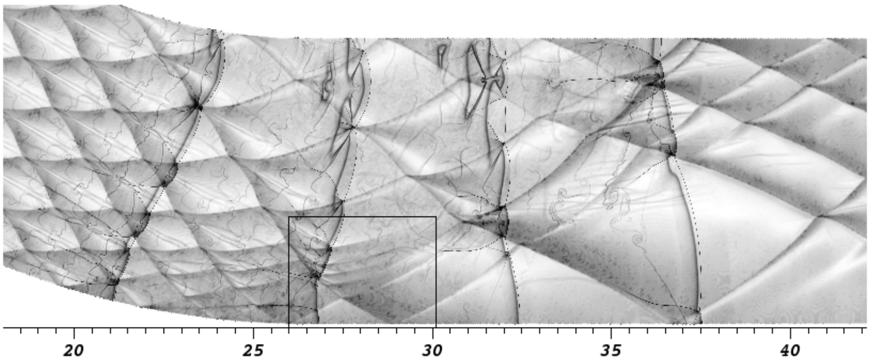

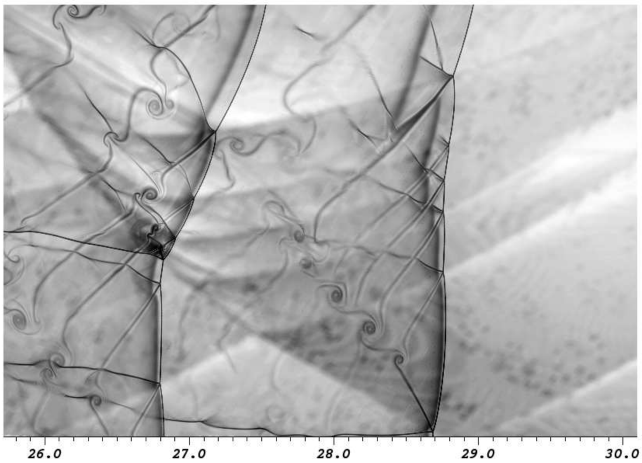

- Triple point quenching and failure as single Mach reflection

Detonation cell structure in 3D

- 44.8 Pts/l_{ig} for $\mathrm{H_2} : \mathrm{O_2} : \mathrm{Ar}$ CJ detonation
- SAMR base grid 400x24x24 for one quadrant, 2 additional refinement levels (2, 4)
- Simulation uses $\sim 18\,\mathrm{M}$ cells instead of $\sim 118\,\mathrm{M}$ (unigrid)
- $\sim 51,000\,\mathrm{h}$ CPU on 128 CPU Compaq Alpha. $\mathcal{H}$: 37.6 %, $\mathcal{S}$: 25.1 %

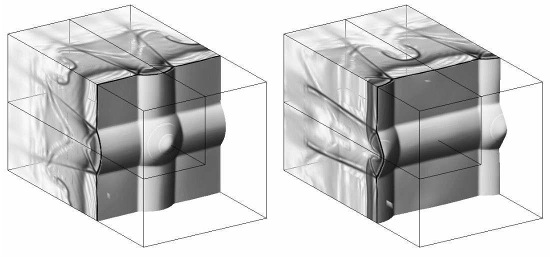

Schlieren plots of density, mirrored for visualization

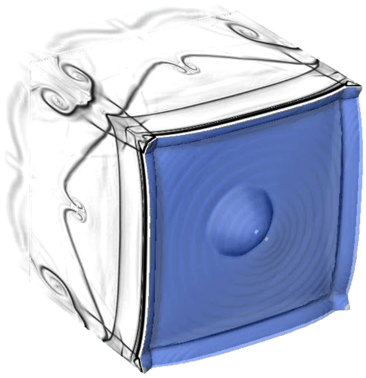

Schlieren plots of Y_{OH}

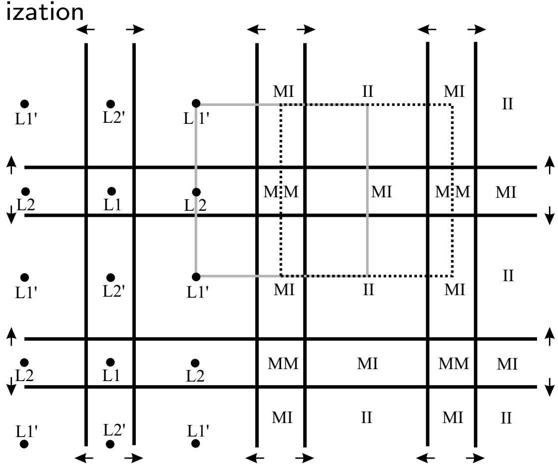

Schematic front view of the periodic triple point line structure right plot at the same time.

Temporal Development of Detonation Velocity

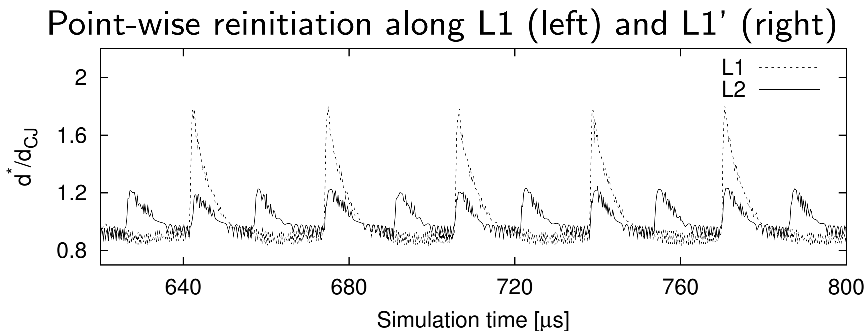

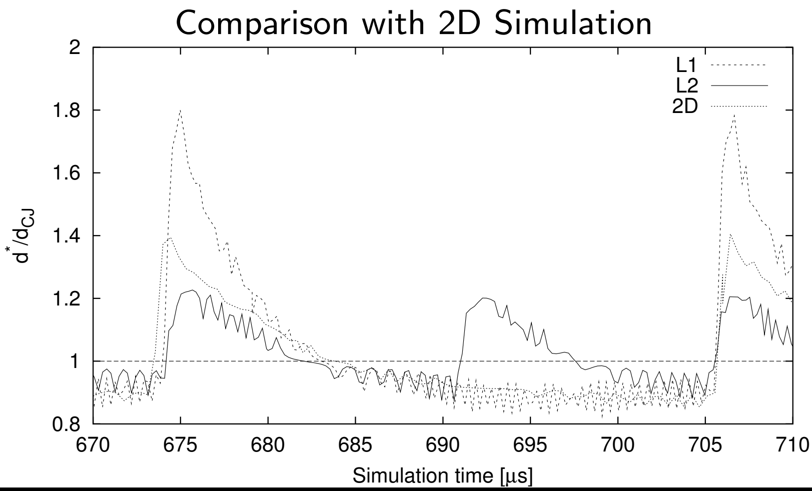

Triple point analysis

Tracks of triple point lines

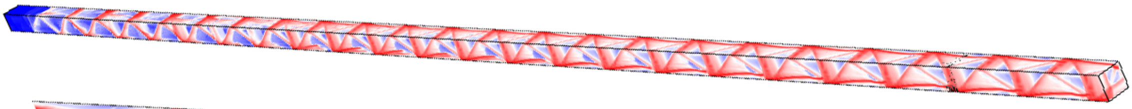

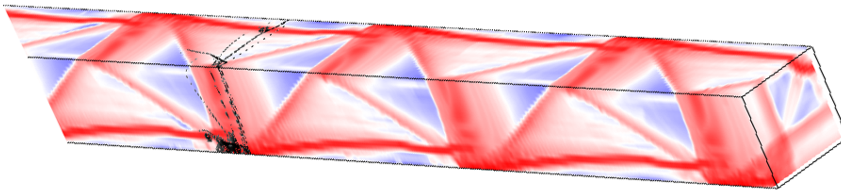

Schlieren plots perpendicular to y- and z-plane (right) and on triple point line tracks (below)

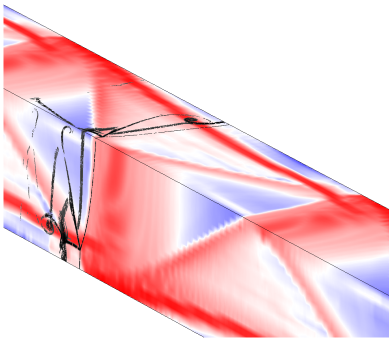

Weakest TMR structure in Incident-Incident region immediately before collision

Schlieren plots perpendicu-

Detonation ignition by a hot jet in 3d

- 3d Euler simulation on AMR base mesh of $64 \times 32 \times 16$ cells
- Domain size $3.2\,\mathrm{cm} \times 1.6\,\mathrm{cm} \times 0.8\,\mathrm{cm}$
- Inflow of $\mathrm{H_2 : O_2 : Ar}$ mixture (molar ratios 2:1:7) at $10\,\mathrm{kPa}$ and $T = 298\,\mathrm{K}$ at CJ velocity $V_{\mathrm{CJ}} = 1627\,\mathrm{m/s}$
- Hot jet inflow with fully reacted CJ conditions, i.e., $T = 3296\,\mathrm{K}$, $p = 172.7\,\mathrm{kPa}$ and $\rho = 0.0893\,\mathrm{kg/m^3}$
- Mechanism by [Westbrook, 1982]: 34 forward reactions, 9 species
- Computations on 1024 cores Intel E5-2692 2.20 GHz (Tianhe-2)
- X. Cai, J. Liang, RD, Y. Che, Z. Lin, *Int. J. Hydrogen Energy* 41(4): 3222–3239, 2016

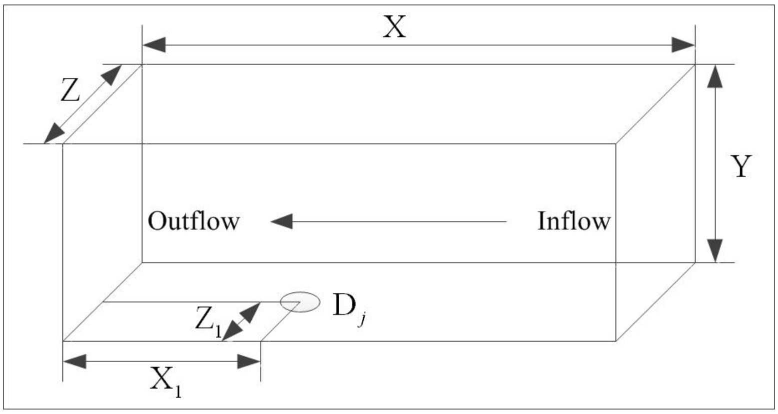

Detonation ignition process - Front view

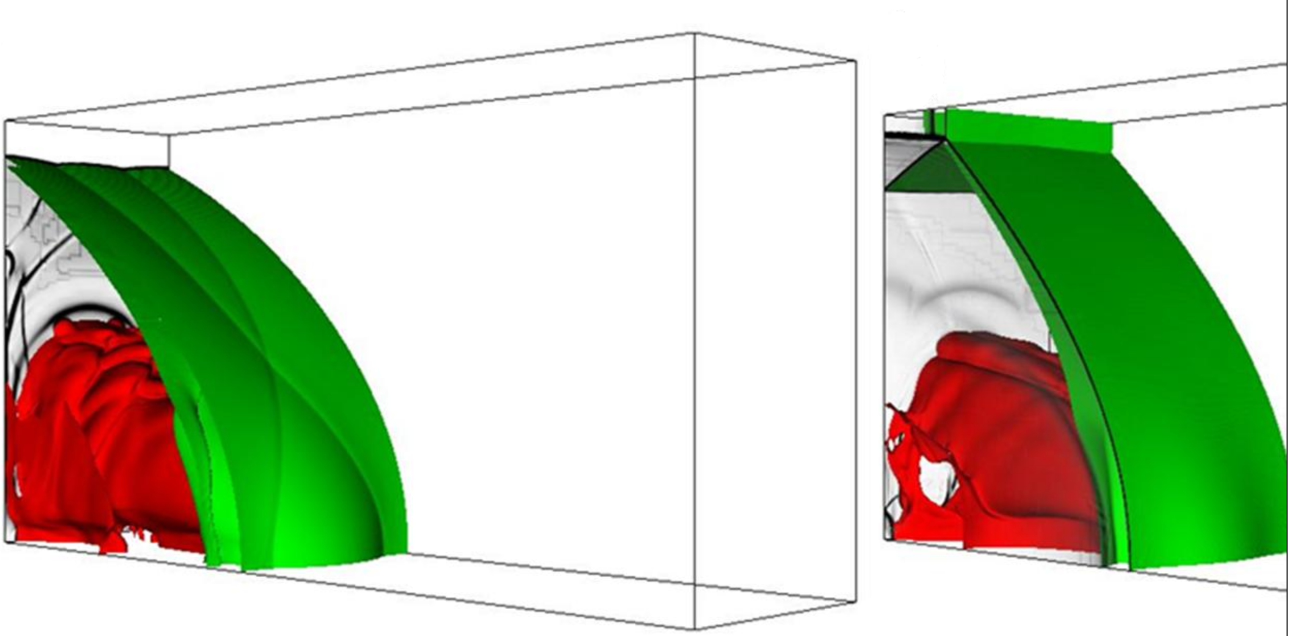

Isosurfaces of ρ at $t = 18.85\,\mu\text{s}$ Isosurfaces of ρ at $t = 224.34\,\mu\text{s}$ Isosurfaces of ρ at $t = 323.07\,\mu\text{s}$ Isosurfaces of ρ at $t = 334.10\,\mu\text{s}$

Detonation propagation

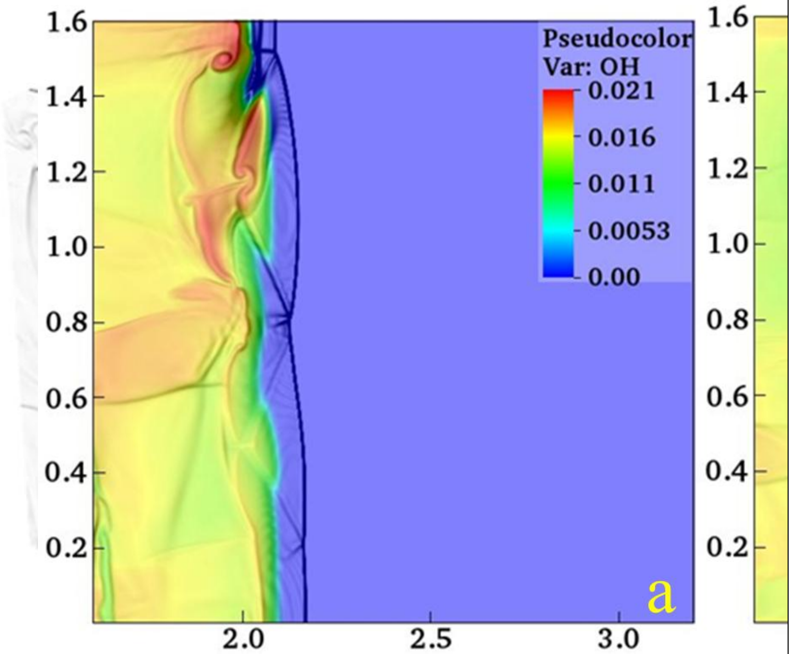

- Continuous jet injection overdrives the detonation to $f \approx 1.07$
- Number of triple point lines is increased compared to CJ case
- Rectangular domain straightens triple point lines
- Primarily TMR triple point line structures visible as in previous case

Dynamic mesh refinement

- Mesh adaptation with 4 additional levels refined by factors 2, 2, 2, 2 $\longrightarrow$ $\sim 30.85\,\mathrm{Pts}/l_{ig}$
- Adaptation indicators similar as before

$t = 234.10\,\mu\mathrm{s}$ $t = 253.32\,\mu\mathrm{s}$ $t = 272.78\,\mu\mathrm{s}$ $t = 292.46\,\mu\mathrm{s}$

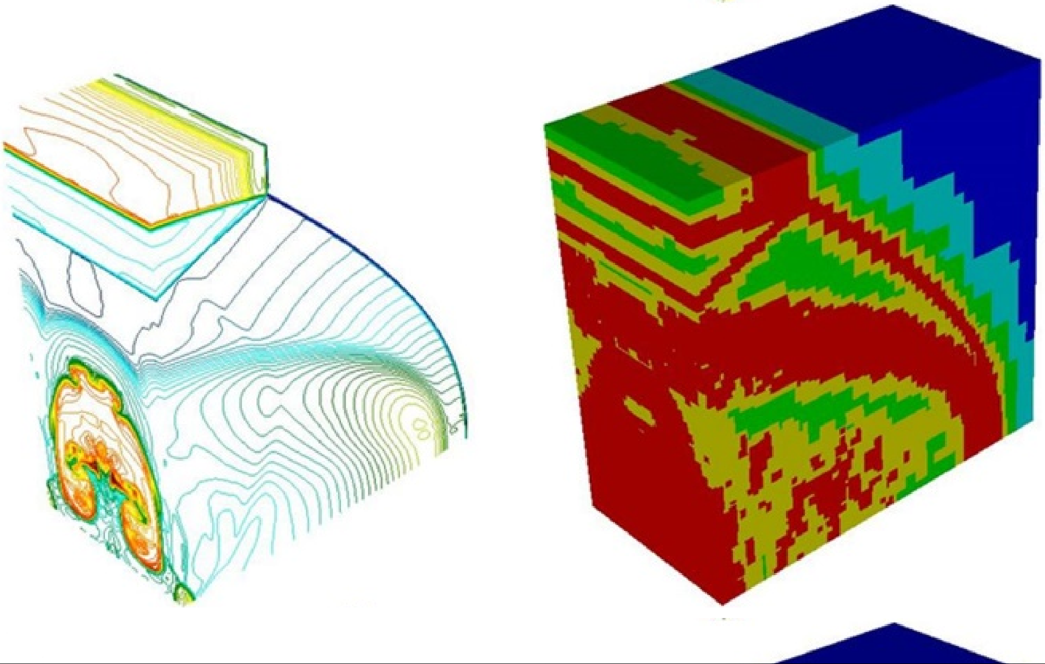

Shock-boundary layer interaction

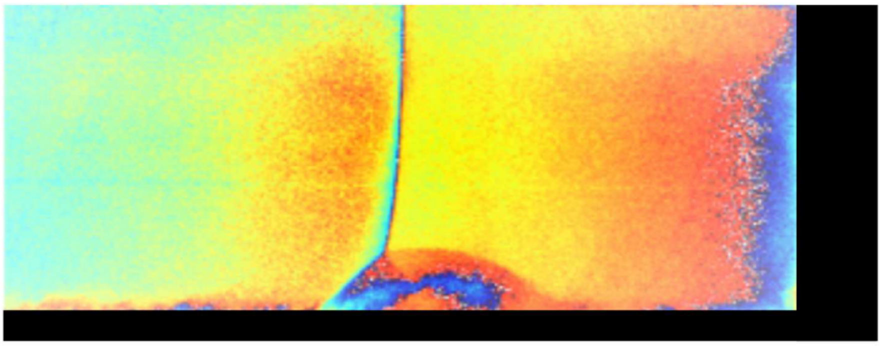

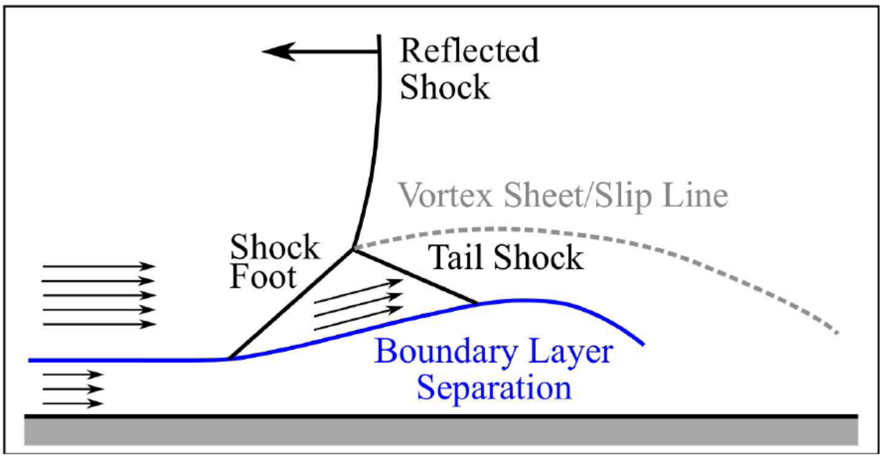

Non-reactive case

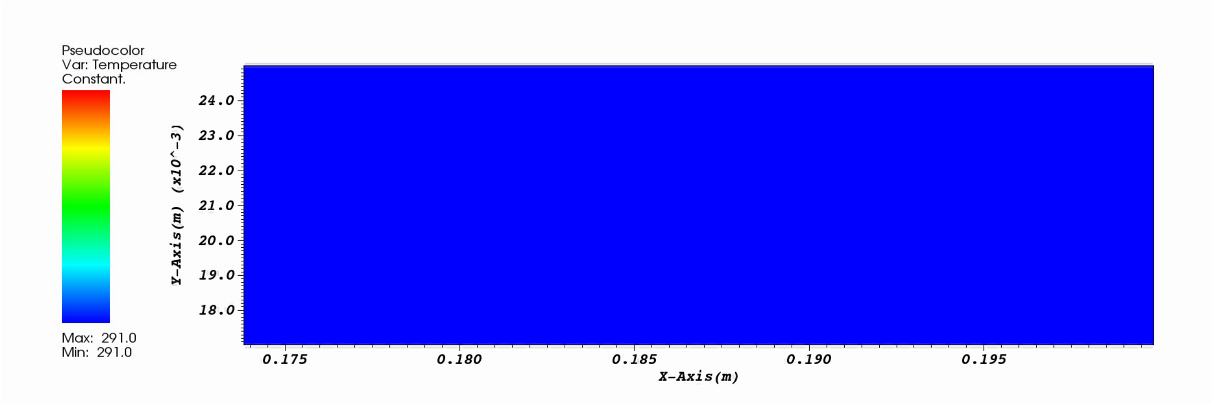

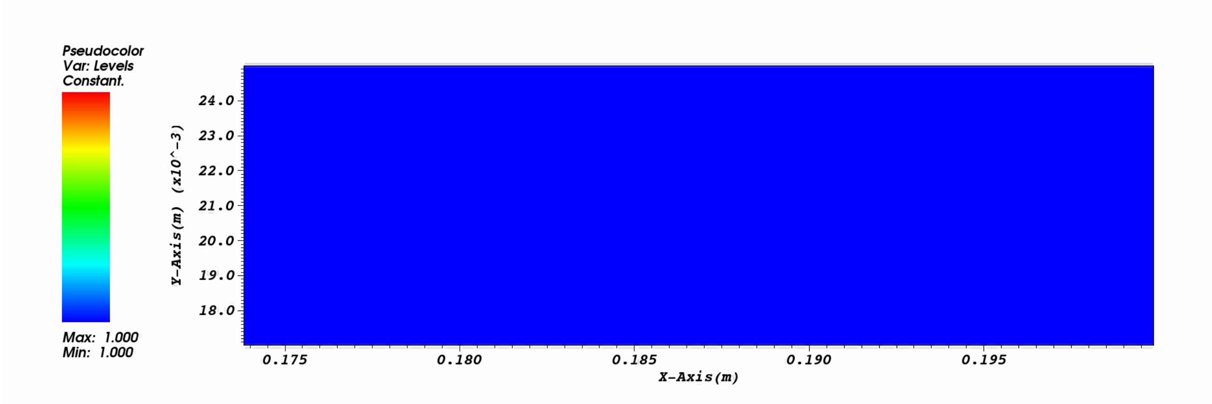

M. Ihme, Y. Sun, RD, *51st AIAA Aerospace Sciences Meeting*, AIAA-2013-0538 ,2013

Reactive case: $H_2 : O_2 : Ar - 15 : 17.85 : 67.15$

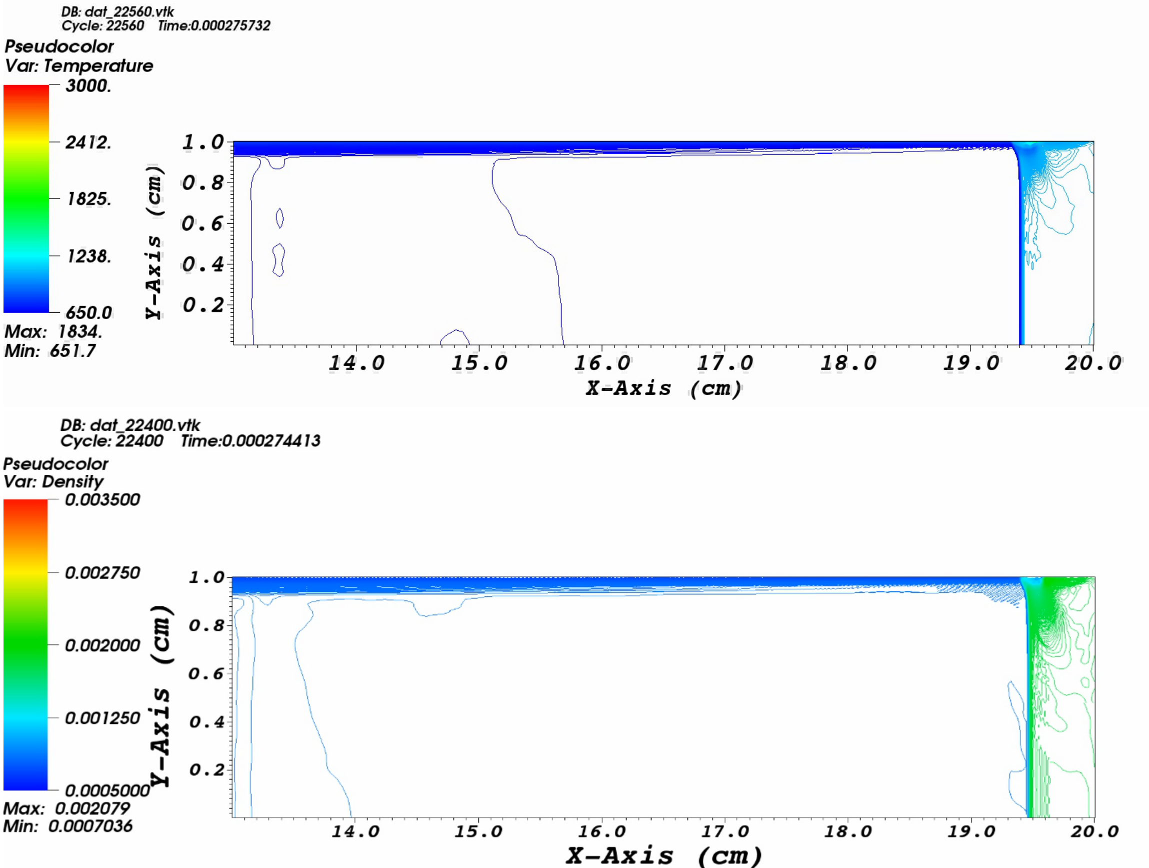

Detonation establishment in a scramjet combustor

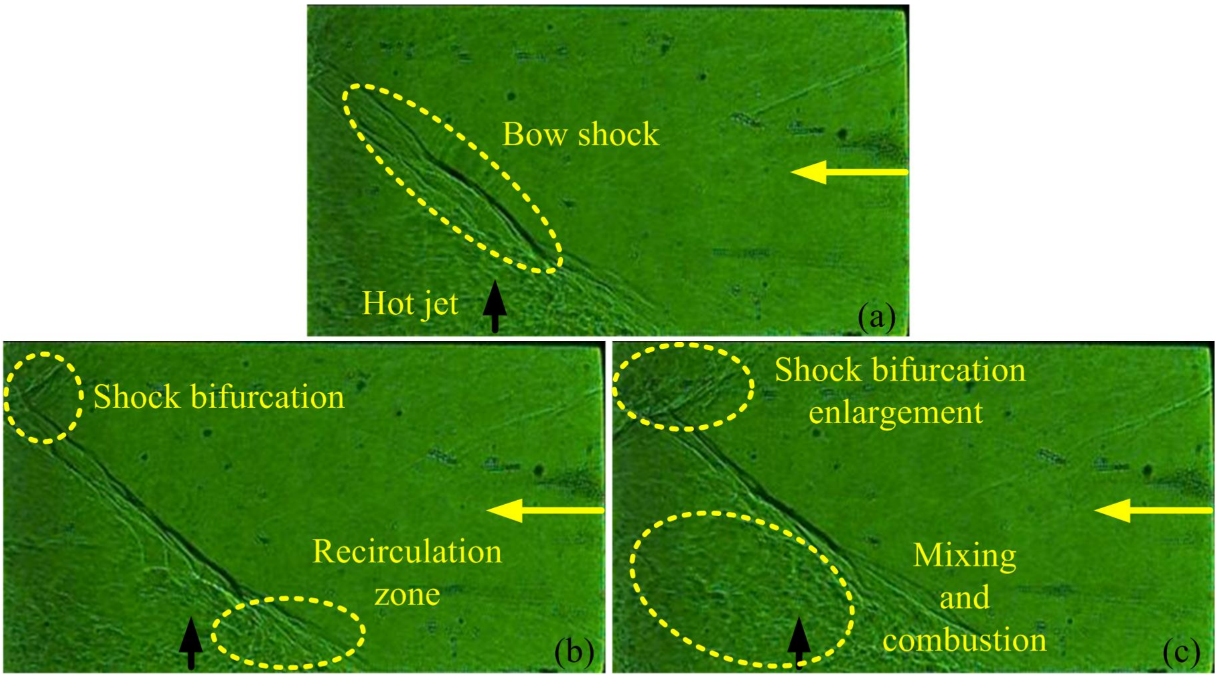

C. Cai, RD, J. Liang, M. Sun, Y. Mahmoudi, *Combust. Flame* 190: 201–215, 2018

Setup 1 – Experiment $\phi = 0.28$

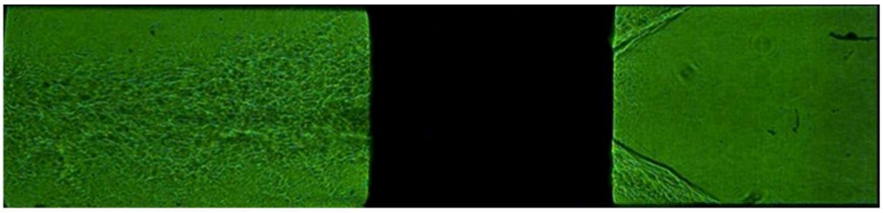

(a)

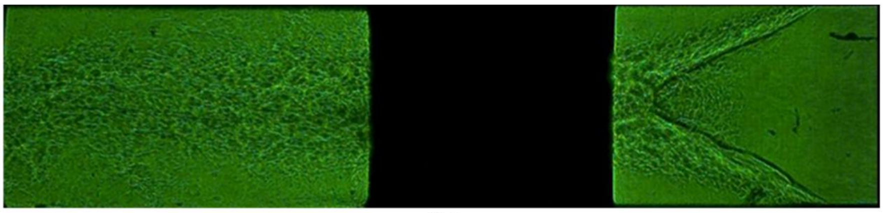

(b)

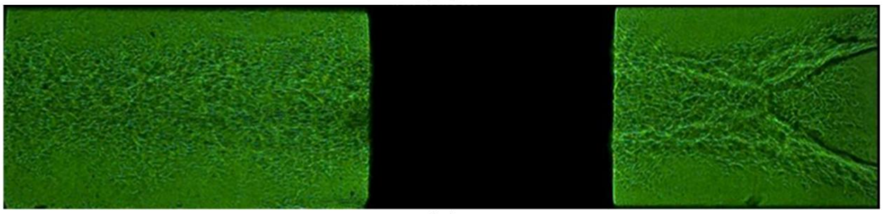

(c)

$\mathrm{H_2 : O_2 : N_2} - 0.56 : 1.0 : 2.9$, $p_0 = 36.1\,\mathrm{kPa}$, $T_0 = 581\,\mathrm{K}$, inflow $V_I = 1532\,\mathrm{m/s}$, $V_{CJ} = 1431\,\mathrm{m/s}$

Setup 1 – Numerical simulation $\phi = 0.28$

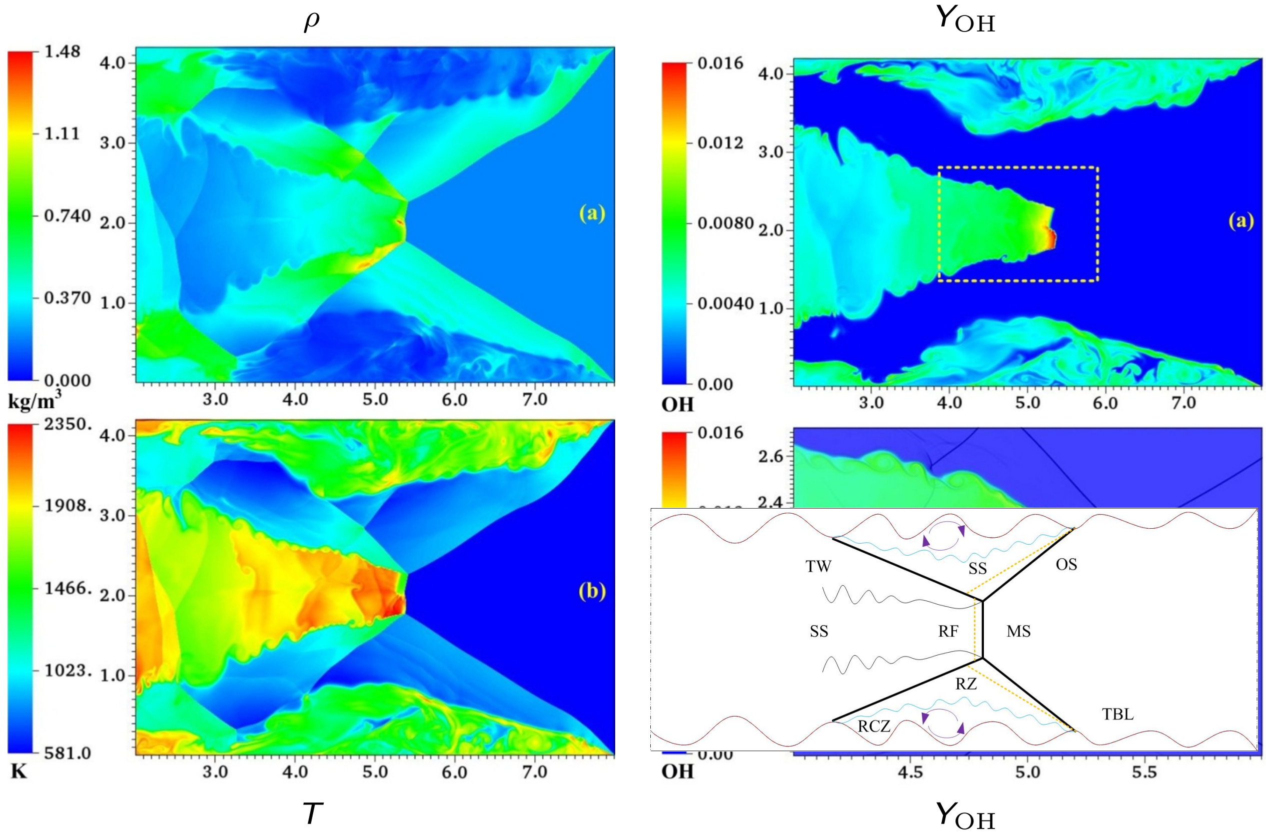

Setup 2 – Experiment $\phi = 0.29$

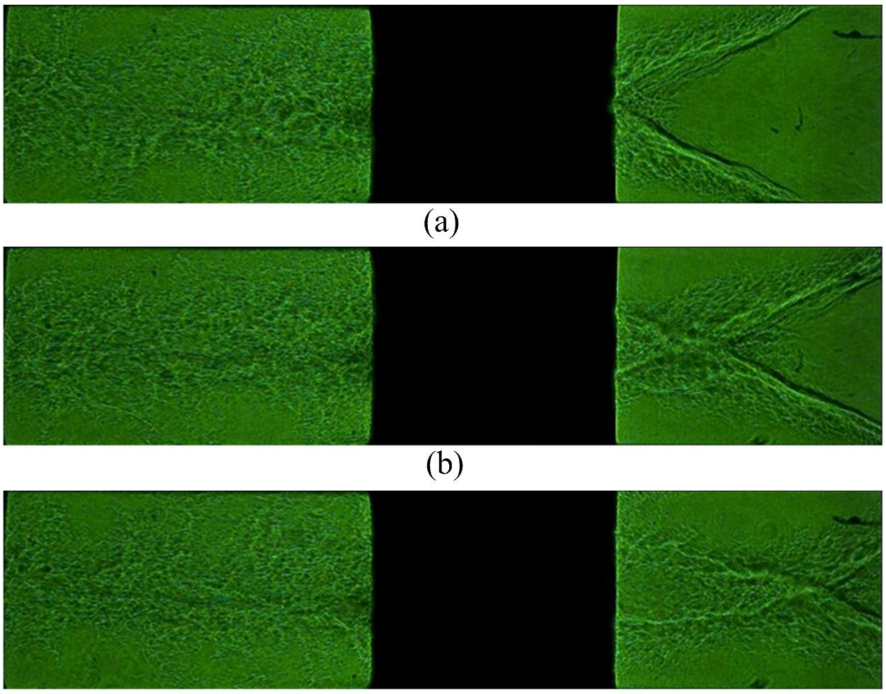

(a) (b) (c)

$\mathrm{H_2 : O_2 : N_2} - 0.58 : 1.0 : 2.9$, $p_0 = 36.1\,\mathrm{kPa}$, $T_0 = 581\,\mathrm{K}$, inflow $V_I = 1532\,\mathrm{m/s}$

Numerical simulation $\phi = 0.29$

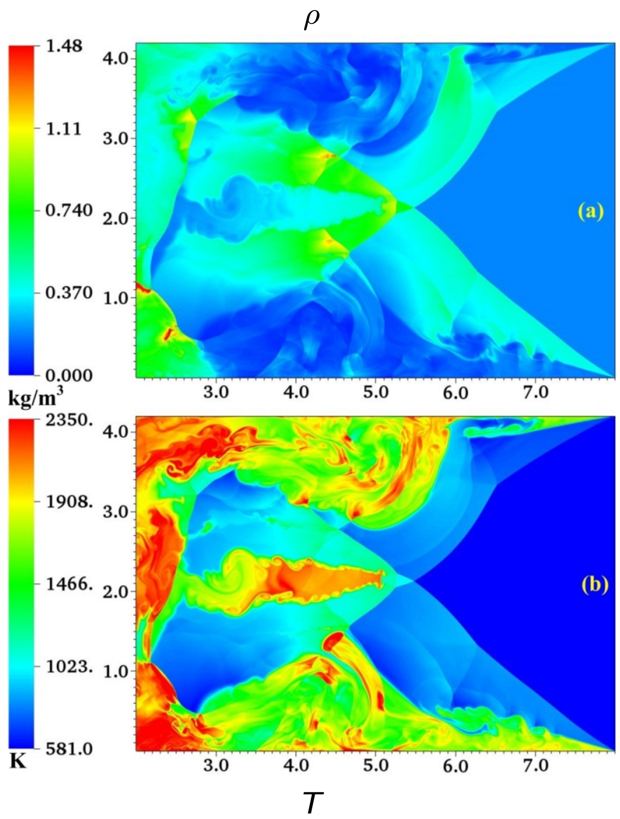

- SAMR simulation with 4 additional levels (2,2,2,2), 137.8 Pts/l_{ig}

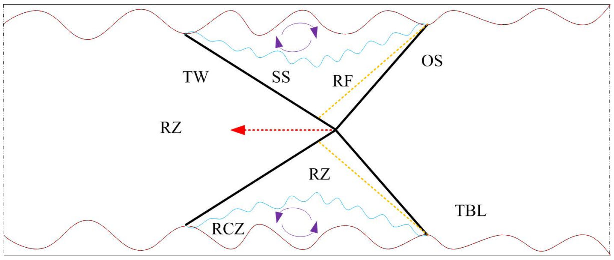

Conclusions – Detonations

- For small mechanisms, detailed detonation structure simulations and accurate DNS are nowadays possible for realistic 2d geometries
- Accurate studies for idealized 3d configurations feasible
- Resolution down to the scale of secondary triple points can be provided on parallel capacity computing systems
- Enabling components:
  - Splitting methods combined with high-resolution FV schemes for hyrodynamic transport
  - SAMR provides a sufficient spatial and temporal resolution. Savings from SAMR for pipe bend simulations: up to >680x
- Future work will concentrate on non-Cartesian and higher order schemes with low numerical dissipation geared to DNS.

References I

[Axdahl et al., 2011] Axdahl, E., Kumar, A., and Wilhite, A. (2011). Study of unsteady, sphere-driven, shock-induced combustion for application to hypervelocity airbreathing propulsio. In *Proc. 47th AIAA/ASME/SAE/SAEE Joint Propulsion Conference & Exhibit*.

[Barton et al., 2013] Barton, P. T., Deiterding, R., Meiron, D. I., and Pullin, D. I. (2013). Eulerian continuum model and adaptive finite-difference method for high-velocity impact and penetration problems. *J. Comput. Phys.*, 240:76–99.

[Bell et al., 1994] Bell, J., Berger, M., Saltzman, J., and Welcome, M. (1994). Three-dimensional adaptive mesh refinement for hyperbolic conservation laws. *SIAM J. Sci. Comp.*, 15(1):127–138.

[Berger, 1986] Berger, M. (1986). Data structures for adaptive grid generation. *SIAM J. Sci. Stat. Comput.*, 7(3):904–916.

[Berger and Colella, 1988] Berger, M. and Colella, P. (1988). Local adaptive mesh refinement for shock hydrodynamics. *J. Comput. Phys.*, 82:64–84.

[Berger and Rigoutsos, 1991] Berger, M. and Rigoutsos, I. (1991). An algorithm for point clustering and grid generation. *IEEE Transactions on Systems, Man, and Cybernetics*, 21(5):1278–1286.

[Cai et al., 2018] Cai, X., Deiterding, R., Liang, J., Sun, M., and Mahmoudi, Y. (2018). Experimental and numerical investigations on propagating modes of detonations: detonation wave/boundary layer interaction. *Combust. Flame*, 190:201–215.

References II

[Cai et al., 2016] Cai, X., Liang, J., Deiterding, R., Che, Y., and Lin, Z. (2016). Adaptive mesh refinement based simulations of three-dimensional detonation combustion in supersonic combustible mixtures with a detailed reaction model. *Int. J. Hydrogen Energy*, 41:3222–3239.

[Cerminara et al., 2018] Cerminara, A., Deiterding, R., and Sandham, N. (2018). Dns of hypersonic flow over porous surfaces with a hybrid method. In *AIAA Aerospace Sciences Meeting, AIAA Science and Technology Forum and Exposition*.

[Cirak et al., 2007] Cirak, F., Deiterding, R., and Mauch, S. P. (2007). Large-scale fluid-structure interaction simulation of viscoplastic and fracturing thin shells subjected to shocks and detonations. *Computers & Structures*, 85(11-14):1049–1065.

[Deiterding, 2003] Deiterding, R. (2003). *Parallel adaptive simulation of multi-dimensional detonation structures*. PhD thesis, Brandenburgische Technische Universität Cottbus.

[Deiterding, 2005] Deiterding, R. (2005). Construction and application of an AMR algorithm for distributed memory computers. In Plewa, T., Linde, T., and Weirs, V. G., editors, *Adaptive Mesh Refinement - Theory and Applications*, volume 41 of *Lecture Notes in Computational Science and Engineering*, pages 361–372. Springer.

[Deiterding, 2009] Deiterding, R. (2009). A parallel adaptive method for simulating shock-induced combustion with detailed chemical kinetics in complex domains. *Computers & Structures*, 87:769–783.

[Deiterding, 2011a] Deiterding, R. (2011a). Block-structured adaptive mesh refinement - theory, implementation and application. *European Series in Applied and Industrial Mathematics: Proceedings*, 34:97–150.

References III

[Deiterding, 2011b] Deiterding, R. (2011b). High-resolution numerical simulation and analysis of Mach reflection structures in detonation waves in low-pressure $\mathrm{h}_2 : \mathrm{o}_2 : \mathrm{ar}$ mixtures: a summary of results obtained with adaptive mesh refinement framework AMROC. *J. Combustion*, 2011:738969.

[Deiterding and Bader, 2005] Deiterding, R. and Bader, G. (2005). High-resolution simulation of detonations with detailed chemistry. In Warnecke, G., editor, *Analysis and Numerics for Conservation Laws*, pages 69–91. Springer.

[Deiterding et al., 2009a] Deiterding, R., Cirak, F., and Mauch, S. P. (2009a). Efficient fluid-structure interaction simulation of viscoplastic and fracturing thin-shells subjected to underwater shock loading. In Hartmann, S., Meister, A., Schäfer, M., and Turek, S., editors, *Int. Workshop on Fluid-Structure Interaction. Theory, Numerics and Applications, Herrsching am Ammersee 2008*, pages 65–80. kassel university press GmbH.

[Deiterding et al., 2007] Deiterding, R., Cirak, F., Mauch, S. P., and Meiron, D. I. (2007). A virtual test facility for simulating detonation- and shock-induced deformation and fracture of thin flexible shells. *Int. J. Multiscale Computational Engineering*, 5(1):47–63.

[Deiterding et al., 2009b] Deiterding, R., Domingues, M. O., Gomes, S. M., Roussel, O., and Schneider, K. (2009b). Adaptive multiresolution or adaptive mesh refinement? A case study for 2D Euler equations. *European Series in Applied and Industrial Mathematics: Proceedings*, 29:28–42.

References IV

[Deiterding et al., 2006] Deiterding, R., Radovitzky, R., Mauch, S. P., Noels, L., Cummings, J. C., and Meiron, D. I. (2006). A virtual test facility for the efficient simulation of solid materials under high energy shock-wave loading. *Engineering with Computers*, 22(3-4):325–347.

[Deiterding and Wood, 2016] Deiterding, R. and Wood, S. L. (2016). Predictive wind turbine simulation with an adaptive lattice Boltzmann method for moving boundaries. *J. Phys. Conf. Series*, 753:082005.

[Feldhusen et al., 2016] Feldhusen, K., Deiterding, R., and Wagner, C. (2016). A dynamically adaptive lattice Boltzmann method for thermal convection problems. *J. Applied Math. and Computer Science*, 26:735–747.

[Fragner and Deiterding, 2016] Fragner, M. M. and Deiterding, R. (2016). Investigating cross-wind stability of high speed trains with large-scale parallel cfd. *Int. J. Comput. Fluid Dynamics*, 30:402–407.

[Gomes et al., 2015] Gomes, A. K. F., Domingues, M. O., Schneider, K., Mendes, O., and Deiterding, R. (2015). An adaptive multiresolution method for ideal magnetohydrodynamics using divergence cleaning with parabolic-hyperbolic correction. *Applied Numerical Mathematics*, 95:199–213.

[Harten, 1983] Harten, A. (1983). High resolution schemes for hyperbolic conservation laws. *J. Comput. Phys.*, 49:357–393.

[Harten and Hyman, 1983] Harten, A. and Hyman, J. M. (1983). Self-adjusting grid methods for one-dimensional hyperbolic conservation laws. *J. Comput. Phys.*, 50:235–269.

References V

[Jachimowski, 1988] Jachimowski, C. J. (1988). An analytical study of the hydrogen-air reaction mechanism with application to scramjet combustion. Technical Report TP-2791, NASA.

[Lehr, 1972] Lehr, H. F. (1972). Experiments on shock-induced combustion. *Astronautica Acta*, 17:589–597.

[Lombardini and Deiterding, 2010] Lombardini, M. and Deiterding, R. (2010). Large-eddy simulation of Richtmyer-Meshkov instability in a converging geometry. *Physics of Fluids*, 22(9):091112.

[Mauch, 2003] Mauch, S. P. (2003). *Efficient Algorithms for Solving Static Hamilton-Jacobi Equations*. PhD thesis, California Institute of Technology.

[Pantano et al., 2007] Pantano, C., Deiterding, R., Hill, D. J., and Pullin, D. I. (2007). A low-numerical dissipation patch-based adaptive mesh refinement method for large-eddy simulation of compressible flows. *J. Comput. Phys.*, 221(1):63–87.

[Perotti et al., 2013] Perotti, L. E., Deiterding, R., Inaba, K., Shepherd, J. E., and Ortiz, M. (2013). Elastic response of water-filled fiber composite tubes under shock wave loading. *Int. J. Solids and Structures*, 50(3-4):473–486.

[Quirk, 1994] Quirk, J. J. (1994). A contribution to the great Riemann solver debate. *Int. J. Numer. Meth. Fluids*, 18:555–574.

[Sanders et al., 1998] Sanders, R., Morano, E., and Druguett, M.-C. (1998). Multidimensional dissipation for upwind schemes: Stability and applications to gas dynamics. *J. Comput. Phys.*, 145:511–537.

References VI

[Souza Lopes et al., 2018] Souza Lopes, M. M., Deiterding, R., Gomes, A. K. F., Mendes, O., and Domingues, M. O. (2018). An ideal compressible magnetohydrodynamic solver with parallel block-structured adaptive mesh refinement. *Computers & Fluids*. in press.

[Wan et al., 2017] Wan, Q., Jeon, H., Deiterding, R., and Eliasson, V. (2017). Numerical and experimental investigation of oblique shock wave reflection off a water wedge. *J. Fluid Mech.*, 826:732–758.

[Westbrook, 1982] Westbrook, C. K. (1982). Chemical kinetics of hydrocarbon oxidation in gaseous detonations. *Combust. Flame*, 46:191–210.

[Yungster and Radhakrishnan, 1996] Yungster, S. and Radhakrishnan, K. (1996). A fully implicit time accurate method for hypersonic combustion: application to shock-induced combustion instability. *Shock Waves*, 5:293–303.

[Ziegler et al., 2011] Ziegler, J. L., Deiterding, R., Shepherd, J. E., and Pullin, D. I. (2011). An adaptive high-order hybrid scheme for compressive, viscous flows with detailed chemistry. *J. Comput. Phys.*, 230(20):7598–7630.

Riemann solver for combustion: carbuncle fix

Entropy corrections [Harten, 1983] [Harten and Hyman, 1983]

1. $|\tilde{s}_\iota| = \begin{cases} |s_\iota| & \text{if} |s_\iota| \ge 2\eta \\ \frac{|s_\iota^2|}{4\eta} + \eta & \text{otherwise} \end{cases}$

   $\eta = \frac{1}{2} \max_\iota \left\{ |s_\iota(\mathbf{q}_R) - s_\iota(\mathbf{q}_L)| \right\}$

2. Replace $|s_\iota|$ by $|\tilde{s}_\iota|$ only if $s_\iota(\mathbf{q}_L) < 0 < s_\iota(\mathbf{q}_R)$

2D modification of entropy correction [Sanders et al., 1998]:

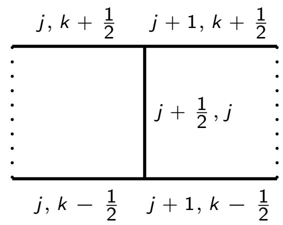

$$\tilde{\eta}_{j+1/2,k} = \max\left\{\eta_{j+1/2,k}, \eta_{j,k-1/2}, \ \eta_{j,k+1/2}, \eta_{j+1,k-1/2}, \eta_{j+1,k+1/2}\right\}$$

Carbuncle phenomenon

- [Quirk, 1994]
- Test from [Deiterding, 2003]

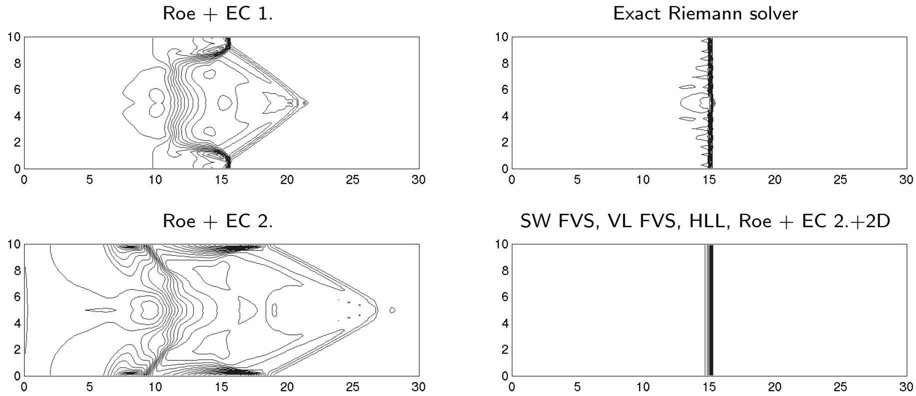

Clustering by signatures

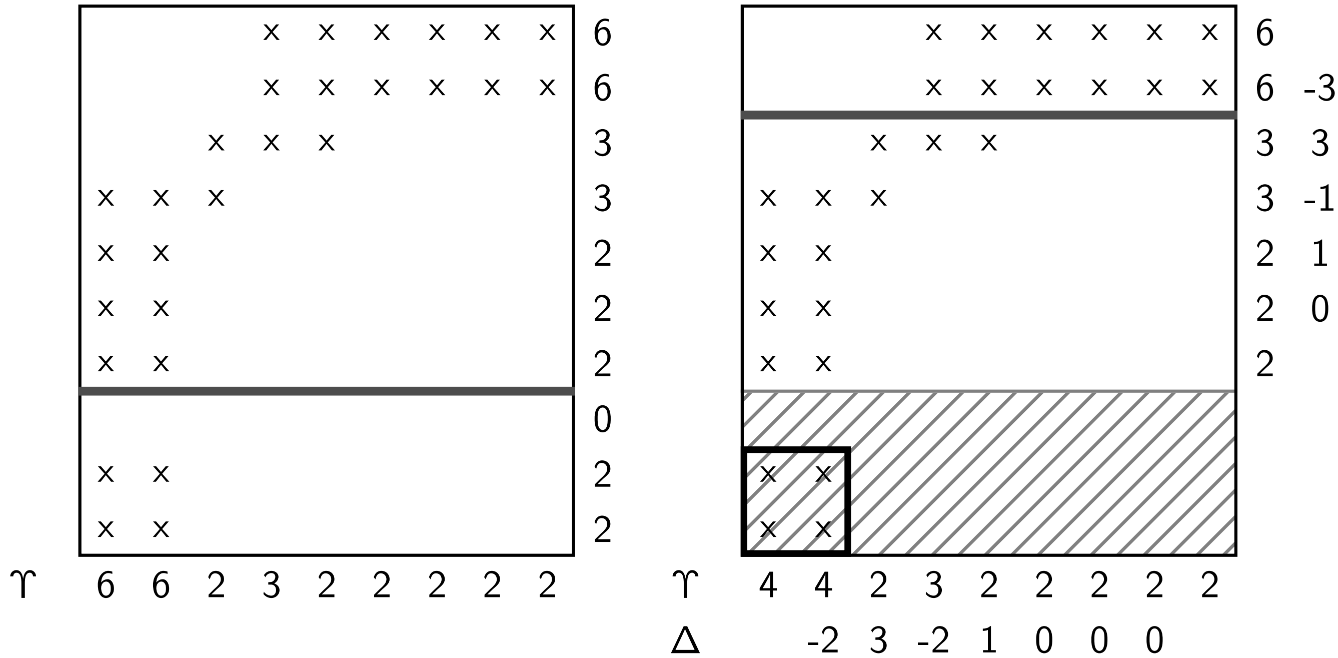

Υ Flagged cells per row/column

Δ Second derivative of Υ, $\Delta = \Upsilon_{\nu+1} - 2\,\Upsilon_\nu + \Upsilon_{\nu-1}$

Technique from image detection: [Bell et al., 1994], see also [Berger and Rigoutsos, 1991], [Berger, 1986]

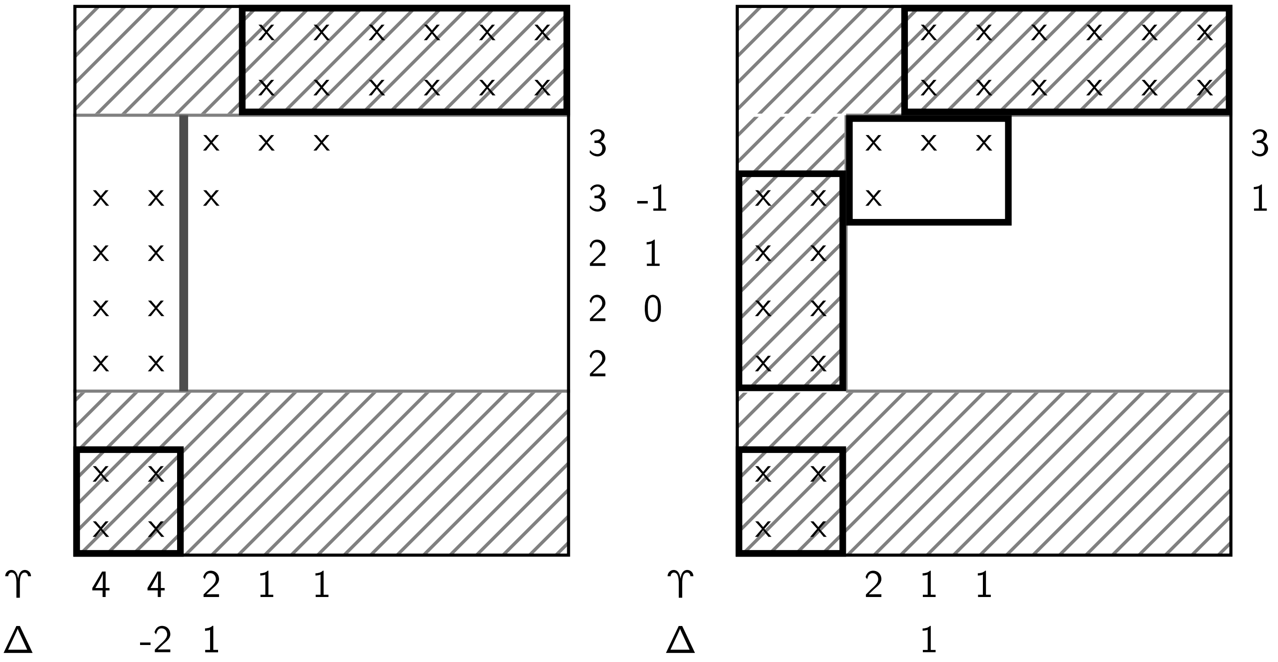

Recursive generation of $\breve{G}_{l,m}$

1. 0 in Υ
2. Largest difference in Δ
3. Stop if ratio between flagged and unflagged cell $> \eta_{tol}$

Detonation and hypersonics simulation with AMROC – Part II

Ralf Deiterding

Aerodynamics and Flight Mechanics Research Group
University of Southampton
Highfield Campus
Southampton SO17 1BJ, UK
Email: r.deiterding@soton.ac.uk

Xiamen
23rd July, 2019

Outline

Two-temperature solver
Thermodynamic model
Cartesian results

Two-temperature mapped mesh solver
Mapped mesh treatment
Non-cartesian results and comparison

DNS with a hybrid method
Higher-order hybrid methods

Summary
Conclusions

Thermodynamic Model

The two temperature thermodynamic model is used to model the thermodynamic nonequilibrium,

$$e_s(T_{tr}, T_{ve}) = e_s^t(T_{tr}) + e_s^r(T_{tr}) + e_s^v(T_{ve}) + e_s^{el}(T_{ve}) + e_s^0$$

- Computationally efficient,
- Widely used,
- Integrated into the open source library Mutation++ [Scoggins and Magin, 2014].

The internal energies are calculated within the Mutation++ library using the Rigid-Rotator Harmonic-Oscillator (RRHO) model.

Governing Equations

The two temperature thermodynamic model has been implemented using the equations,

$$\frac{\partial \mathbf{Q}}{\partial t} + \frac{\partial \mathbf{F}}{\partial x} + \frac{\partial \mathbf{G}}{\partial y} = \mathbf{W}$$

where,

$$\mathbf{Q} = \begin{bmatrix} \rho_1 \\ \vdots \\ \rho_{N_s} \\ \rho u \\ \rho v \\ \rho e^{ve} \\ \rho E \end{bmatrix}, \quad \mathbf{F} = \begin{bmatrix} \rho_1 u \\ \vdots \\ \rho_{N_s} u \\ \rho u^2 + p \\ \rho v u \\ \rho e^{ve} u \\ (\rho E + p) u \end{bmatrix}, \quad \mathbf{G} = \begin{bmatrix} \rho_1 v \\ \vdots \\ \rho_{N_s} v \\ \rho u v \\ \rho v^2 + p \\ \rho e^{ve} v \\ (\rho E + p) v \end{bmatrix}, \quad \mathbf{W} = \begin{bmatrix} \dot{w}_1 \\ \vdots \\ \dot{w}_{N_s} \\ 0 \\ 0 \\ Q_{ve} \\ 0 \end{bmatrix}.$$

Source Terms

The net species production rates,

$$\dot{w}_s = M_s \sum_{r=1}^{N_r} (\beta_{sr} - \alpha_{sr}) \left[k_{f,r} \prod_{i=1}^{N_s} \left(\frac{\rho_i}{M_i} \right)^{\alpha_{ir}} - k_{b,r} \prod_{i=1}^{N_s} \left(\frac{\rho_i}{M_i} \right)^{\beta_{ir}} \right] \ ,$$

$$k_{f,r}(T_c) = A_{f,r} T_c^{\eta_{f,r}} \exp\left[-\theta_r / T_c\right] \ ,$$

and the energy transfer rate (neutral mixture),

$$Q_{ve} = \sum_s Q_s^{T-V} + Q_s^{C-V} + Q_s^{C-el} \ ,$$

$$Q_s^{T-V} = \rho_s \frac{e_s^v(T_{tr}) - e_s^v}{\tau_{V,s}^{T-V}} \ ,$$

$$Q_s^{C-V} = c_1 \dot{w}_s e_s^v, \quad Q_s^{C-el} = c_1 \dot{w}_s e_s^{el} \ ,$$

are both calculated using the Mutation++ library.

Numerical Integration

Finite volume method with two flux schemes implemented,

- Van Leer's flux vector splitting method [van Leer, 1982],
- The AUSM scheme [Liou and Steffen Jr, 1993].

Second order in space and time,

- The MUSCL-Hancock scheme is used for the fluxes.
- Strang splitting is used to integrate the source term.

Double Wedge

Simulation of a double wedge in a high enthalpy flow of air [Pezzella et al., 2015].

T_∞	p_∞	U_∞	M_∞	L_1	θ_1	L_2	θ_2
710 K	0.78 kPa	3812 m/s	7.14	50.8 mm	30°	25.4 mm	55°

Table: Double wedge geometry and experimental conditions.

- Five species mixture of air.
- Initial 200×200 cell mesh, with 3 levels of refinement.
- Embedded boundary used to define geometry.
- Van Leer flux scheme.
- Physical time of 242 μs.

Double Wedge

The temperature and mass fraction of atomic oxygen.

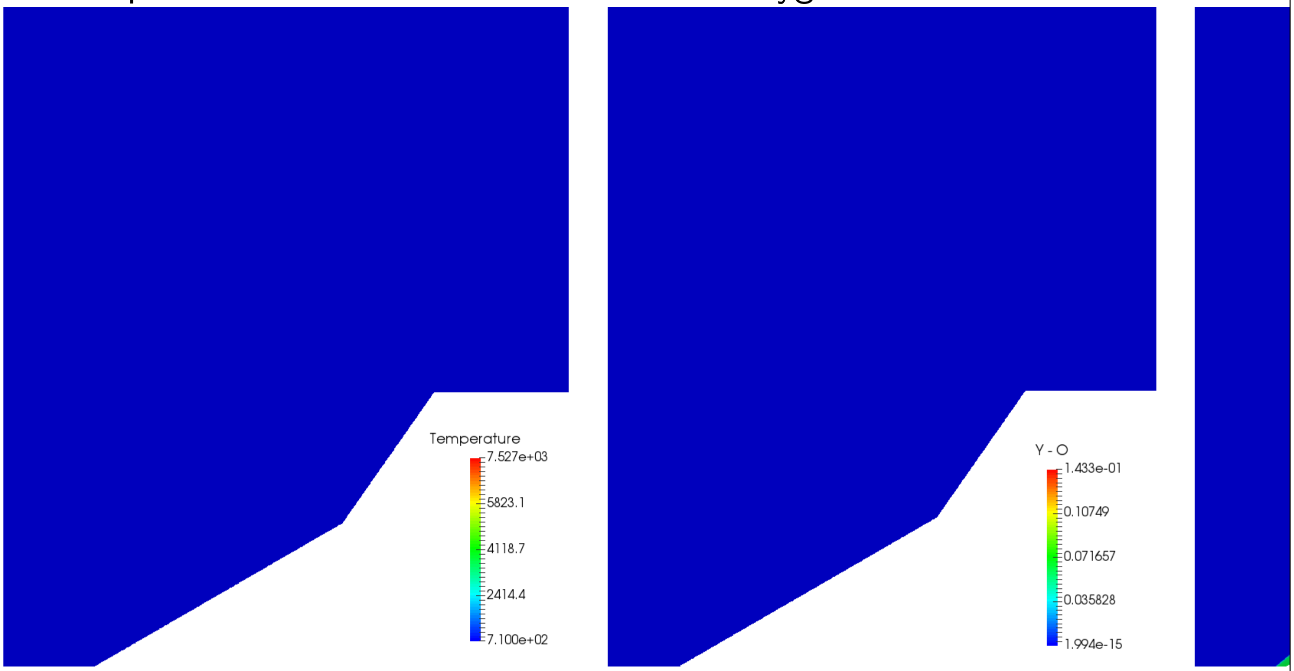

$t = 242 \mu\text{secs}.$

Double Wedge

The mesh was refined using pressure and density gradients.

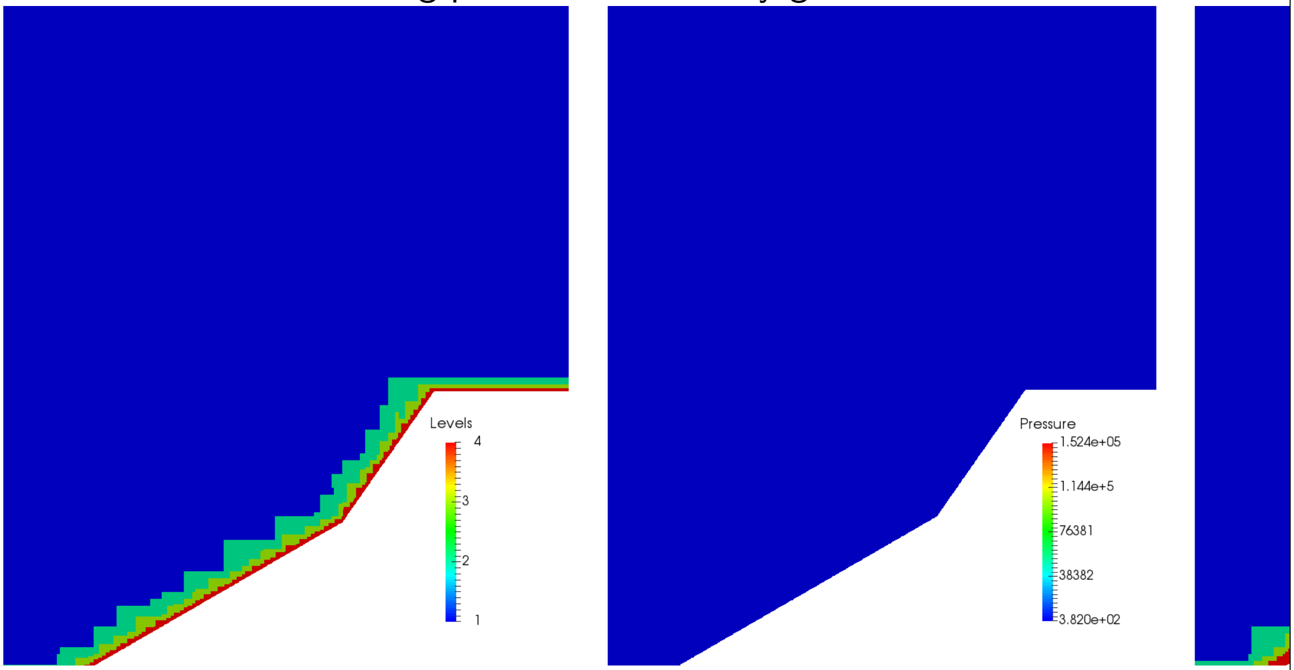

$t = 242\,\mu\mathrm{secs}.$

Double Wedge

Dynamic load balancing distributes the cells across the processors.

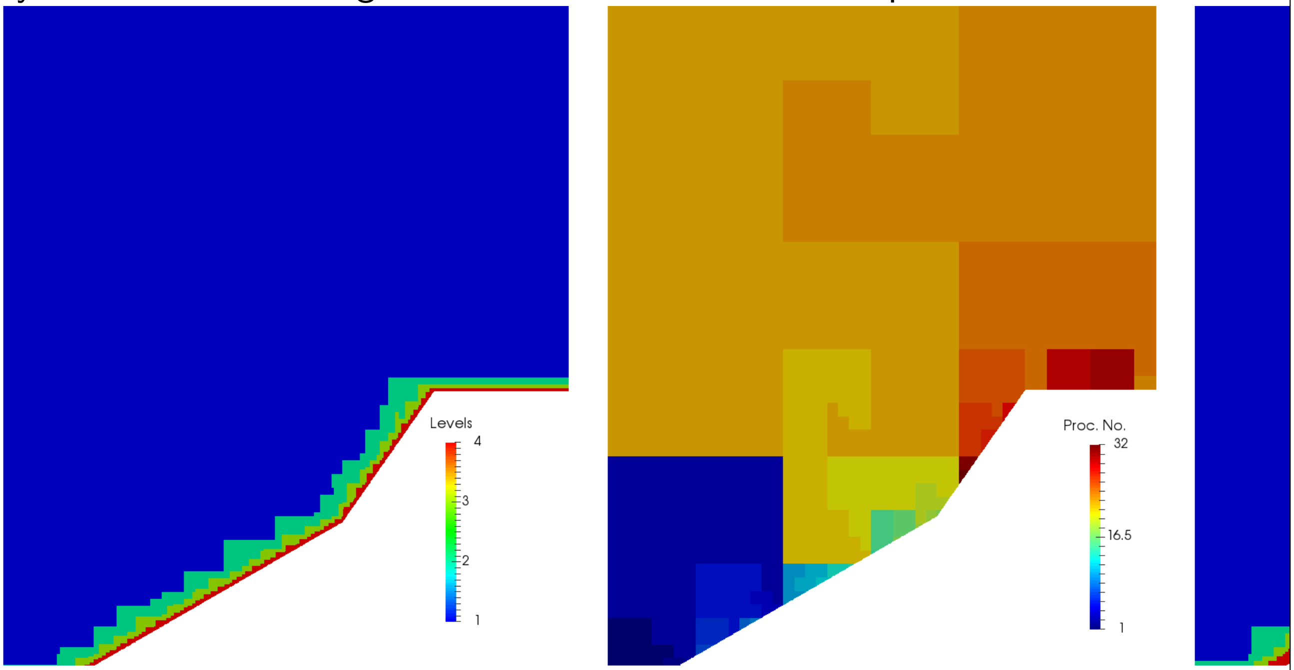

$t = 242\,\mu\text{secs}.$

Double Wedge

The AMR enables the flow features to be captured in detail.

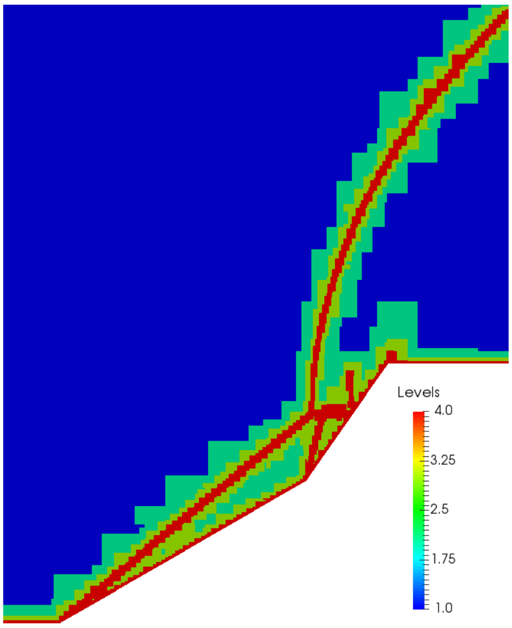

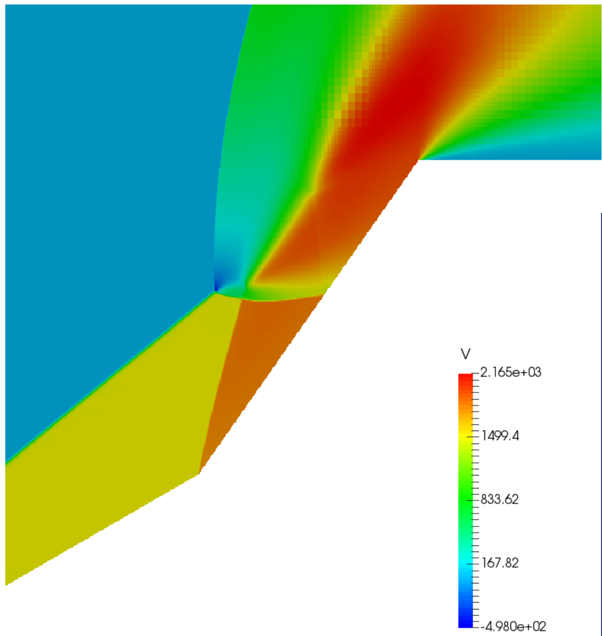

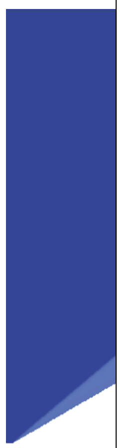

The schlieren image is taken from [Pezzella et al., 2015].

Mapped Solution Update

Within the AMROC-Clawpack framework, the solution is stored in physical (x, y) space and the fluxes are mapped from computational (ξ, η) space.
Using dimensional splitting the solution update is given by:

$$\mathbf{Q}^{*}_{i,j} = \mathbf{Q}^{n}_{i,j} - \frac{\Delta t}{\Delta \xi}\left[\left(\hat{\mathbf{F}} - \hat{\mathbf{F}}^{v}\right)_{i+1,j} - \left(\hat{\mathbf{F}} - \hat{\mathbf{F}}^{v}\right)_{i,j}\right]\frac{\Delta\eta\Delta\xi}{V_{i,j}},$$

$$\mathbf{Q}^{n+1}_{i,j} = \mathbf{Q}^{*}_{i,j} - \frac{\Delta t}{\Delta \eta}\left[\left(\hat{\mathbf{G}} - \hat{\mathbf{G}}^{v}\right)_{i,j+1} - \left(\hat{\mathbf{G}} - \hat{\mathbf{G}}^{v}\right)_{i,j}\right]\frac{\Delta\eta\Delta\xi}{V_{i,j}}.$$

where $V_{i,j}$ is the volume of cell i, j in physical space. $\hat{\mathbf{F}}$, $\hat{\mathbf{F}}^{v}$, $\hat{\mathbf{G}}$, $\hat{\mathbf{G}}^{v}$ are the physical fluxes **per computational unit length**.

Mapped Mesh Computation

In the mapped mesh computations, the flux is transformed to align with the cell face,

$$\hat{\mathbf{F}} = T^{-1}\mathbf{F}_n(T\,\mathbf{Q}_l, T\,\mathbf{Q}_r)\,,$$

where T is the transformation matrix,

$$T = \begin{bmatrix} 1 & 0 & 0 & 0 & 0 & 0 & 0 \\ 0 & \ddots & 0 & 0 & 0 & 0 & 0 \\ 0 & 0 & 1 & 0 & 0 & 0 & 0 \\ 0 & 0 & 0 & \hat{n}^x & \hat{n}^y & 0 & 0 \\ 0 & 0 & 0 & -\hat{n}^y & \hat{n}^x & 0 & 0 \\ 0 & 0 & 0 & 0 & 0 & 1 & 0 \\ 0 & 0 & 0 & 0 & 0 & 0 & 1 \end{bmatrix}.$$

Mapped Inviscid Fluxes

The inviscid fluxes per computational unit length are found by:

- Rotating the momentum components to be normal to the face,
- Calculating the flux with the rotated solution vectors,
- Rotating the solution vector back,
- Scaling the flux using the ratio of the computational face to the mapped face

In the ξ directional sweep, this gives

$$\mathbf{F}_{i-1/2,j} = T^{-1}_{i-1/2,j}\mathbf{F}_n\big(T_{i-1/2,j}\mathbf{Q}_{i-1,j},\, T_{i-1/2,j}\mathbf{Q}_{i,j}\big)\,.$$

where T is the rotation matrix used to rotate the momentum components, and $\mathbf{F}_n$ is the normal flux through the face.
The scaling is given by:

$$\hat{\mathbf{F}}_{i,j} = \frac{|\mathbf{n}_{i-1/2,j}|}{\Delta\eta}\,\mathbf{F}_{i-1/2,j}\,,$$

Mapped Viscous Fluxes

The physical viscous flux per computational unit length in the ξ directional sweep is given by,

$$\hat{\mathbf{F}}^v_{i-1/2,j} = \frac{|\mathbf{n}_{i-1/2,j}|}{\Delta\eta}\left[(\mathbf{F}^v\hat{n}^x)_{i-1/2,j} + (\mathbf{G}^v\hat{n}^y)_{i-1/2,j}\right],$$

To calculate the derivatives needed for $\mathbf{F}^v$ and $\mathbf{G}^v$, one must use

$$\frac{\partial\phi}{\partial x} = \left(\frac{\partial\phi}{\partial\xi}\right)\left(\frac{\partial\xi}{\partial x}\right) + \left(\frac{\partial\phi}{\partial\eta}\right)\left(\frac{\partial\eta}{\partial x}\right),$$

and,

$$\frac{\partial\phi}{\partial y} = \left(\frac{\partial\phi}{\partial\xi}\right)\left(\frac{\partial\xi}{\partial y}\right) + \left(\frac{\partial\phi}{\partial\eta}\right)\left(\frac{\partial\eta}{\partial y}\right).$$

Boundary Conditions

For wall boundary conditions the ghost cell values are set by first transforming the domain variables,

$$\hat{\mathbf{Q}} = T_w \mathbf{Q}_{\mathrm{dom.}} \, .$$

Then setting the ghost cell variables using interpolation,

$$\hat{\mathbf{Q}}^{\rho u}_{\mathrm{gc}} = \frac{-\frac{d_{gw}}{d_{gd}}\hat{\mathbf{Q}}^{\rho u}}{1 - \frac{d_{gw}}{d_{gd}}} \, ,$$

and

$$\hat{\mathbf{Q}}^{\rho v}_{\mathrm{gc}} = \hat{\mathbf{Q}}^{\rho v} \ \ \mathrm{slip}, \quad \hat{\mathbf{Q}}^{\rho v}_{\mathrm{gc}} = \frac{-\frac{d_{gw}}{d_{gd}}\hat{\mathbf{Q}}^{\rho v}}{1 - \frac{d_{gw}}{d_{gd}}} \ \ \mathrm{no-slip},$$

Then rotating the ghost cell values using the inverse transformation,

$$\mathbf{Q}_{\mathrm{gc}} = T_w^{-1} \hat{\mathbf{Q}}_{\mathrm{gc}} \, .$$

CFL condition

The time step must be adjusted to account for the changes in mesh size. The Courant-Friedrichs-Lewy (CFL) condition can be written as [Moukalled et al., 2015],

$$\sum_f \left[\frac{\lambda_f^v |\mathbf{n}|_f}{d_f} + \lambda_f^c |\mathbf{n}|_f \right] - \frac{V_c}{\Delta t} \leq 0 \,,$$

where λ_f^v and λ_f^c are the viscous and convective spectral radii, respectively, and d_f is the distance between the cell centres either side of the face.

Rearranging the above equation gives,

$$\frac{\Delta t}{V_c} \sum_f \left[\frac{\lambda_f^v}{d_f} + \lambda_f^c \right] |\mathbf{n}|_f \leq 1 \,.$$

CFL Condition

With dimensional splitting, the CFL condition must be evaluated in each dimension separately, giving,

$$\max\left(\left[\frac{\lambda^v_{i-1/2,j}}{d_{i-1/2,j}}+\lambda^c_{i-1/2,j}\right]|\mathbf{n}|_{i-1/2,j}+\left[\frac{\lambda^v_{i+1/2,j}}{d_{i+1/2,j}}+\lambda^c_{i+1/2,j}\right]|\mathbf{n}|_{i+1/2,j}\,,\right.$$
$$\left.\left[\frac{\lambda^v_{i,j-1/2}}{d_{i,j-1/2}}+\lambda^c_{i,j-1/2}\right]|\mathbf{n}|_{i,j-1/2}+\left[\frac{\lambda^v_{i,j+1/2}}{d_{i,j+1/2}}+\lambda^c_{i,j+1/2}\right]|\mathbf{n}|_{i,j+1/2}\right)\frac{\Delta t}{V_c}\le 1\,.$$

Hypersonic Sphere

Simulations of a half inch sphere travelling at hypersonic speeds in air [Lobb, 1964].

Mach number range between 8.4 and 16.1, with $p_\infty = 1333\,\mathrm{Pa}$ and $T_\infty = 293\,\mathrm{K}$.

The shock standoff distance was measured at each condition.

The shock standoff distance is used to validate the non-equilibrium model.

Validation of the axi-symmetric source term.

$$\mathbf{W}_{\mathrm{axi}} = -\frac{1}{y}\begin{bmatrix} \rho_1 v \\ \vdots \\ \rho_N v \\ \rho u v \\ \rho v^2 \\ (\rho E + p) v \end{bmatrix}$$

Hypersonic Sphere

Computed shock standoff distances compared with experimental data.

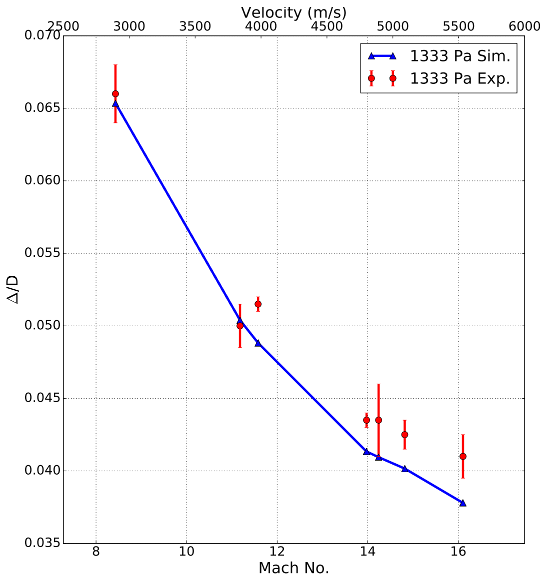

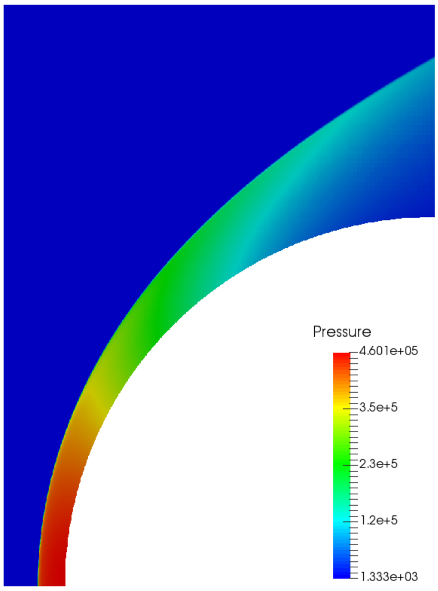

Hypersonic Sphere

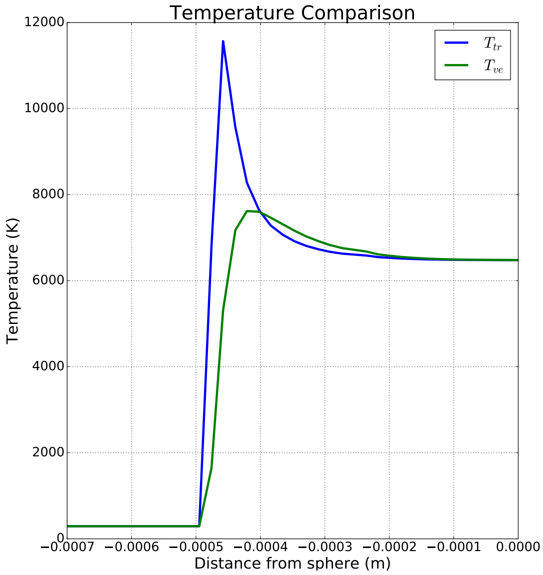

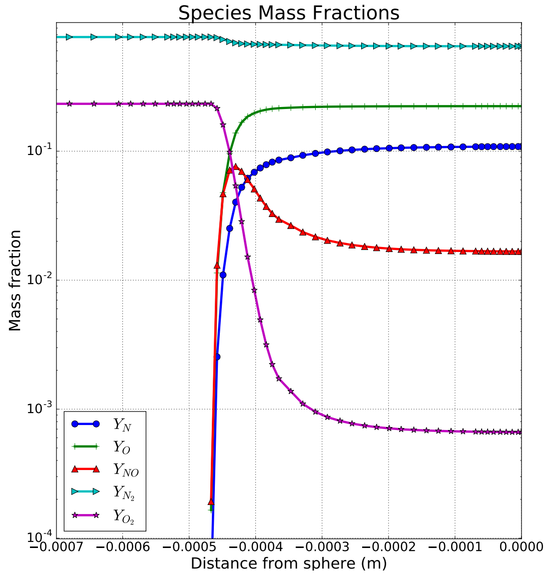

Mapped Mesh Computation

Experiments of a cylinder in hypersonic flow [Hornung, 1972] were simulated with the mapping and initial conditions given by,

$$x = \xi \cos(\eta), \quad y = -\xi \sin(\eta).$$

Radius	Y_{N_2}	Y_N	T_∞	p_∞	U_∞	M_∞
0.0127 m	0.927	0.073	1833 K	2.91 kPa	5590 $\mathrm{m/s}$	6.14

Table: Cylinder geometry and freestream conditions

The implementation was verified by comparing a mapped computation with a embedded boundary computation.

Mapped Mesh Computation

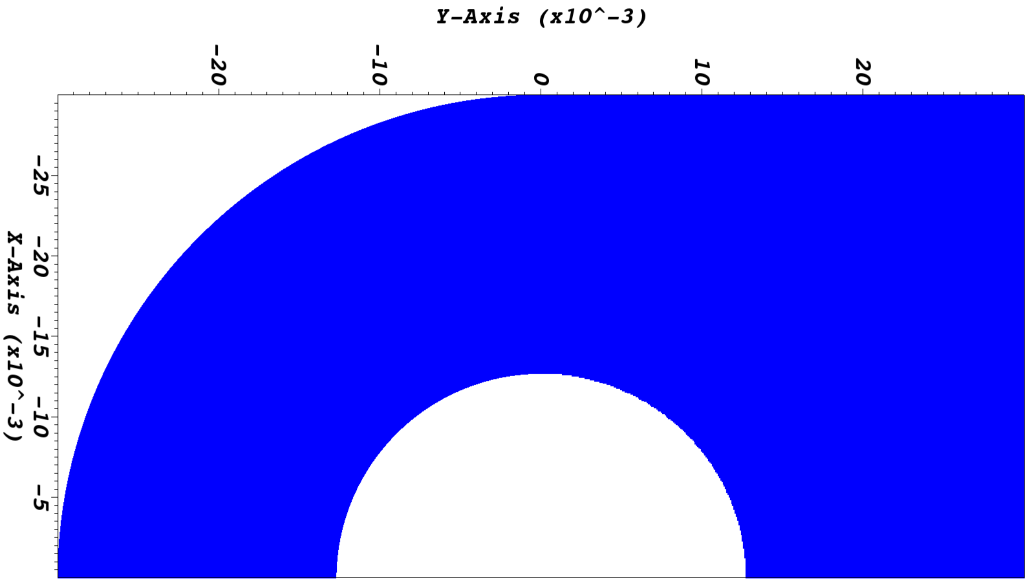

$t = 100\,\mu\mathrm{sec}$

Mapped Mesh Computation

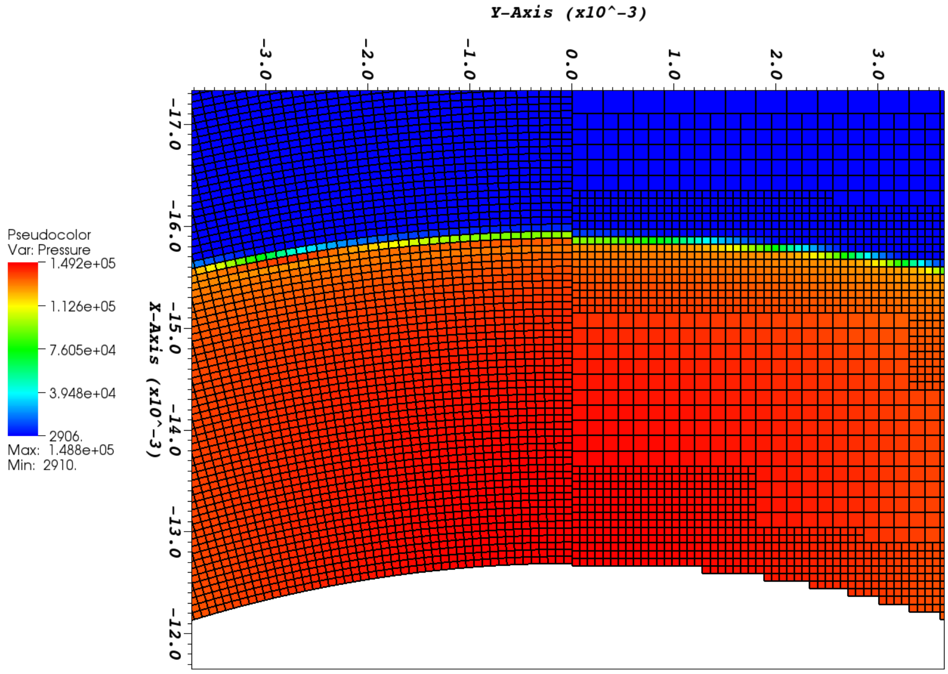

Viscous Computations

Preliminary results have been obtained for computations including the viscous flux vectors,

$$\frac{\partial \mathbf{Q}}{\partial t} + \frac{\partial \left(\mathbf{F} - \mathbf{F}^v\right)}{\partial x} + \frac{\partial \left(\mathbf{G} - \mathbf{G}^v\right)}{\partial y} = \mathbf{W}$$

where,

$$\mathbf{F}^v = \begin{bmatrix} -J_{x,1} \\ \vdots \\ -J_{x,N_s} \\ \tau_{x,x} \\ \tau_{y,x} \\ \kappa_{ve}\frac{\partial T_{ve}}{\partial x} - \sum_{s=1}^{N_s} J_{x,s} e_{ve} \\ \kappa_{tr}\frac{\partial T_{tr}}{\partial x} + \kappa_{ve}\frac{\partial T_{ve}}{\partial x} + u\tau_{x,x} + v\tau_{y,x} - \sum_{s=1}^{N_s} J_{x,s} h_s \end{bmatrix}.$$

and a similar expression is obtained for $\mathbf{G}^v$.

Viscous Computations

The species diffusion uses a modified version of Fick's diffusion law [Sutton and Gnoffo, 1998],

$$J_{x,s} = -\rho D_s \frac{\partial Y_s}{\partial x} - Y_s \sum_{r=1}^{N_s} (-\rho D_r \frac{\partial Y_r}{\partial x}) \,.$$

The viscous stress tensor, $\tau_{i,j}$ is given by,

$$\tau_{i,j} = \mu \left(\frac{\partial u_i}{\partial x_j} + \frac{\partial u_j}{\partial x_i} \right) - \delta_{i,j} \frac{2}{3} \mu \nabla \cdot \mathbf{u} \,,$$

where $\delta_{i,j}$ is the Kronecker delta.

The diffusion coefficients, the viscosity and the thermal conductivities are all calculated within the Mutation++ library.

Viscous Computations

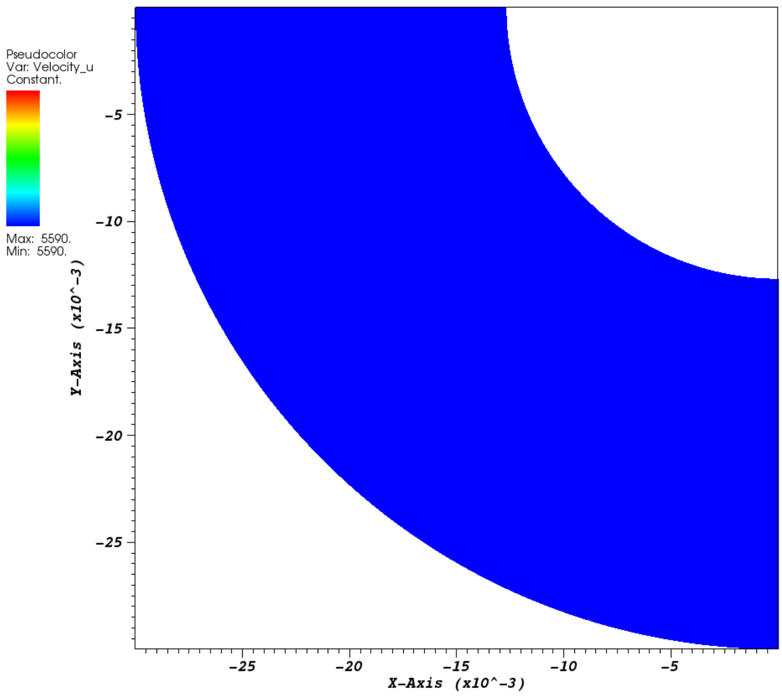

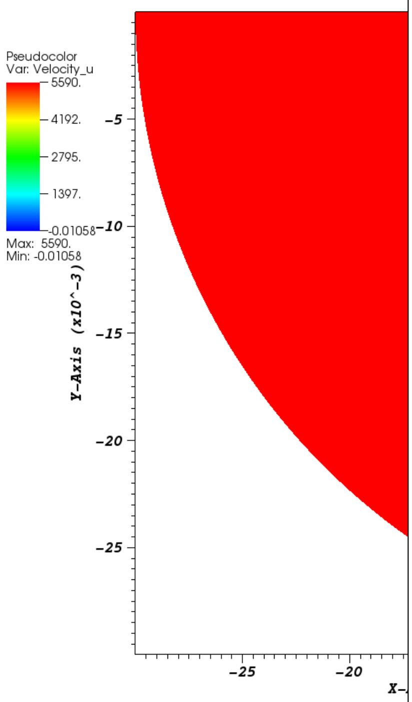

$t = 60\,\mu$secs.

Flat Plate Comparison

To test the implementation of the viscous fluxes a comparison between the mapped AMROC solver and the SU2 solver was completed.
A hyperbolic tangent mapping to stretch the grid away from the wall, with an initial spacing of 1e-5 m.
A Mach 3 flow over a 0.3 m flat plate was simulated using both an isothermal and adiabatic wall using the same mesh in each solver.

Flat Plate Comparison

A comparison between the two boundary layers at $0.2\,\mathrm{m}$ is shown below,

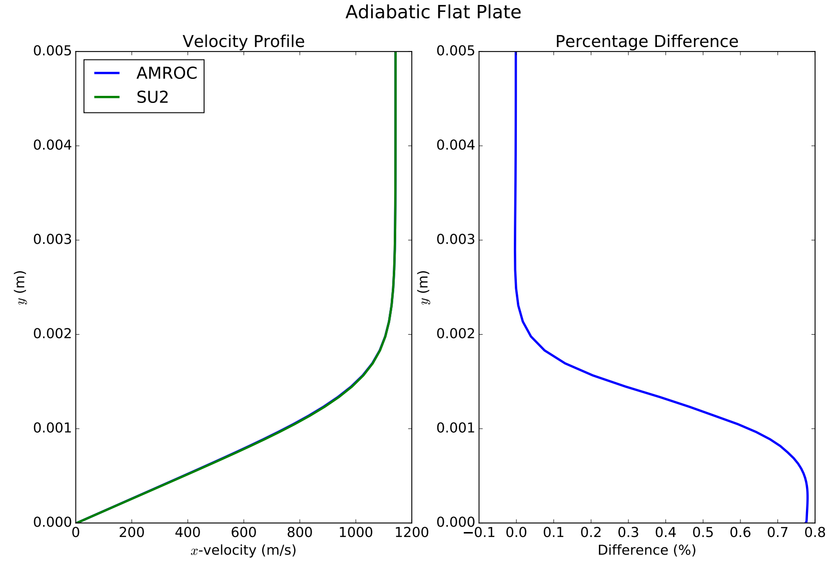

Figure: A comparison of the velocity boundary layers over an adiabatic flat plate, where $M_\infty = 3.0$.

Cylinder Heat Flux Computation

The mapped mesh solver has been validated by simulating a cylinder in a nonequilibrium, high enthalpy flow.
The inflow conditions and results were taken from [Degrez et al., 2009].

T_∞	ρ_∞	U_∞	Y_{N_2}	Y_N	Y_{O_2}	Y_O	Y_{NO}
694 K	3.26 $\mathrm{g/m^3}$	4776 $\mathrm{m/s}$	0.7356	0.0	0.1340	0.07955	0.0509

Table: Freestream conditions for the HEG cylinder simulation.

A cylinder mesh was generated with hyperbolic tangent stretching away from the wall using a 1e-6 initial spacing.

Cylinder Heat Flux Comparison

The simulated results show good agreement with the experimental results:

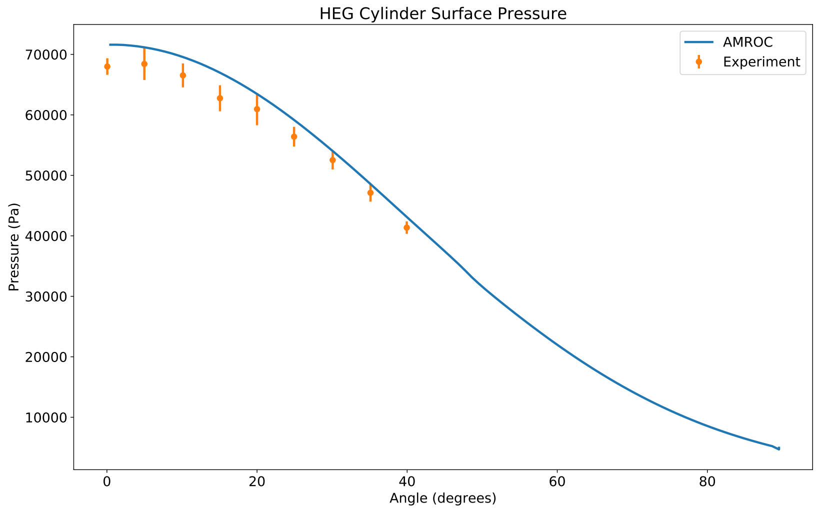

Figure: A comparison of the experimental and simulated surface pressures in the HEG cylinder experiment.

Hybrid method

Convective numerical flux is defined as

$$\mathbf{F}^n_{inv} = \begin{cases} \mathbf{F}^n_{inv-WENO}, & \text{in } \mathcal{C} \\ \mathbf{F}^n_{inv-CD}, & \text{in } \overline{\mathcal{C}}, \end{cases}$$

- For LES: 3rd order WENO method, 2nd order TCD [Hill and Pullin, 2004]
- For DNS: Symmetric 6th order WENO, 6th-order CD scheme

  J. Ziegler, RD, J. Shepherd, D. Pullin, *J. Comput. Phys.* 230(20):7598-7630, 2011.

Use WENO scheme to only capture shock waves but resolve interface between species.

Shock detection based on using two criteria together:

1. Lax-Liu entropy condition $|u_R \pm a_R| < |u_* \pm a_*| < |u_L \pm a_L|$ tested with a threshold to eliminate weak acoustic waves. Used intermediate states at cell interfaces:

$$u_* = \frac{\sqrt{\rho_L u_L} + \sqrt{\rho_R u_R}}{\sqrt{\rho_L} + \sqrt{\rho_R}}, \quad a_* = \sqrt{(\gamma_* - 1)(h_* - \frac{1}{2}u_*^2)}, \; \ldots$$

2. Limiter-inspired discontinuity test based on mapped normalized pressure gradient θ_j

$$\phi(\theta_j) = \frac{2\theta_j}{(1+\theta_j)^2} \quad \text{with} \quad \theta_j = \frac{|p_{j+1} - p_j|}{|p_{j+1} + p_j|}, \quad \phi(\theta_j) > \alpha_{Map}$$

Results for shear layer in Mach reflection pattern

WENO/CD - 6 levels

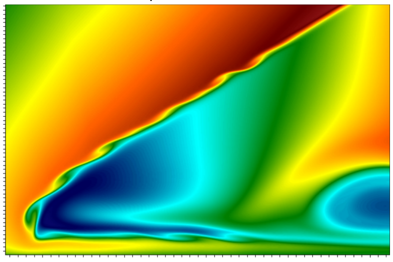

$\Delta x_{\min} = 3.91 \cdot 10^{-6}\,\mathrm{m}$

WENO/CD - 7 levels

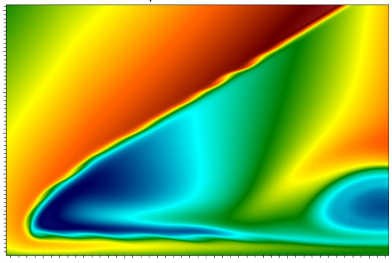

$\Delta x_{\min} = 1.95 \cdot 10^{-6}\,\mathrm{m}$

WENO/CD - 8 levels

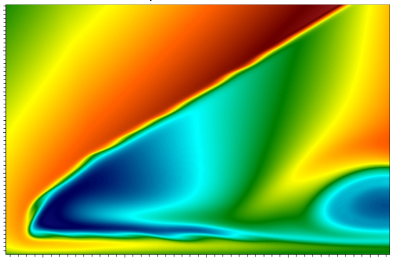

$\Delta x_{\min} = 9.77 \cdot 10^{-7}\,\mathrm{m}$

MUSCL - 7 levels

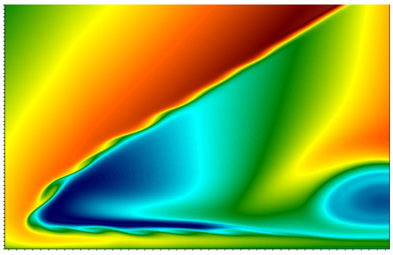

$\Delta x_{\min} = 1.05 \cdot 10^{-6}\,\mathrm{m}$

MUSCL - 7 levels - Euler

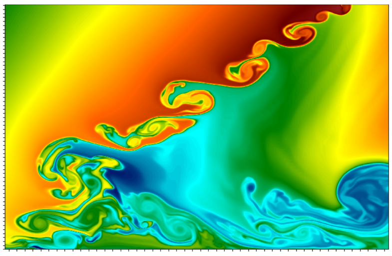

$\Delta x_{\min} = 1.05 \cdot 10^{-6}\,\mathrm{m}$

Usage of WENO for WENO/CD - 8 levels

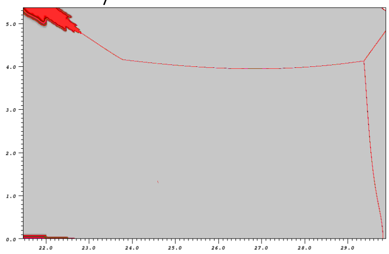

- WENO/CD/RK3 gives results comparable to 4x finer resolved optimal 2nd-order scheme, but CPU times with SAMR 2-3x larger
- Gain in CPU time from higher-order scheme roughly one order

Detonation ignition by hot jet in 2d

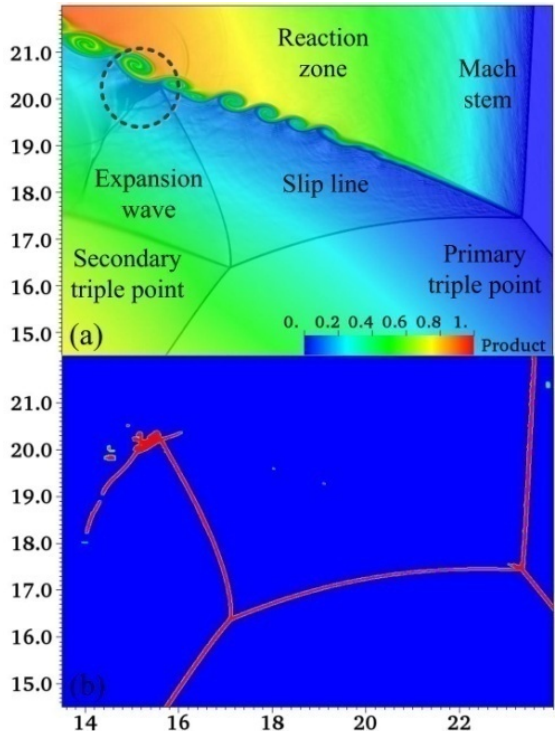

(a) Detailed structure, (b) WENO usage

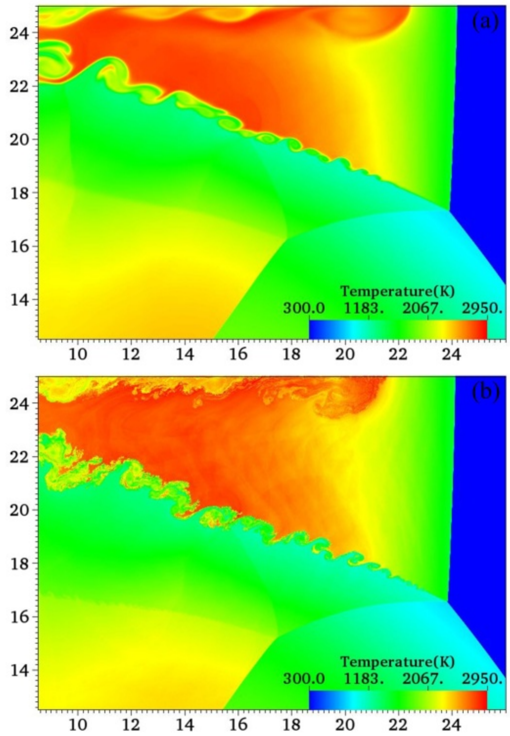

(a) Navier-Stokes, (b) Euler

X. Cai, RD, J. Liang, Y. Mahmoudi, *Proc. Combust. Institute* 36(2): 2725–2733, 2017

Conclusions – Hypersonics

- We have developed a first 2D prototype of two-temperature model solver that is suitable for very high temperatures, i.e., high enthalpy re-entry flows
- The Cartesian version is fully integrated into SAMR AMROC-Clawpack; structured non-Cartesian version runs also within AMROC-Clawpack but only on non-adaptive meshes so far
- SAMR framework can remain basically unchanged; however mapping needs to be considered in prolongation and restriction, flux correction, visualization (work in progress)
- For moving geometries, the goal is a Chimera-type approach that constructs non-Cartesian boundary layer meshes near the body and uses SAMR in the far field
- Incorporation of the methodology into the hybrid WENO/CD scheme for high enthalpy DNS in 3D is proposed within the next two years

References I

[Degrez et al., 2009] Degrez, G., Lani, A., Panesi, M., Chazot, O., and Deconinck, H. (2009). Modelling of High Enthalpy, High Mach Number Flows. *Journal of Physics D: Applied Physics*, 42.

[Hill and Pullin, 2004] Hill, D. J. and Pullin, D. I. (2004). Hybrid tuned center difference - WENO method for large eddy simulations in the presence of strong shocks. *J. Comput. Phys.*, 194(2):435–450.

[Hornung, 1972] Hornung, H. G. (1972). Non-equilibrium dissociating nitrogen flow over spheres and circular cylinders. *Journal of Fluid Mechanics*, 53:149–176.

[Liou and Steffen Jr, 1993] Liou, M.-S. and Steffen Jr, C. J. (1993). A new flux splitting scheme. *Journal of Computational Physics*, 107:23–39.

[Lobb, 1964] Lobb, K. R. (1964). Experimental Measurement of Shock Detachment Distance on Spheres Fired in Air at Hypervelocities. *High Temperature Aspects of Hypersonic Flows*, 14(5):519–527.

[Moukalled et al., 2015] Moukalled, F., Mangani, L., and Darwish, M. (2015). *The finite volume method in computational fluid dynamics: An Advanced Introduction with OpenFOAM and Matlab*. Springer.

[Pezzella et al., 2015] Pezzella, G., de Rosa, D., and Donelli, R. (2015). Computational Analysis of Shock Wave Boundary Layer Interactions in Non-equilibrium Hypersonic Flow. *20th AIAA International Space Planes and Hypersonic Systems and Technologies Conference*, (July):1–12.

[Scoggins and Magin, 2014] Scoggins, J. B. and Magin, T. E. (2014). Development of Mutation++ : MUlticomponent Thermodynamics And Transport properties for IONized gases library in C++. In *11th AIAA/ASME Joint Thermophysics and Heat Transfer Conference*.

[Sutton and Gnoffo, 1998] Sutton, K. and Gnoffo, P. A. (1998). Multi-Component Diffusion with Application To Computational Aerothermodynamics. *7th AIAA / ASME Joint Thermophysics and Heat Transfer Conference*.

[van Leer, 1982] van Leer, B. (1982). Flux Vector Splitting for the Euler Equations. In *Eighth international conference on numerical methods in fluid dynamics*.

Aerodynamics and fluid-structure interaction simulation with AMROC Part I

Ralf Deiterding

Aerodynamics and Flight Mechanics Research Group
University of Southampton
Highfield Campus
Southampton SO17 1BJ, UK
Email: r.deiterding@soton.ac.uk

Xiamen
24th July, 2019

Outline

Fluid-structure coupling
- Approach
- Rigid body motion
- Thin elastic and deforming thin structures
- Real-world example

Train-tunnel aerodynamics
- Validation
- Passing trains in open space
- Passing trains in a double track tunnel

Summary
- Conclusions

Collaboration with

Finite volume methods

- Jose M. Garro Fernandez (University of Southampton)
- Stuart Laurence (Department of Aerospace Engineering, University of Maryland, College Park)
- Fehmi Cirak (Cambridge University)
- Sean Mauch, Joe Shepherd, Dan Meiron (California Institute of Technology)

Lattice Boltzmann methods

- Christos Gkoudesnes, Juan Antonio Reyes Barraza (University of Southampton)
- Stephen Wood (NASA)
- Kai Feldhusen, Claus Wagner (German Aerospace Center – DLR)
- Moritz Fragner (University of Applied Sciences Hannover, Germany)
- Cinar Laloglu (Marmara University, Turkey)

Construction of coupling data

- Moving boundary/interface is treated as a moving contact discontinuity and represented by level set [Fedkiw, 2002][Arienti et al., 2003]
- Efficient construction of level set from triangulated surface data with closest-point-transform (CPT) algorithm [Mauch, 2003]
- One-sided construction of mirrored ghost cell and new FEM nodal point values
- FEM ansatz-function interpolation to obtain intermediate surface values
- Explicit coupling possible if geometry and velocities are prescribed for the more compressible medium [Specht, 2000]

$u_n^F := u_n^S(t)|_{\mathcal{I}}$
UpdateFluid(Δt)
$\sigma_{nm}^S := -p^F(t+\Delta t)\delta_{nm}|_{\mathcal{I}}$
UpdateSolid(Δt)
$t := t + \Delta t$

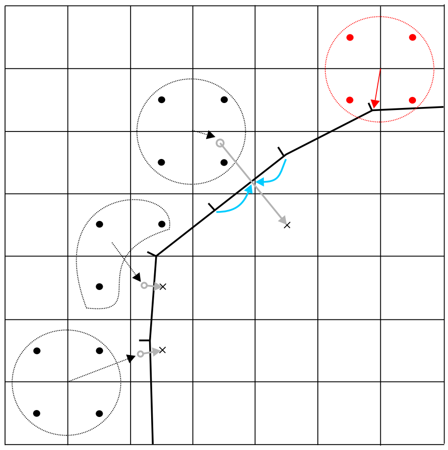

Coupling conditions on interface
Inviscid fluid:

$u_n^S = u_n^F$

Closest point transform algorithm

The signed distance φ to a surface $\mathcal{I}$ satisfies the eikonal equation [Sethian, 1999]

$$|\nabla\varphi| = 1 \quad \text{with} \quad \varphi\big|_{\mathcal{I}} = 0$$

Solution smooth but non-diferentiable across characteristics.

Distance computation trivial for non-overlapping elementary shapes but difficult to do efficiently for triangulated surface meshes:

- Geometric solution approach with plosest-point-transform algorithm [Mauch, 2003]

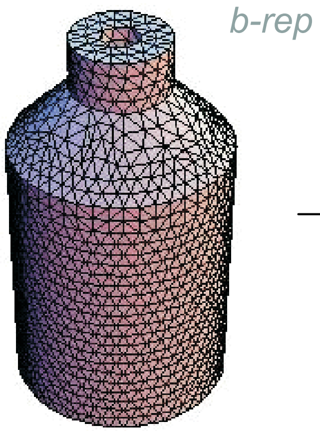

Surface mesh $\mathcal{I}$

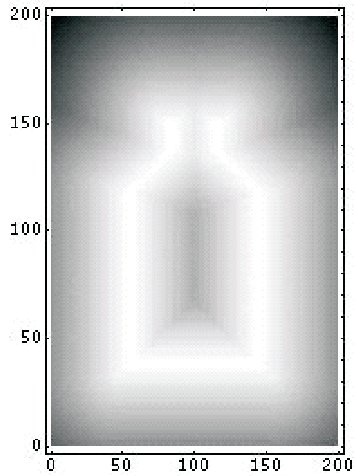

Distance φ

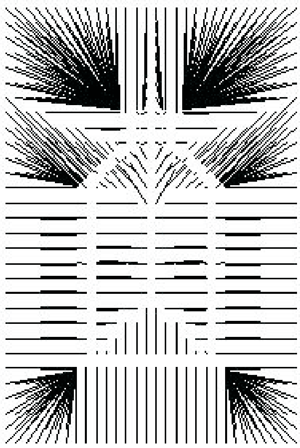

Normal to closest point

The characteristic / scan conversion algorithm

1. Build the characteristic polyhedrons for the surface mesh
2. For each face/edge/vertex
   2.1 Scan convert the polyhedron.
   2.2 Compute distance to that primitive for the scan converted points
3. Computational complexity.
   - $O(m)$ to build the b-rep and the polyhedra.
   - $O(n)$ to scan convert the polyhedra and compute the distance, etc.
4. Problem reduction by evaluation only within specified max. distance

[Mauch, 2003], see also [Deiterding et al., 2006]

Characteristic polyhedra for faces, edges, and vertices

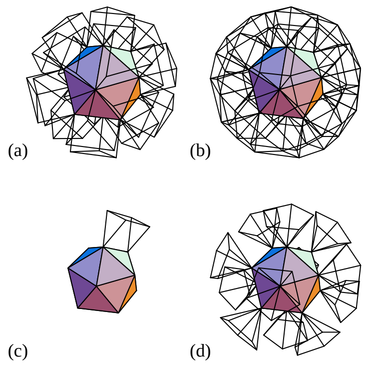

Slicing and scan conversion of apolygon

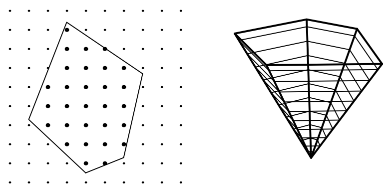

Eulerian/Lagrangian communication module

1. Put bounding boxes around each solid processors piece of the boundary and around each fluid processors grid
2. Gather, exchange and broadcast of bounding box information
3. Optimal point-to-point communication pattern, non-blocking

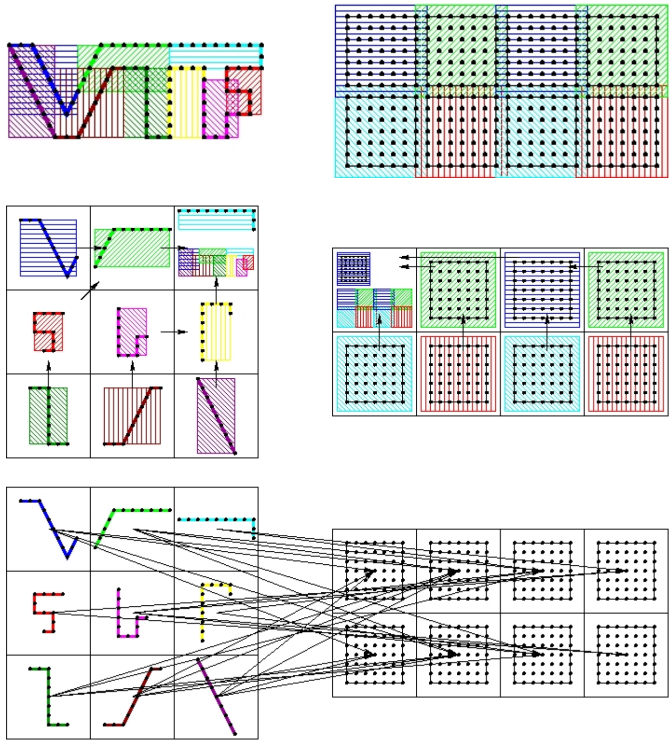

Coupling elements

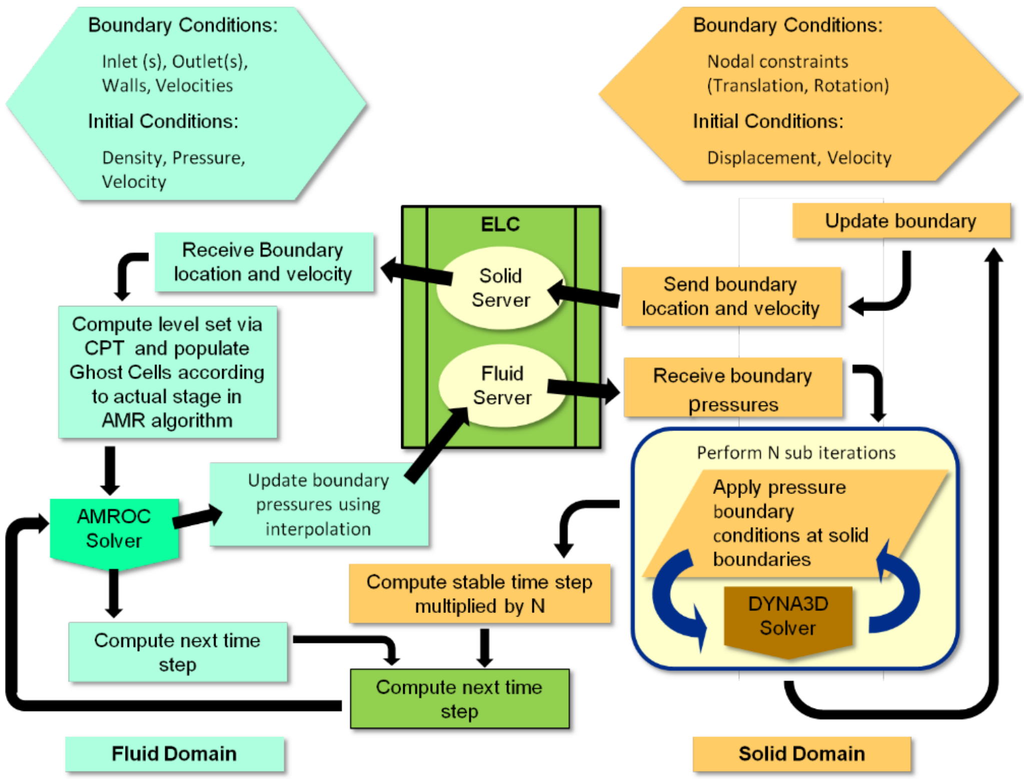

Proximal bodies in hypersonic flow

Flow modeled by Euler equations for a single polytropic gas with $p = (\gamma - 1)\,\rho e$

$$\partial_t \rho + \partial_{x_n}(\rho u_n) = 0\ , \quad \partial_t(\rho u_k) + \partial_{x_n}(\rho u_k u_n + \delta_{kn} p) = 0\ , \quad \partial_t(\rho E) + \partial_{x_n}(u_n(\rho E + p)) = 0$$

Numerical approximation with

- Finite volume flux-vector splitting scheme with MUSCL reconstruction, dimensional splitting
- Spherical bodies, force computation with overlaid lattitude-longitude mesh to obtain drag and lift coefficients $C_{D,L} = \dfrac{2F_{D,L}}{\rho v^2 \pi r^2}$
- inflow $M = 10$, C_D and C_L on secondary sphere, lateral position varied, no motion

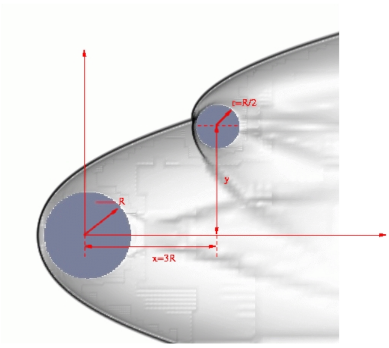

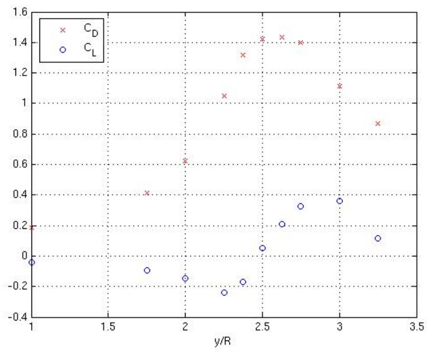

Verification and validation

Static force measurements, $M = 10$:
[Laurence et al., 2007]

- Refinement study: $40 \times 40 \times 32$ base grid , up to without AMR up to $\sim 209.7 \cdot 10^6$ cells, largest run $\sim 35,000\,\mathrm{h}$ CPU

$l_{\max}$	C_D	ΔC_D	C_L	ΔC_L
1	1.264		-0.176	
2	1.442	0.178	-0.019	0.157
3	1.423	-0.019	0.052	0.071
4	1.408	-0.015	0.087	0.035

- Comparison with experimental results: 3 additional levels, $\sim 2000\,\mathrm{h}$ CPU

	Experimental	Computational
C_D	1.11 ± 0.08	1.01
C_L	0.29 ± 0.05	0.28

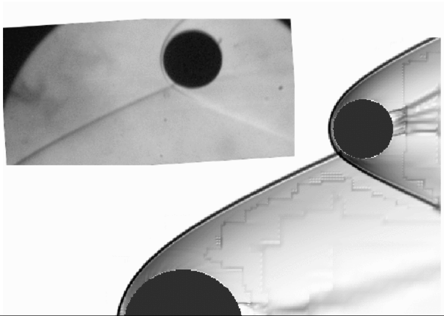

Dynamic motion, $M = 4$:

- Base grid $150 \times 125 \times 90$, two additional levels with $r_{1,2} = 2$
- 24,704 time steps, $36,808\,\mathrm{h}$ CPU on 256 cores IBM BG/P

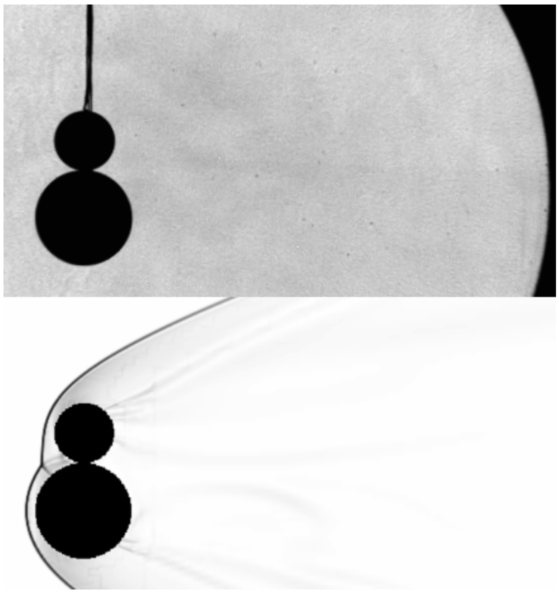

[Laurence and Deiterding, 2011]

Schlieren graphics on refinement regions

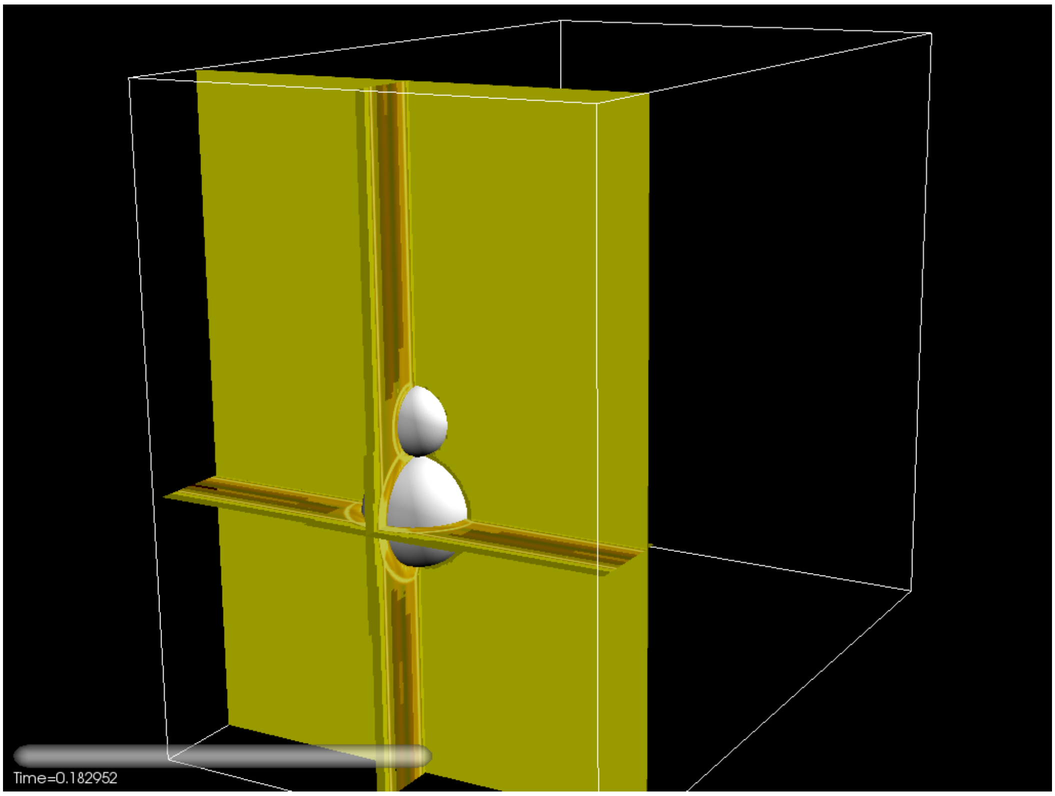

Treatment of thin structures

- Thin boundary structures or lower-dimensional shells require "thickening" to apply embedded boundary method
- Unsigned distance level set function φ
- Treat cells with $0 < \varphi < d$ as ghost fluid cells

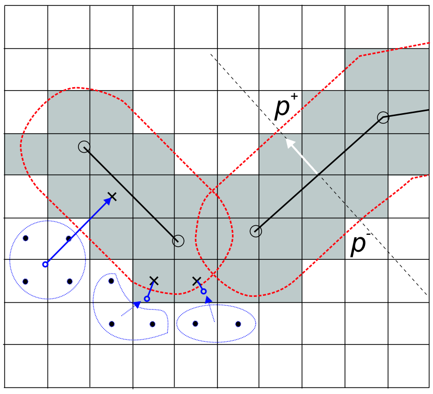

- Leaving φ unmodified ensures correctness of $\nabla\varphi$
- Use face normal in shell element to evaluate in $\Delta p = p^+ - p^-$
- Utilize finite difference solver using the beam equation

$$\rho_s h \frac{\partial^2 w}{\partial t^2} + EI \frac{\partial^4 w}{\partial \bar{x}^4} = p^F$$

to verify FSI algorithms

FSI verification by elastic vibration

- Thin steel plate (thickness $h = 1\,\mathrm{mm}$, length $50\,\mathrm{mm}$), clamped at lower end
- $\rho_s = 7600\,\mathrm{kg/m^3}$, $E = 220\,\mathrm{GPa}$, $I = h^3/12$, $\nu = 0.3$
- Modeled with beam solver (101 points) and thin-shell FEM solver (325 triangles) by F. Cirak
- Left: Coupling verification with constant instantenous loading by $\Delta p = 100\,\mathrm{kPa}$
- Right: FSI verification with Mach 1.21 shockwave in air ($\gamma = 1.4$)

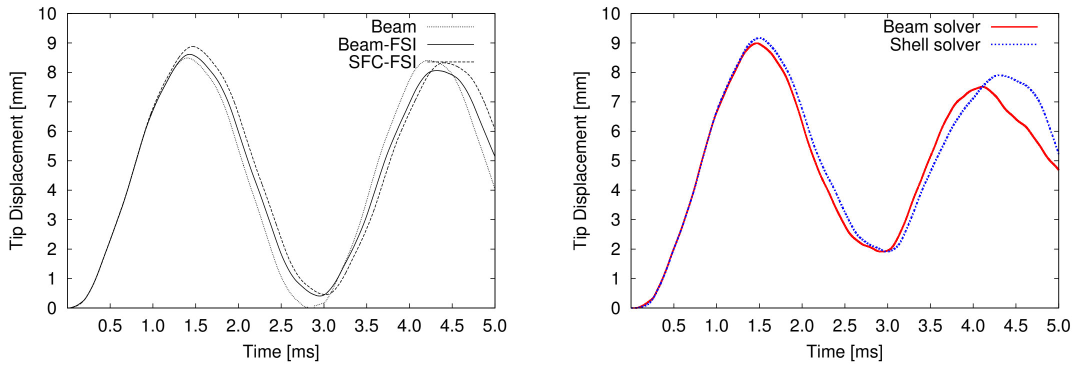

Shock-driven elastic panel motion

Test case suggested by [Giordano et al., 2005]

- Forward facing step geometry, fixed walls everywhere except at inflow

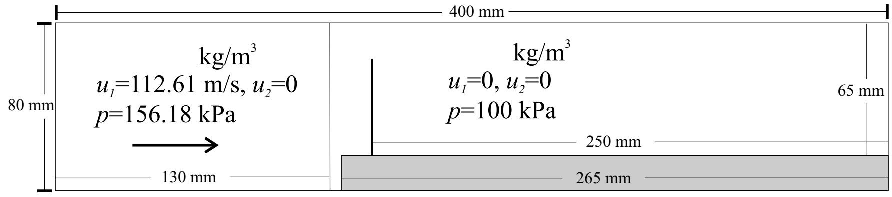

- SAMR base mesh $320 \times 64(\times 2)$, $r_{1,2} = 2$
- Intel 3.4GHz Xeon dual processors, GB Ethernet interconnect
  - Beam-FSI: $12.25\,\mathrm{h}$ CPU on 3 fluid CPU + 1 solid CPU
  - FEM-FSI: $322\,\mathrm{h}$ CPU on 14 fluid CPU + 2 solid CPU

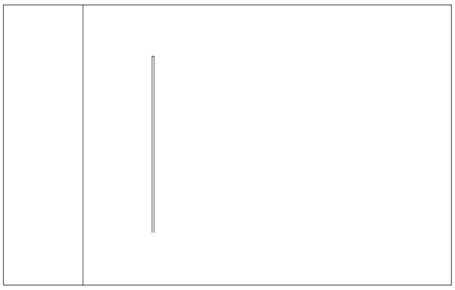

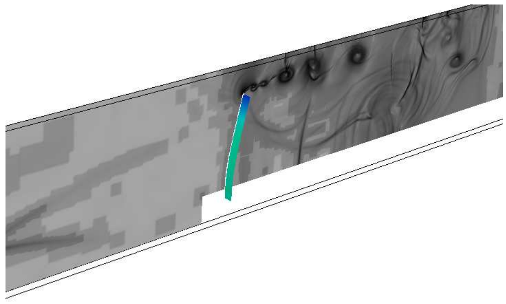

$t = 1.56\,\mathrm{ms}$ after impact

Detonation-driven plastic deformation

Chapman-Jouguet detonation in a tube filled with a stoichiometric ethylene and oxygen ($\mathrm{C_2H_4} + 3\,\mathrm{O_2}$, $295\,\mathrm{K}$) mixture. Euler equations with single exothermic reaction $A \longrightarrow B$

$$\partial_t \rho + \partial_{x_n}(\rho u_n) = 0 \;, \quad \partial_t(\rho u_k) + \partial_{x_n}(\rho u_k u_n + \delta_{kn} p) = 0 \;, k = 1, \dots, d$$
$$\partial_t(\rho E) + \partial_{x_n}(u_n(\rho E + p)) = 0 \;, \quad \partial_t(Y\rho) + \partial_{x_n}(Y\rho u_n) = \psi$$

with

$$p = (\gamma - 1)(\rho E - \frac{1}{2}\rho u_n u_n - \rho Y q_0) \quad \text{and} \quad \psi = -kY\rho \exp\left(\frac{-E_{\mathrm{A}}\rho}{p}\right)$$

modeled with heuristic detonation model by [Mader, 1979]

$V := \rho^{-1}$, $V_0 := \rho_0^{-1}$, $V_{\mathrm{CJ}} := \rho_{\mathrm{CJ}}$
$Y' := 1 - (V - V_0)/(V_{\mathrm{CJ}} - V_0)$
`If` $0 \le Y' \le 1$ `and` $Y > 10^{-8}$ `then`
  `If` $Y < Y'$ `and` $Y' < 0.9$ `then` $Y' := 0$
  `If` $Y' < 0.99$ `then` $p' := (1 - Y')p_{\mathrm{CJ}}$
    `else` $p' := p$
  $\rho_{\mathrm{A}} := Y'\rho$
  $E := p'/(\rho(\gamma - 1)) + Y' q_0 + \frac{1}{2} u_n u_n$

Comparison of the pressure traces in the experiment and in a 1d simulation

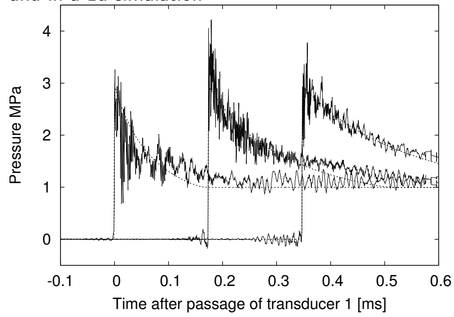

Tube with flaps

- Fluid: VanLeer FVS
  - Detonation model with $\gamma = 1.24$, $p_{\mathrm{CJ}} = 3.3\,\mathrm{MPa}$, $D_{\mathrm{CJ}} = 2376\,\mathrm{m/s}$
  - AMR base level: $104 \times 80 \times 242$, $r_{1,2} = 2$, $r_3 = 4$
  - $\sim 4 \cdot 10^7$ cells instead of $7.9 \cdot 10^9$ cells (uniform)
  - Tube and detonation fully refined
  - Thickening of 2D mesh: $0.81\,\mathrm{mm}$ on both sides (real $0.445\,\mathrm{mm}$)
- Solid: thin-shell solver by F. Cirak
  - Aluminum, J2 plasticity with hardening, rate sensitivity, and thermal softening
  - Mesh: 8577 nodes, 17056 elements
- 16+2 nodes 2.2 GHz AMD Opteron quad processor, PCI-X 4x Infiniband network, $\sim 4320\,\mathrm{h}$ CPU to $t_{end} = 450\,\mu\mathrm{s}$


$0.032\,\mathrm{ms}$

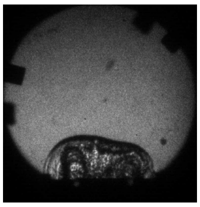
$0.030\,\mathrm{ms}$

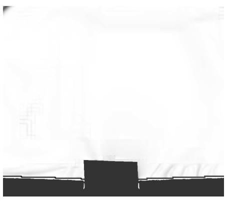
$0.212\,\mathrm{ms}$

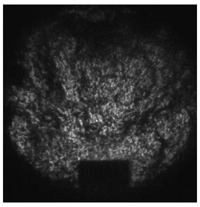
$0.210\,\mathrm{ms}$

Tube with flaps: results

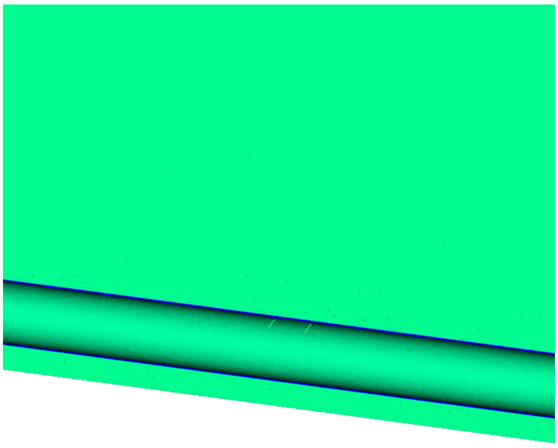

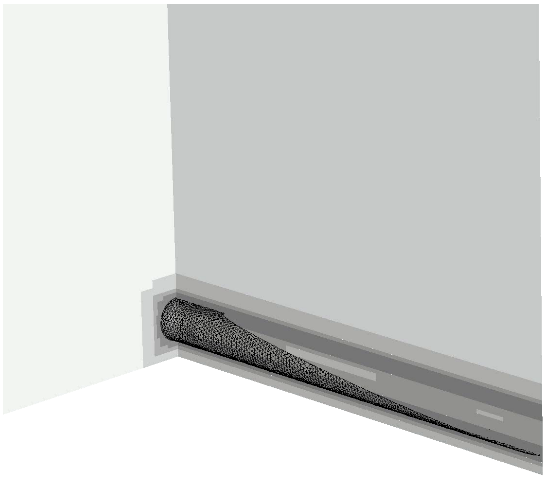

Fluid density and diplacement in y-direction in solid

Schlieren plot of fluid density on refinement levels

[Cirak et al., 2007]

Coupled fracture simulation

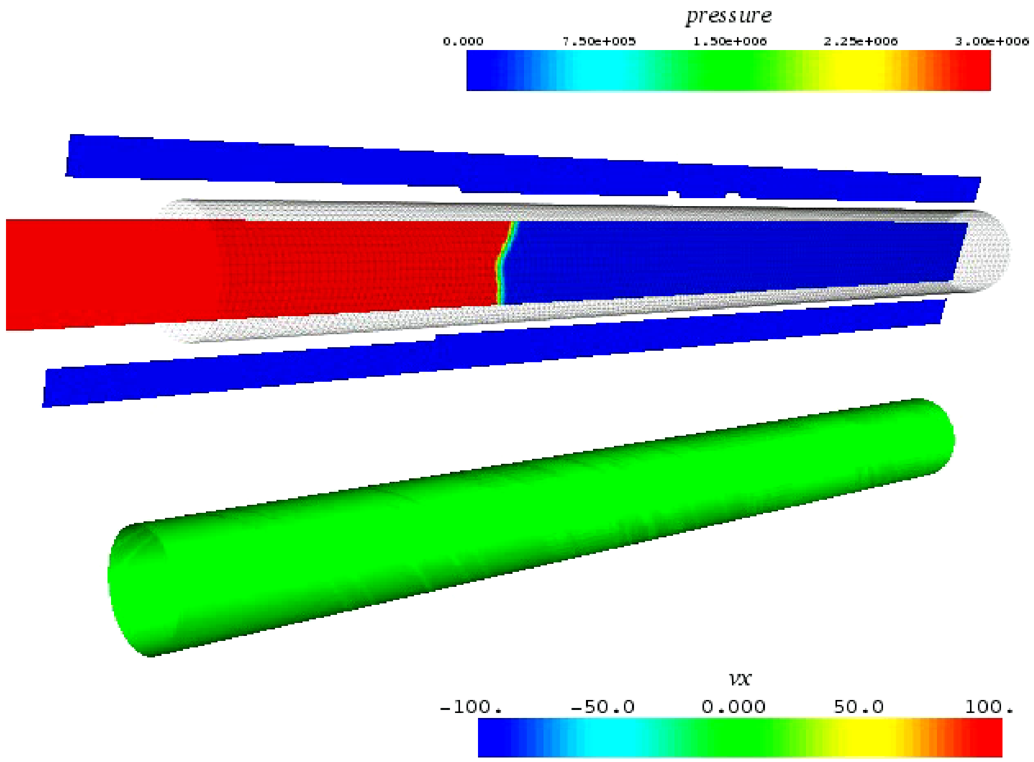

Blast explosion in a multistory building

- $20\,\mathrm{m} \times 40\,\mathrm{m} \times 25\,\mathrm{m}$ seven-story building similar to [Luccioni et al., 2004]
- Spherical energy deposition $\equiv 400\,\mathrm{kg}$ TNT, $r = 0.5\,\mathrm{m}$ in lobby of building
- SAMR: $80 \times 120 \times 90$ base level, three additional levels $r_{1,2} = 2$, $l_{\rm fsi} = 1$, $k = 1$
- Simulation with ground: 1,070 coupled time steps, $830\,\mathrm{h}$ CPU ($\sim 25.9\,\mathrm{h}$ wall time) on 31+1 cores
- $\sim 8,000,000$ cells instead of 55,296,000 (uniform)
- 69,709 hexahedral elements and with material parameters. [Deiterding and Wood, 2013]

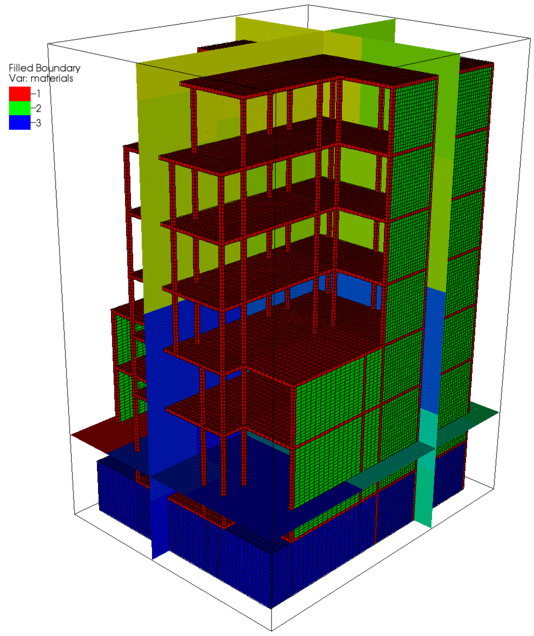

	ρ_s [kg/m^3]	σ_0 [MPa]	E_T [GPa]	β	K [GPa]	G [GPa]	$\bar{\epsilon}^p$	p_f [MPa]
Columns	2010	50	11.2	1.0	21.72	4.67	0.02	-30
Walls	2010	25	11.2	1.0	6.22	4.67	0.01	-15

Blast explosion in a multistory building – II

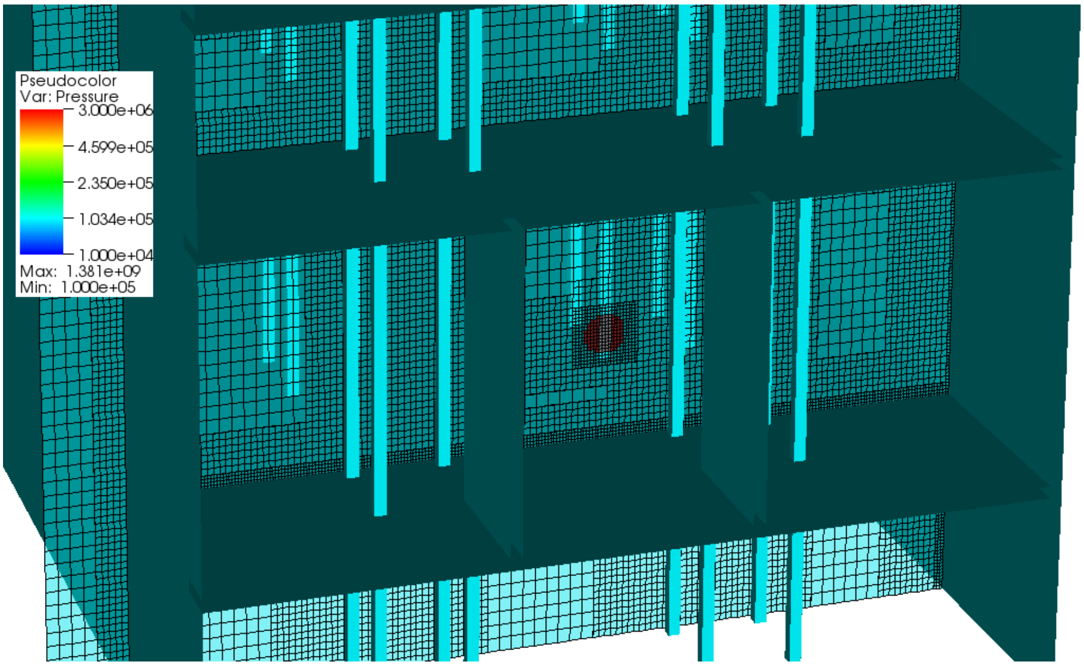

$t = 0$

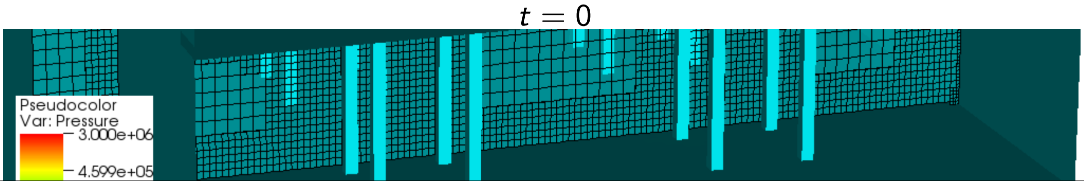

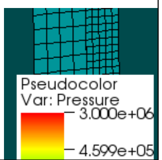

Laboratory tunnel simulator [Zonglin et al., 2002]

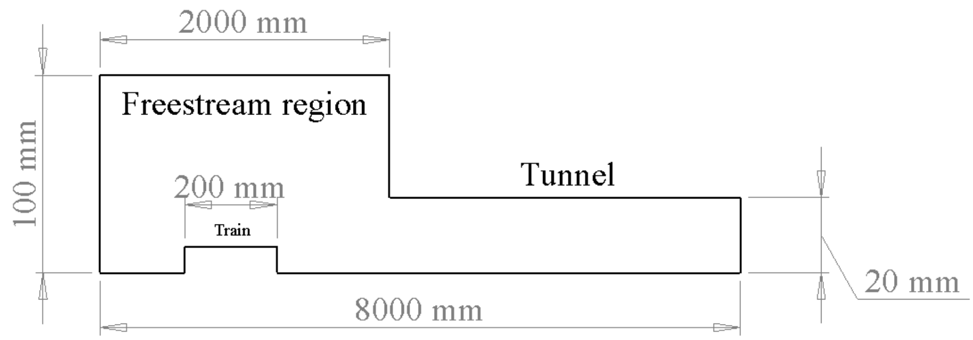

Model solves the inviscid Euler equations

$$\partial_t \rho + \nabla \cdot (\rho \mathbf{u}) = 0$$
$$\partial_t (\rho \mathbf{u}) + \nabla \cdot (\rho \mathbf{u} \otimes \mathbf{u}) + \nabla p = 0$$
$$\partial_t (\rho E) + \nabla \cdot ((\rho E + p)\mathbf{u}) = 0$$

with $p = (\gamma - 1)(\rho E - \frac{1}{2}\rho \mathbf{u}^T \mathbf{u})$

- Two-dimensional axi-symmetric computation
- $p_0 = 100\,\mathrm{kPa}$, $\rho_0 = 1.225\,\mathrm{kg/m^3}$, $\gamma = 1.4$
- Roe shock-capturing scheme blended with HLL
- 2nd order accuracy achieved with MUSCL-Hancock method

Basic phenomena – $v_0 = 100\,\mathrm{m/s}$

- 800×25 mesh with Cartesian cut-out $(200, 5)$ to $(800, 25)$
- 2 level of additional refinement by factor 2

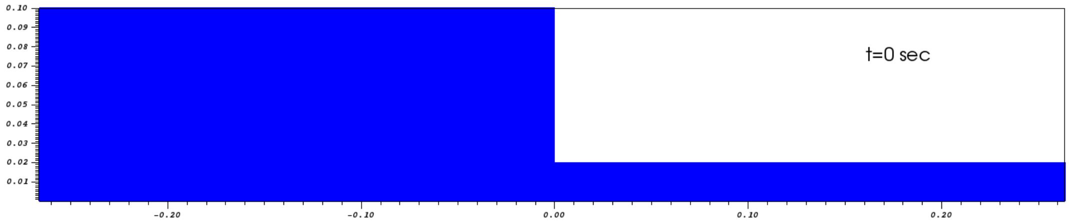

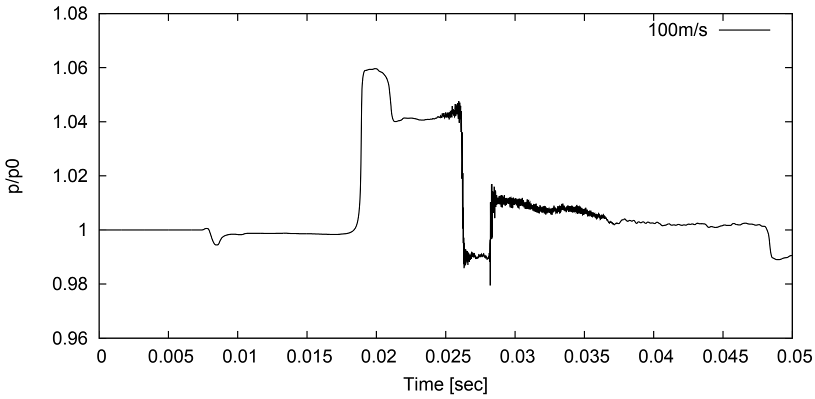

Pressure record at location $(1020\,\mathrm{mm}, 20\,\mathrm{mm})$ inside tunnel

Comparison with experiment – I

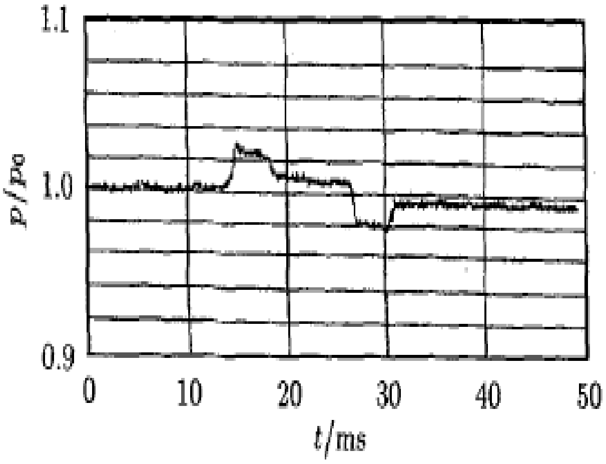

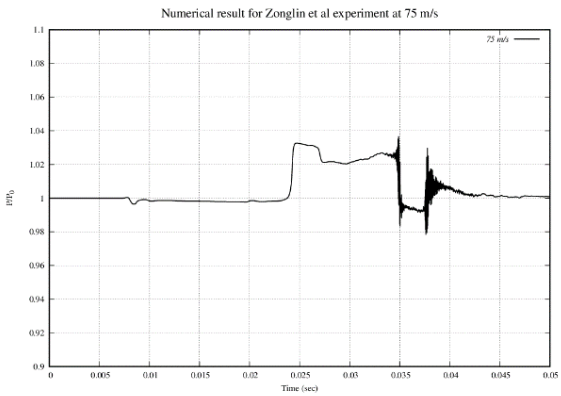

Pressure record at $(1020\,\mathrm{mm}, 20\,\mathrm{mm})$ for $v_0 = 75\,\mathrm{m/s}$. Experiment (left) and AMROC (right)

Comparison with experiment – I

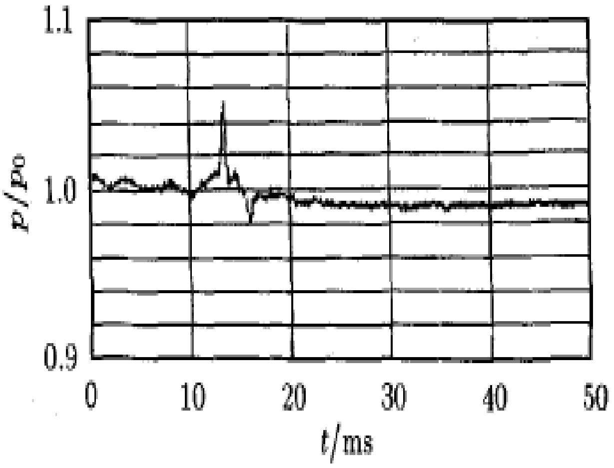

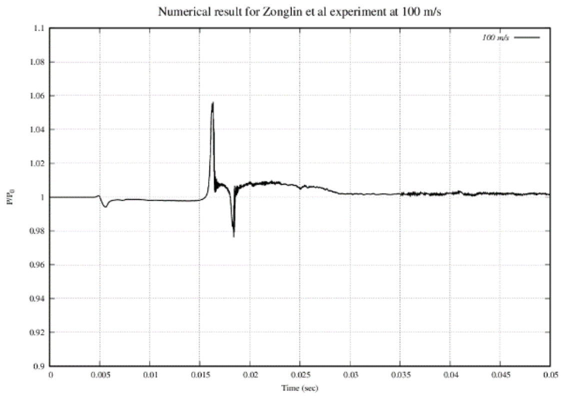

Pressure record at $(40\,\mathrm{mm}, 20\,\mathrm{mm})$ for model velocity $v_0 = 100\,\mathrm{m/s}$. Experiment (left) and AMROC (right)

Variation of velocity and nose half angle

Pressure sensor at $(420\,\mathrm{mm}, 20\,\mathrm{mm})$

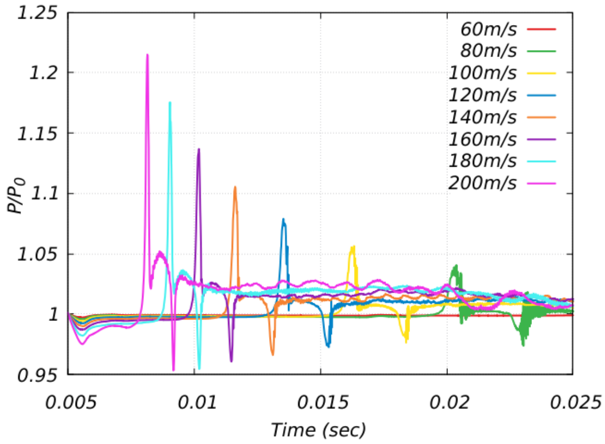

Pressure sensor at $(1020\,\mathrm{mm}, 20\,\mathrm{mm})$

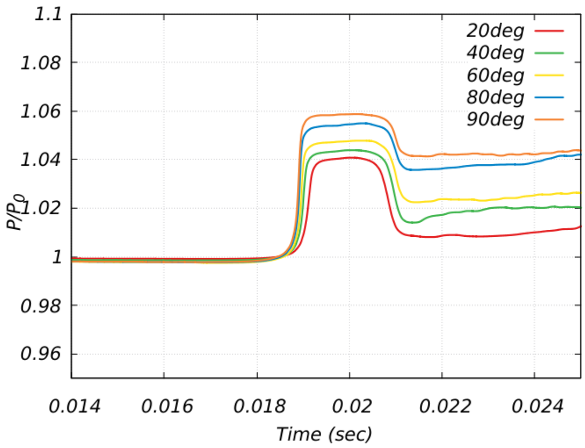

- Dependence on v_0^2 is the dynamic pressure influence (left)
- For constant blockage ratio and body velocity, using more pointed noses alleviates the maximal pressure level (right, nose half angle varied)
- For $v_0 \approx 140\,\mathrm{m/s}$ a shock wave (tunnel boom) can be observed. Sharper noses also delay this phenomenon.

NGT2 prototype setup

- Next Generation Train 2 (NGT2) geometry by the German Aerospace Centre (DLR) [Fragner and Deiterding, 2016, Fragner and Deiterding, 2017]
- Mirrored train head of length $\sim 60\,\mathrm{m}$, no wheels or tracks, train models $0.17\,\mathrm{m}$ above ground above the ground level.
- Train velocities $100\,\mathrm{m/s}$ and $-100\,\mathrm{m/s}$, middle axis $6\,\mathrm{m}$ apart, initial distance between centers $200\,\mathrm{m}$
- Base mesh of $360 \times 40 \times 30$ for domain of $360\,\mathrm{m} \times 40\,\mathrm{m} \times 30\,\mathrm{m}$
- Two/three additional levels, refined by $r_{1,2,3} = 2$. Refinement based on pressure gradient and level set and regenerated at every coarse time step. Parallel redistribution at every level-0 time step.
- On 96 cores Intel Xeon E5-2670 $2.6\,\mathrm{GHz}$ a final $t_e = 3\,\mathrm{sec}$ was reached after $12,385\,\mathrm{sec}$ / $43,395\,\mathrm{sec}$ wall time, i.e., $330\,\mathrm{h}$ and $1157\,\mathrm{h}$ CPU

Passing in open space – AMR and dynamic distribution

Domains of three-level refinement

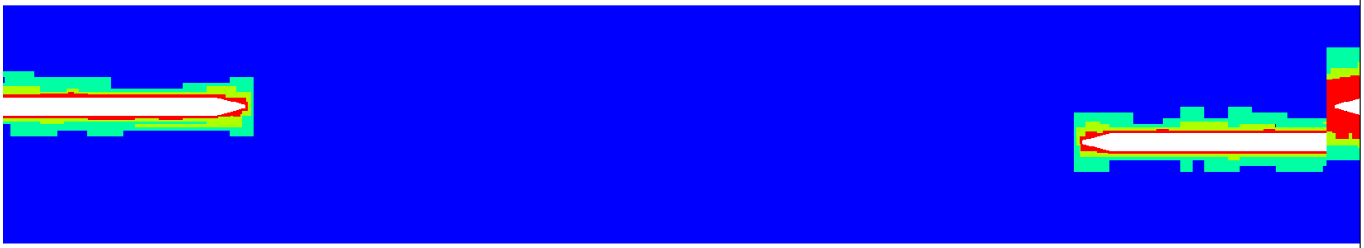

Distribution to 96 processors

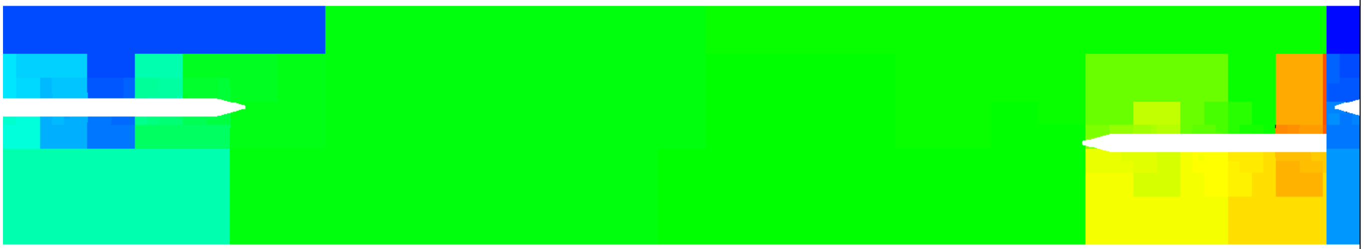

Enlargement of domain center shown

Pressure isosurfaces

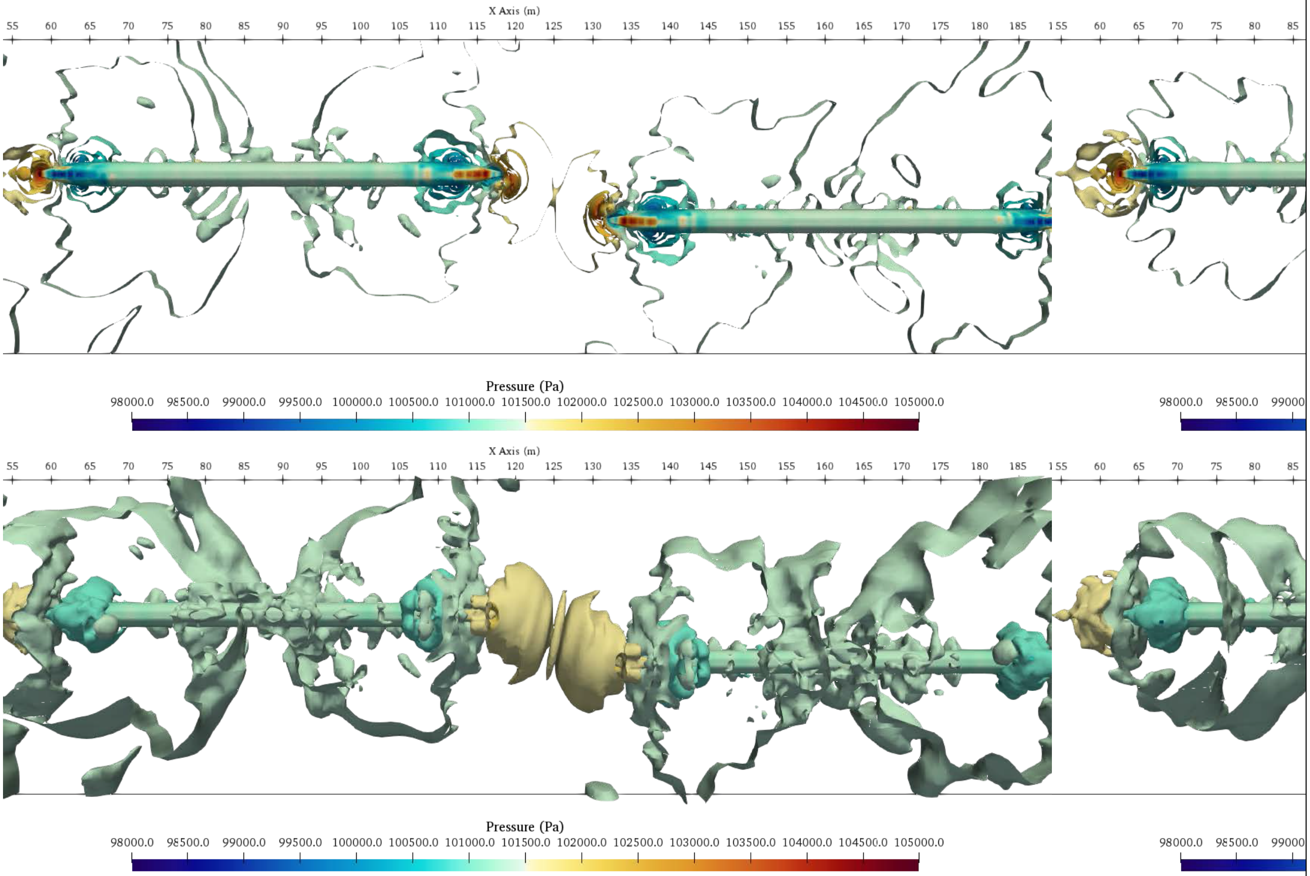

Pressure transects

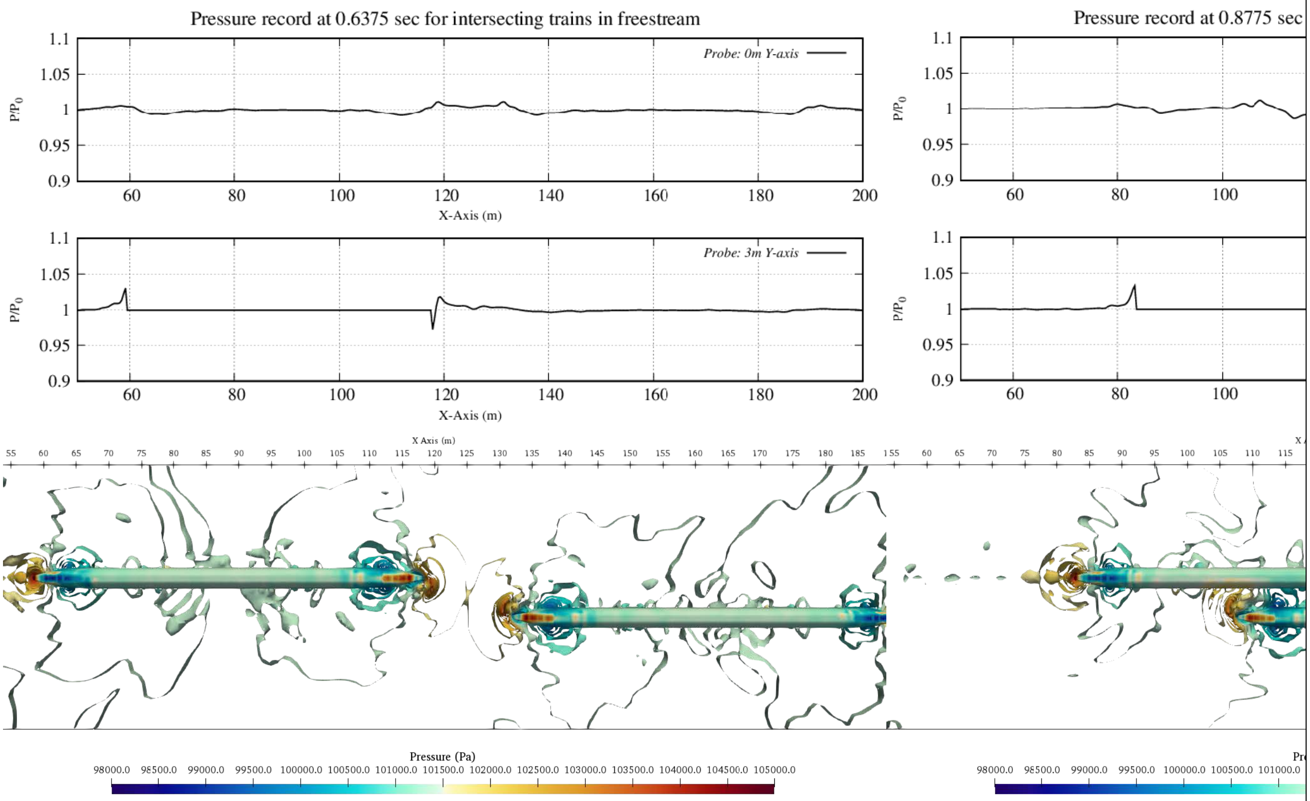

Setup with realistic tunnel shape

- Two NGT2 trains again at velocities $100\,\mathrm{m/s}$ and $-100\,\mathrm{m/s}$
- Prototype straight double track tunnel of $640\,\mathrm{m}$ length, initial distance between centers of trains $820\,\mathrm{m}$
- Base mesh of $1060 \times 36 \times 24$ for domain of $1060\,\mathrm{m} \times 36\,\mathrm{m} \times 24\,\mathrm{m}$, three levels refined by $r_{1,2,3} = 2$
- On 96 cores Intel Xeon E5-2670 $2.6\,\mathrm{GHz}$ a final $t_e = 5\,\mathrm{sec}$ was reached after $84,651\,\mathrm{sec}$ wall time, i.e., $2257\,\mathrm{h}$ CPU

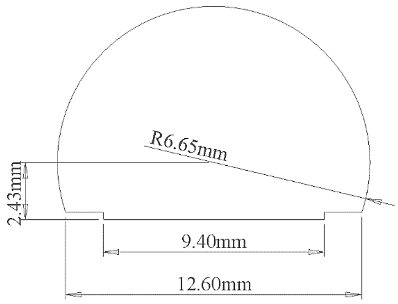

Tunnel shape

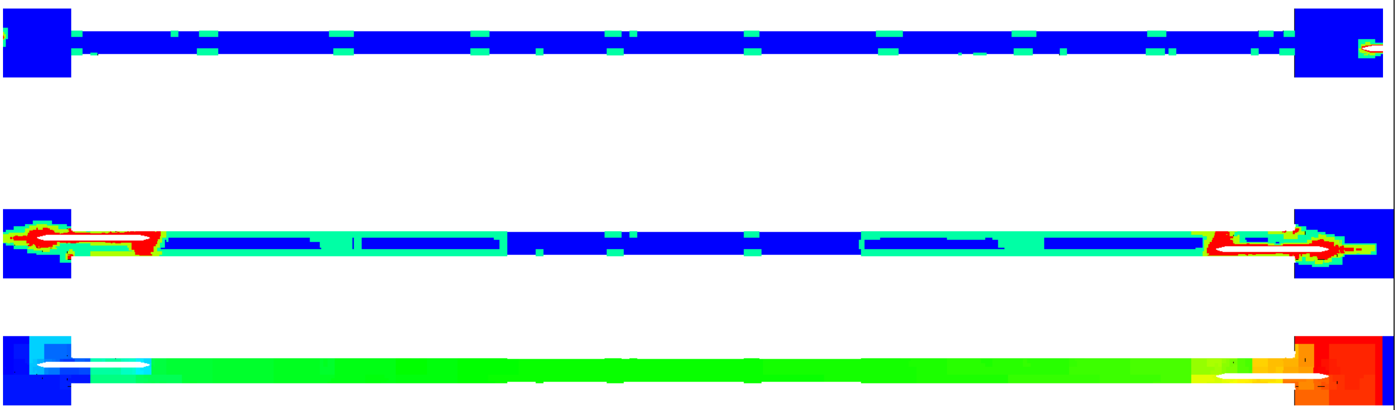

Pressure transects

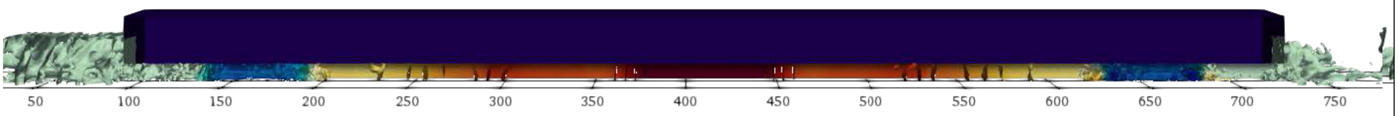

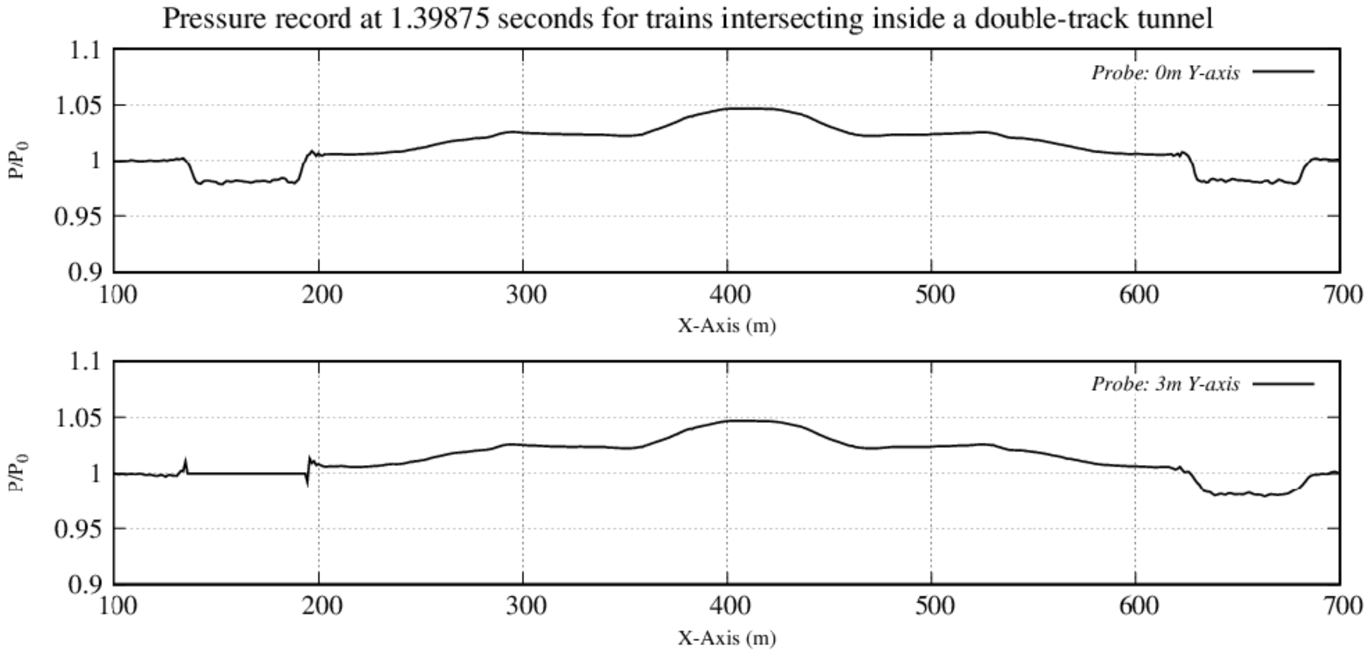

Conclusions – compressible flow aerodynamics

- A Cartesian embedded boundary method for compressible flows with block-based adaptive mesh refinement is an efficient and scalable prediction tool for pressure and shock waves created by moving bodies
- Multi-resolution and fluid-structure coupling problems can be tackled without expensive mesh regeneration
  - Level set approach easily handles large motions, element failure and removal
  - Dynamic adaptation ensures high resolution at embedded boundaries and essential flow features
- Aerodynamics of bodies with large motion are easily accessible
  - Current inviscid approach predicts maximal overpressure in front of trains reliably
  - For predicting the flow around entire trains, the boundary layer growing over the train body needs to be considered.
  - AMROC solvers for the compressible Navier-Stokes equations and even LES are already available, however, for this particular application a turbulent wall function on the embedded boundary first needs to be implemented. Such a wall function is currently work-in-progress for the LBM-LES solver.

References I

[Arienti et al., 2003] Arienti, M., Hung, P., Morano, E., and Shepherd, J. E. (2003). A level set approach to Eulerian-Lagrangian coupling. *J. Comput. Phys.*, 185:213–251.

[Cirak et al., 2007] Cirak, F., Deiterding, R., and Mauch, S. P. (2007). Large-scale fluid-structure interaction simulation of viscoplastic and fracturing thin shells subjected to shocks and detonations. *Computers & Structures*, 85(11-14):1049–1065.

[Deiterding et al., 2006] Deiterding, R., Radovitzky, R., Mauch, S. P., Noels, L., Cummings, J. C., and Meiron, D. I. (2006). A virtual test facility for the efficient simulation of solid materials under high energy shock-wave loading. *Engineering with Computers*, 22(3-4):325–347.

[Deiterding and Wood, 2013] Deiterding, R. and Wood, S. L. (2013). Parallel adaptive fluid-structure interaction simulations of explosions impacting on building structures. *Computers & Fluids*, 88:719–729.

[Fedkiw, 2002] Fedkiw, R. P. (2002). Coupling an Eulerian fluid calculation to a Lagrangian solid calculation with the ghost fluid method. *J. Comput. Phys.*, 175:200–224.

[Fragner and Deiterding, 2016] Fragner, M. M. and Deiterding, R. (2016). Investigating cross-wind stability of high speed trains with large-scale parallel cfd. *Int. J. Comput. Fluid Dynamics*, 30:402–407.

[Fragner and Deiterding, 2017] Fragner, M. M. and Deiterding, R. (2017). Investigating side-wind stability of high speed trains using high resolution large eddy simulations and hybrid models. In Diez, P., Neittaanmäki, P., Periaux, J., Tuovinen, T., and Bräysy, O., editors, *Computational Methods in Applied Sciences*, volume 45, pages 223–241. Springer.

[Giordano et al., 2005] Giordano, J., Jourdan, G., Burtschell, Y., Medale, M., Zeitoun, D. E., and Houas, L. (2005). Shock wave impacts on deforming panel, an application of fluid-structure interaction. *Shock Waves*, 14(1-2):103–110.

[Laurence and Deiterding, 2011] Laurence, S. J. and Deiterding, R. (2011). Shock-wave surfing. *J. Fluid Mech.*, 676:369–431.

[Laurence et al., 2007] Laurence, S. J., Deiterding, R., and Hornung, H. G. (2007). Proximal bodies in hypersonic flows. *J. Fluid Mech.*, 590:209–237.

[Luccioni et al., 2004] Luccioni, B. M., Ambrosini, R. D., and Danesi, R. F. (2004). Analysis of building collapse under blast loads. *Engineering & Structures*, 26:63–71.

[Mader, 1979] Mader, C. L. (1979). *Numerical modeling of detonations*. University of California Press, Berkeley and Los Angeles, California.

References II

[Mauch, 2003] Mauch, S. P. (2003). *Efficient Algorithms for Solving Static Hamilton-Jacobi Equations*. PhD thesis, California Institute of Technology.

[Sethian, 1999] Sethian, J. A. (1999). *Level set methods and fast marching methods*. Cambridge University Press, Cambridge, New York.

[Specht, 2000] Specht, U. (2000). *Numerische Simulation mechanischer Wellen an Fluid-Festkörper-Mediengrenzen*. Number 398 in VDI Reihe 7. VDU Verlag, Düsseldorf.

[Zonglin et al., 2002] Zonglin, J., Matsuoka, K., Sasoh, A., and Takayama, K. (2002). Numerical and experimental investigation of wave dynamics processes in high-speed train/tunnels. *Chinese Journal of Mechanics Press*, 18(3):210–226.

Aerodynamics and fluid-structure interaction simulation with AMROC Part II

Ralf Deiterding

Aerodynamics and Flight Mechanics Research Group
University of Southampton
Highfield Campus
Southampton SO17 1BJ, UK
Email: r.deiterding@soton.ac.uk

Xiamen
24th July, 2019

Outline

Adaptive lattice Boltzmann method
- Construction principles
- Verification and validation
- Thermal LBM

Large-eddy simulation
- LES models
- Verification for homogeneous isotropic turbulence

Realistic aerodynamics computations
- Vehicle geometries
- Wind turbine benchmark
- Wake interaction prediction

Non-Cartesian lattice Boltzmann method
- Construction principles
- Verification and validation for 2d cylinder

Summary
- Conclusions

Approximation of Boltzmann equation

Is based on solving the Boltzmann equation with a simplified collision operator

$$\partial_t f + \mathbf{u} \cdot \nabla f = \omega(f^{eq} - f)$$

- $\mathrm{Kn} = l_f / L \ll 1$, where l_f is replaced with Δx
- Weak compressibilty and small Mach number assumed
- Assume a simplified phase space

Equation is approximated with a splitting approach.

1.) Transport step solves $\partial_t f_\alpha + \mathbf{e}_\alpha \cdot \nabla f_\alpha = 0$

Operator: $\mathcal{T}$: $\tilde{f}_\alpha(\mathbf{x} + \mathbf{e}_\alpha \Delta t, t + \Delta t) = f_\alpha(\mathbf{x}, t)$

$$\rho(\mathbf{x}, t) = \sum_{\alpha=0}^{18} f_\alpha(\mathbf{x}, t), \quad \rho(\mathbf{x}, t) u_i(\mathbf{x}, t) = \sum_{\alpha=0}^{18} \mathbf{e}_{\alpha i} f_\alpha(\mathbf{x}, t)$$

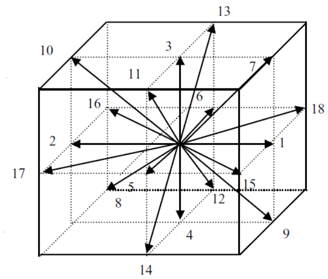

Discrete velocities:

$$\mathbf{e}_\alpha = \begin{cases} 0, & \alpha = 0, \\ (\pm 1, 0, 0)c, (0, \pm 1, 0)c, (0, 0, \pm 1)c, & \alpha = 1, \ldots, 6, \\ (\pm 1, \pm 1, 0)c, (\pm 1, 0, \pm 1)c, (0, \pm 1, \pm 1)c, & \alpha = 7, \ldots, 18, \end{cases}$$

Approximation of equilibrium state

2.) Collision step solves $\partial_t f_\alpha = \omega(f_\alpha^{eq} - f_\alpha)$
Operator $\mathcal{C}$:

$$f_\alpha(\cdot, t+\Delta t) = \tilde{f}_\alpha(\cdot, t+\Delta t) + \omega_L \Delta t \left(\tilde{f}_\alpha^{eq}(\cdot, t+\Delta t) - \tilde{f}_\alpha(\cdot, t+\Delta t) \right)$$

with equilibrium function

$$f_\alpha^{eq}(\rho, \mathbf{u}) = \rho t_\alpha \left[1 + \frac{3\mathbf{e}_\alpha \mathbf{u}}{c^2} + \frac{9(\mathbf{e}_\alpha \mathbf{u})^2}{2c^4} - \frac{3\mathbf{u}^2}{2c^2} \right]$$

with $t_\alpha = \frac{1}{9}\left\{3, \frac{1}{2}, \frac{1}{2}, \frac{1}{2}, \frac{1}{2}, \frac{1}{2}, \frac{1}{2}, \frac{1}{4}, \frac{1}{4}, \frac{1}{4}, \frac{1}{4}, \frac{1}{4}, \frac{1}{4}, \frac{1}{4}, \frac{1}{4}, \frac{1}{4}, \frac{1}{4}, \frac{1}{4}, \frac{1}{4}, \right\}$
Pressure $\delta p = \sum_\alpha f_\alpha^{eq} c_s^2 = \rho c_s^2$.
Dev. stress $\Sigma_{ij} = \left(1 - \frac{\omega_L \Delta t}{2}\right) \sum_\alpha \mathbf{e}_{\alpha i} \mathbf{e}_{\alpha j} (f_\alpha^{eq} - f_\alpha)$
Is derived by assuming a Maxwell-Boltzmann distribution of f_α^{eq} and approximating the involved exp() function with a Taylor series to second-order accuracy.
Using the third-order equilibrium function

$$f_\alpha^{eq}(\rho, \mathbf{u}) = \rho t_\alpha \left[1 + \frac{3\mathbf{e}_\alpha \mathbf{u}}{c^2} + \frac{9(\mathbf{e}_\alpha \mathbf{u})^2}{2c^4} - \frac{3\mathbf{u}^2}{2c^2} + \frac{\mathbf{e}_\alpha \mathbf{u}}{3c^2}\left(\frac{9(\mathbf{e}_\alpha \mathbf{u})^2}{2c^4} - \frac{3\mathbf{u}^2}{2c^2} \right) \right]$$

allows higher flow velocities.

Relation to Navier-Stokes equations

Inserting a Chapman-Enskog expansion, that is,

$$f_\alpha = f_\alpha(0) + \epsilon f_\alpha(1) + \epsilon^2 f_\alpha(2) + \ldots$$

and using

$$\frac{\partial}{\partial t} = \epsilon \frac{\partial}{\partial t_1} + \epsilon^2 \frac{\partial}{\partial t_2} + \ldots, \qquad \nabla = \epsilon \nabla_1 + \epsilon^2 \nabla_2 + \ldots$$

into the LBM and summing over α one can show that the continuity and moment equations are recoverd to $O(\epsilon^2)$ [Hou et al., 1996]

$$\partial_t \rho + \nabla \cdot (\rho \mathbf{u}) = 0$$

$$\partial_t \mathbf{u} + \mathbf{u} \cdot \nabla \mathbf{u} = -\nabla p + \nu \nabla^2 \mathbf{u}$$

Kinematic viscosity and collision time are connected by

$$\nu = \frac{1}{3} \left(\frac{\tau_L}{\Delta t} - \frac{1}{2} \right) c \Delta x$$

from which one gets with $\sqrt{3} c_s = \frac{\Delta x}{\Delta t}$ [Hähnel, 2004]

$$\omega_L = \tau_L^{-1} = \frac{c_s^2}{\nu + \Delta t c_s^2 / 2}$$

Initial and boundary conditions

- Initial conditions are constructed as $f_\alpha^{eq}(\rho(t=0), \mathbf{u}(t=0))$

Boundary conditions (applied before streaming step)

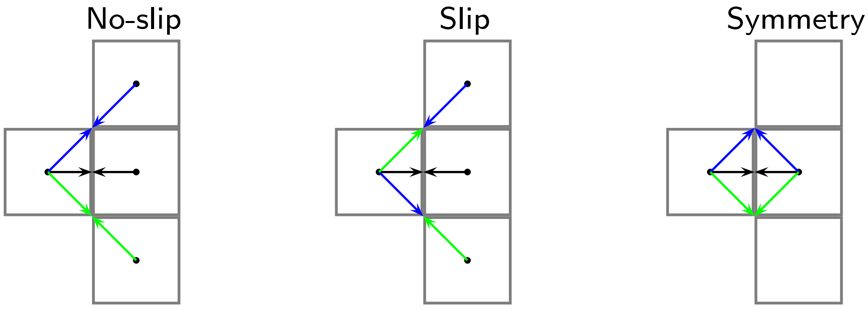

- Outlet basically copies all distributions (zero gradient)
- Inlet and pressure boundary conditions use f_α^{eq}

Complex geometry:

- Use level set method as before to construct macro-values in embedded boundary cells by interpolation / extrapolation [Deiterding, 2011].
- Distance function φ, normal $\mathbf{n} = \nabla\varphi/|\nabla\varphi|$. Triangulated meshes use CPT algorithm [Mauch, 2003].
- Construct macro-velocity in ghost cells for no-slip BC as $\mathbf{u}' = 2\mathbf{w} - \mathbf{u}$
- Then use $f_\alpha^{eq}(\rho', \mathbf{u}')$ or interpolated bounce-back [Bouzidi et al., 2001] to construct distributions in embedded ghost cells

Normalization

The method is implemented on the unit lattice with $\Delta\tilde{x} = \Delta\tilde{t} = 1$

$$\frac{\Delta x}{l_0} = 1, \quad \frac{\Delta t}{t_0} = 1 \longrightarrow c = 1$$

Lattice viscosity $\tilde{\nu} = \frac{1}{3}\left(\tau - \frac{1}{2}\right)$ and lattice sound speed $\tilde{c}_s = \frac{1}{\sqrt{3}}$ yield again

$$\omega_L = \frac{\tilde{c}_s^2}{\nu' + \tilde{c}_s^2/2} = \frac{c_s^2}{\nu + \Delta t c_s^2/2}$$

Velocity normalization factor: $u_0 = \frac{l_0}{t_0}$, density ρ_0

$$\mathrm{Re} = \frac{uL}{\nu} = \frac{u/u_0 \cdot l/l_0}{\nu/(u_0 l_0)} = \frac{\tilde{u}\tilde{l}}{\tilde{\nu}}$$

Trick for scheme acceleration: Use $\bar{u} = Su$ and $\bar{\nu} = S\nu$ which yields

$$\bar{\omega}_L = \frac{c_s^2}{S\nu + \Delta t/S\, c_s^2/2}$$

For instance, the physical hydrodynamic pressure is then obtained for a caloric gas as

$$p = (\tilde{\rho} - 1)\tilde{c}_s^2 \frac{u_0^2}{S^2}\rho_0 + \frac{c_s^2 \rho_0}{\gamma}$$

Adaptive LBM

1. Complete update on coarse grid: $f_\alpha^{C,n+1} := \mathcal{CT}(f_\alpha^{C,n})$
2. Interpolate $f_{\alpha,in}^{C,n}$ onto $f_{\alpha,in}^{f,n}$ to fill fine halos. Set physical boundary conditions.
3. $\tilde{f}_\alpha^{f,n} := \mathcal{T}(f_\alpha^{f,n})$ on whole fine mesh. $f_\alpha^{f,n+1/2} := \mathcal{C}(\tilde{f}_\alpha^{f,n})$ in interior.
4. $\tilde{f}_\alpha^{f,n+1/2} := \mathcal{T}(f_\alpha^{f,n+1/2})$ on whole fine mesh. $f_\alpha^{f,n+1} := \mathcal{C}(\tilde{f}_\alpha^{f,n+1/2})$ in interior.

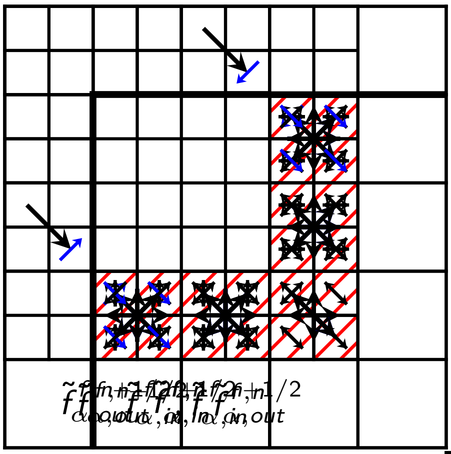

5. Average $\tilde{f}_{\alpha,out}^{f,n+1/2}$ (inner halo layer), $\tilde{f}_{\alpha,out}^{f,n}$ (outer halo layer) to obtain $\tilde{f}_{\alpha,out}^{C,n}$.
6. Revert transport into halos: $\bar{f}_{\alpha,out}^{C,n} := \mathcal{T}^{-1}(\tilde{f}_{\alpha,out}^{C,n})$
7. Parallel synchronization of $f_\alpha^{C,n}$, $\bar{f}_{\alpha,out}^{C,n}$
8. Cell-wise update where correction is needed: $f_\alpha^{C,n+1} := \mathcal{CT}(f_\alpha^{C,n}, \bar{f}_{\alpha,out}^{C,n})$

Algorithm equivalent to [Chen et al., 2006].

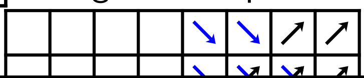

Flow over 2D cylinder, $d = 2\,\mathrm{cm}$

- Air with
  $\nu = 1.61 \cdot 10^{-5}\,\mathrm{m}^2/\mathrm{s}$,
  $\rho = 1.205\,\mathrm{kg}/\mathrm{m}^3$
- Domain size
  $[-8d, 24d] \times [-8d, 8d]$
- Dynamic refinement based on velocity. Last level to refine structure further.
- Inflow from left. Characteristic boundary conditions [Schlaffer, 2013] elsewhere.

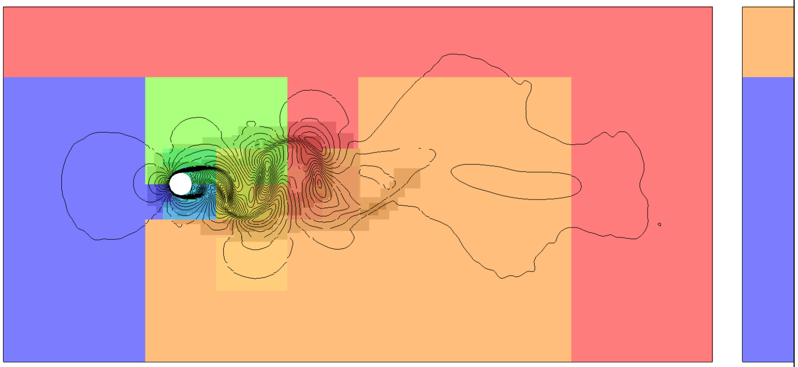

- Base lattice 320×160, 3 additional levels with factors $2, 4, 4$.
- Resolution: ~ 320 points in diameter d
- Computation of C_D on 400 equidistant points along circle and averaged over time. Comparison above with [Henderson, 1995].

Oscillating cylinder – Setup

Motion imposed on cylinder

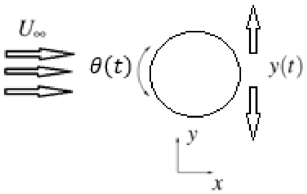

Case	A_t	$f_t = f_\theta$	V_R	U_∞	Re
1a	$D/4$	0.6	0.5	0.0606	1322
1b	$D/2$	0.6	1.0	0.0606	1322
2a	$D/4$	3.0	0.5	0.3030	6310
2b	$D/2$	3.0	1.0	0.3030	6310

$$y(t) = A_t \sin(2\pi f_t t), \qquad \theta(t) = A_\theta \sin(2\pi f_\theta t)$$

- Setup follows [Nazarinia et al., 2012]. Here $A_\theta = 1$ for all cases.
- Natural frequency of cylinder $f_N \approx 0.6154\,\mathrm{s}^{-1}$.
- Strouhal number $\mathrm{St}_t = f_t D/U_\infty \approx 0.198$ for all cases.
- Chosen here $D = 20\,\mathrm{mm}$
- Fluid is water with $c_s = 1482\,\mathrm{m/s}$, $\nu = 9.167 \cdot 10^{-7}\,\mathrm{m}^2/\mathrm{s}$, $\rho = 1016\,\mathrm{kg/m}^3$
- Constant coefficient model deactivated for Case 1, active for Case 2 with $C_{sm} = 0.2$

C. Laloglu, RD. Proc. 5th Int. Conf. on Parallel, Distributed, Grid and Cloud Computing for Engineering, Civil-Comp Press, 2017.

Case 1b, $V_R = 1$, $\mathrm{Re} = 1322$

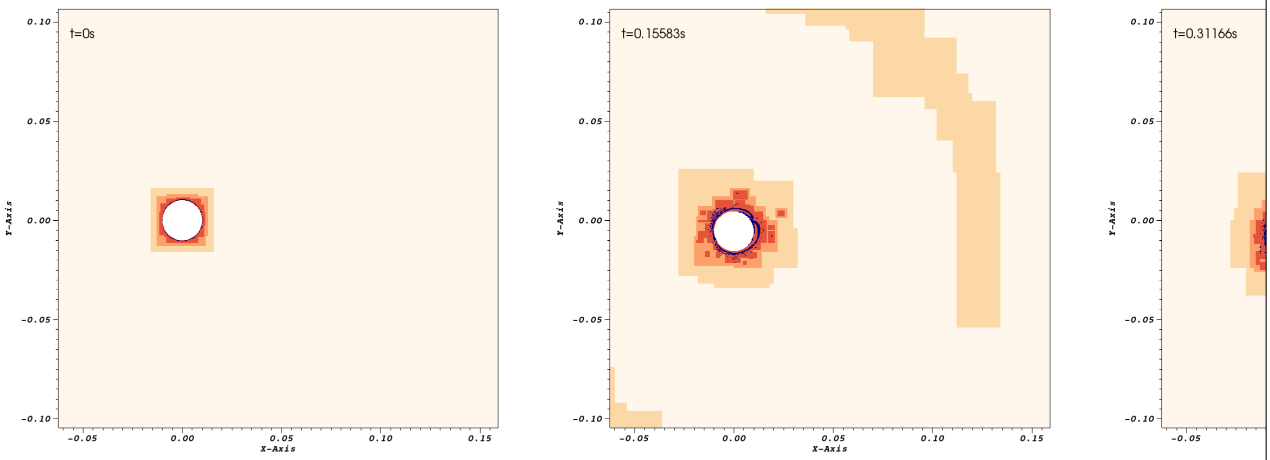

- Visualization enlargement of cylinder region
- Base mesh is discretized with 320×160 cells, 3 additional levels with factor $r_l = 2, 2, 2$
- 80 cells within D on highest level
- Speedup $S = 2000$
- Basically identical setup in commercial code XFlow for comparison

Case 1b, $V_R = 1$, $f_t = f_\theta = 0.6$, $\mathrm{Re} = 1322$

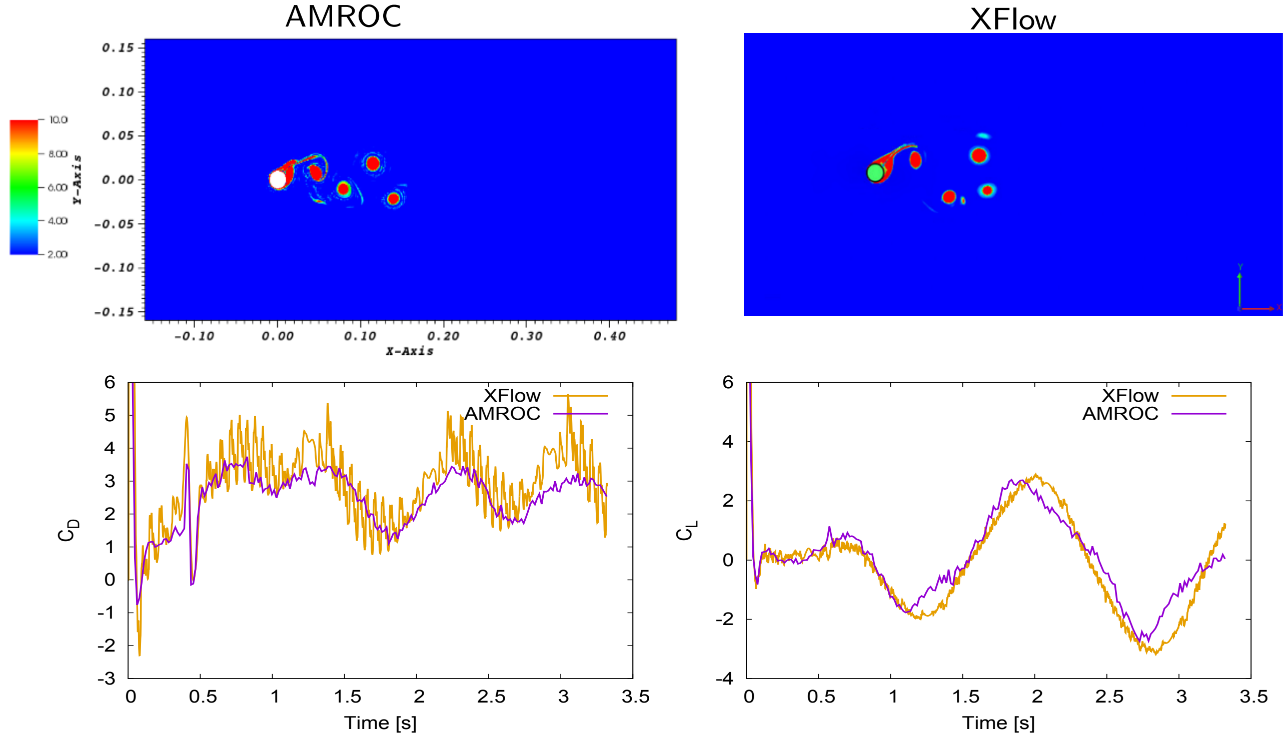

- Increase of rotational velocity leads to formation of a vortex pair plus single vortex. Drag and lift amplitude roughly doubled.
- Laminar results in good agreement with experiments of [Nazarinia et al., 2012].

Case 2a, $V_R = 0.5$, $f_t = f_\theta = 3$, $\mathrm{Re} = 6310$

AMROC

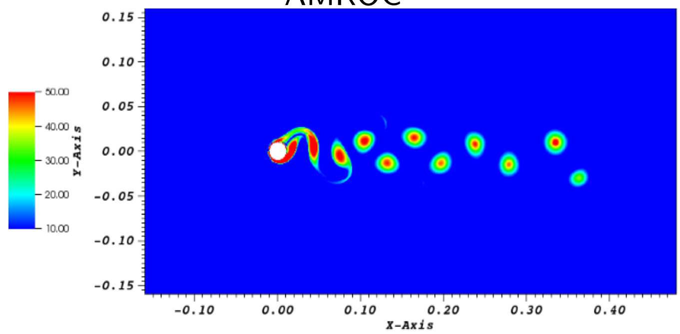

XFlow

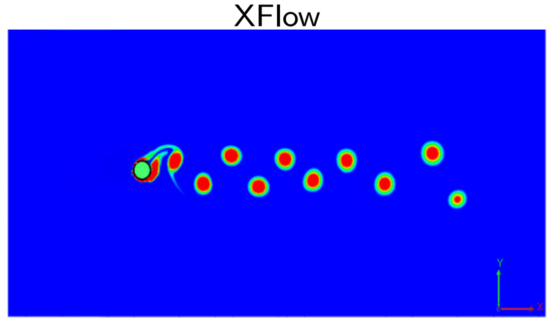

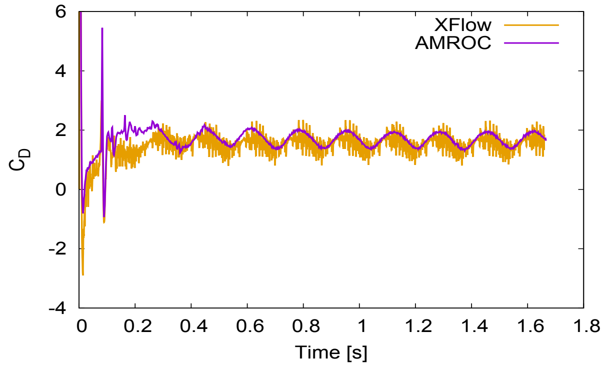

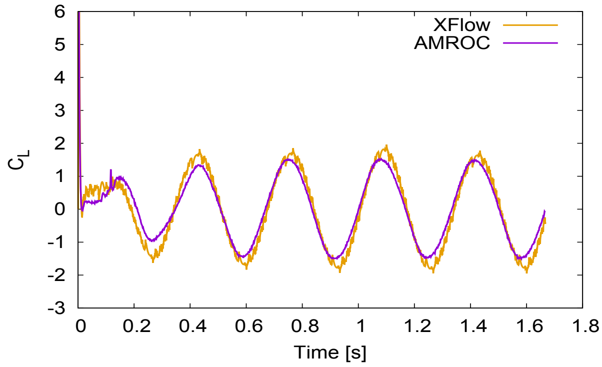

- Oscillation period: $T = 1/f_t = 0.33\,\mathrm{s}$. 10 regular vortices in $1.67\,\mathrm{s}$.
- CPU time on 6 cores for AMROC: $635.8\,s$, XFlow $\sim 50\,\%$ more expensive when normalized based on number of cells

Computational performance

Flow type	Case	Δt_0 [s]	Total cells		Δt_e [s]	Re	y^+	CPU time [s]	
			AMROC	XFlow				AMROC	XFlow
Laminar	**1a**	0.0015	85982	84778	3.33	1322	0	161.89	176
	1b	0.0015	91774	90488	3.33	1322	0	165.97	183
Turbulent	**2a**	0.00031	232840	216452	1.66	6310	2.4	635.8	887
	2b	0.00031	255582	246366	1.66	6310	2.6	933.2	1325

- Intel-Xeon-3.50-GHz desktop workstation with 6 cores, communication through MPI
- Same base mesh and always three additional refinement levels
- AMROC: single-relaxation time LBM, block-based mesh adaptation
- XFlow: slightly more multi-relaxation time LBM, cell-based mesh adaptation
- AMROC uses $\sim 7.5\,\%$ more cells on average more cells
- Normalized on cell number Case 2a is 50 % more expensive for XFlow than for AMROC-LBM
- Case 2b is 42 % more expensive in CPU time alone

Two-segment hinged wing

Configuration by [Toomey and Eldredge, 2008].
Manufactured bodies in tank filled with water.
Prescribed translation and rotation

$$X_t(t) = \frac{A_0}{2}\frac{G_t(ft)}{max\ Gt}C(ft), \quad \alpha_1(t) = -\beta\frac{G_r(ft)}{max\ Gr}$$

with $G_r(t) = tanh[\sigma_r cos(2\pi t + \Phi)]$,

$$G_t(t) = \int_t tanh[\sigma_t cos(2\pi t')]dt'$$

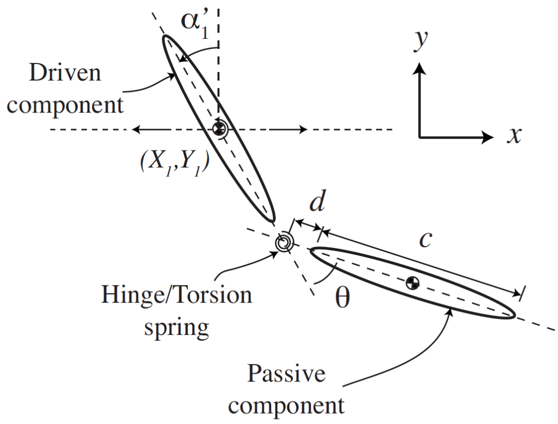

- 7 cases constructed by varying σ_r, σ_t, Φ
- Rotational Reynolds number $\mathrm{Re_r} = 2\pi\beta\sigma_r fc^2/(\tanh(\sigma_r)\nu)$ varied between 2200 and 7200 in experiments
- [Toomey and Eldredge, 2008] reference simulations with a viscous particle method are for $\mathrm{Re_r} = \{100, 500\}$

A_0 (cm)	7.1
c (cm)	5.1
d (cm)	0.25
$\rho_b\ (\mathrm{kg/m^3})$	5080
f (Hz)	0.15

Case 1 - $\sigma_r = \sigma_t = 0.628$, $\Phi = 0$, $\mathrm{Re}_r = 100$

- Quiescent water
  $\rho_f = 997\,\mathrm{kg/m^3}$
  $c_s = 1497\,\mathrm{m/s}$
- No-slip boundaries in y, periodic in x-direction
- Base level: 100×100 for $[-0.5, 0.5] \times [-0.5, 0.5]$ domain
- 4 additional levels with factors 2,2,2,4
- Coupling to rigid body motion solver on 4th level

Right: computed vorticity field (enlarged)

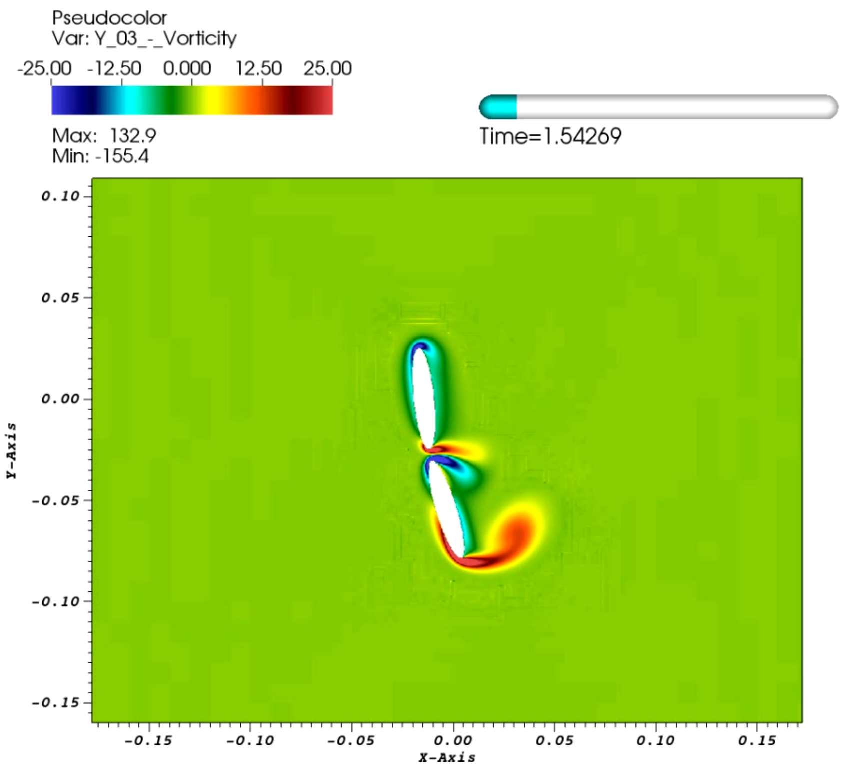

Quantitative comparison

- Evaluate normalized force $F_{x,y} = 2F^*_{x,y}/(\rho_f^2 c^3)$ and moment $M = 2M^*/(\rho_f f^2 c^4)$ over 3 periods
- [Wood and Deiterding, 2015] Used finest spatial resolution $\Delta x/c = 0.0122$
[Toomey and Eldredge, 2008]: $\Delta x/c = 0.013$ $(\mathrm{Re_r} = 100)$, $\Delta x/c = 0.0032$ $(\mathrm{Re_r} = 500)$
- Temporal resolution ~ 113 and ~ 28 times finer

Hinge deflection angle over time

Case 1
$\sigma_t = 0.628$
$\sigma_r = 0.628$
$\Phi = 0$

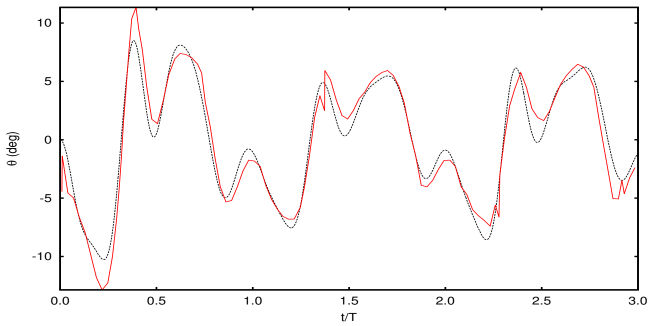

Case 2
$\sigma_t = 1.885$
$\sigma_r = 1.885$
$\Phi = 0^o$

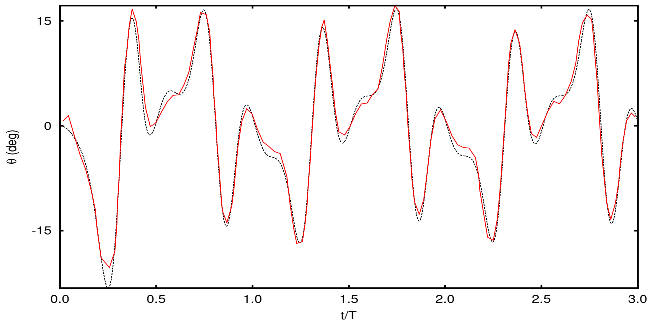

Experimental results (–); Current (- -)

An LBM for thermal transport

Consider the Navier-Stokes equations under Boussinesq approximation

$$\nabla \cdot \mathbf{u} = 0$$
$$\frac{\partial \mathbf{u}}{\partial t} + \nabla \cdot (\mathbf{u}\mathbf{u}) = -\nabla p + \nu \nabla^2 \mathbf{u} + \mathbf{F}$$
$$\frac{\partial T}{\partial t} + \nabla \cdot (\mathbf{u} T) = \mathcal{D} \nabla^2 T$$

with $\mathbf{F} = \mathbf{g}\beta\,(T - T_{ref})$.

An LBM for this system needs to use two distribution functions f_α and g_α.

1.) Transport step $\mathcal{T}$:

$$\tilde{f}_\alpha(\mathbf{x} + \mathbf{e}_\alpha \Delta t, t + \Delta t) = f_\alpha(\mathbf{x}, t), \quad \tilde{g}_\alpha(\mathbf{x} + \mathbf{e}_\alpha \Delta t, t + \Delta t) = g_\alpha(\mathbf{x}, t)$$

2.) Collision step $\mathcal{C}$:

$$f_\alpha(\cdot, t + \Delta t) = \tilde{f}_\alpha(\cdot, t + \Delta t) + \omega_{L,\nu} \Delta t \left(\tilde{f}_\alpha^{eq}(\cdot, t + \Delta t) - \tilde{f}_\alpha(\cdot, t + \Delta t) \right) + \Delta t \mathbf{F}_\alpha$$

$$g_\alpha(\cdot, t + \Delta t) = \tilde{g}_\alpha(\cdot, t + \Delta t) + \omega_{L,\mathcal{D}} \Delta t \left(\tilde{g}_\alpha^{eq}(\cdot, t + \Delta t) - \tilde{g}_\alpha(\cdot, t + \Delta t) \right)$$

with collision frequencies

$$\omega_{L,\nu} = \frac{c_s^2}{\nu + c_s^2 \Delta t/2}, \quad \omega_{L,\mathcal{D}} = \frac{\frac{3}{2} c_s^2}{\mathcal{D} + \frac{3}{2} c_s^2 \Delta t/2}$$

Equilibrium operators

This incompressible method uses in 2D [Guo et al., 2002]

$$f_\alpha^{(eq)} = \begin{cases} -4\sigma_0 p - s_\alpha(\mathbf{u}), & \text{for } \alpha = 0, \\ \sigma_\alpha p + s_\alpha(\mathbf{u}), & \text{for } \alpha = 1, \dots, 8, \end{cases}$$

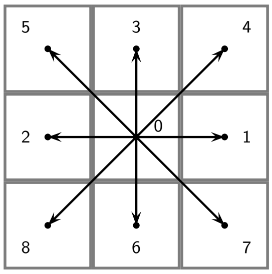

where

$$s_\alpha(\mathbf{u}) = t_\alpha \left[\frac{3\mathbf{e}_\alpha \mathbf{u}}{c^2} + \frac{9(\mathbf{e}_\alpha \mathbf{u})^2}{2c^4} - \frac{3\mathbf{u}^2}{2c^2} \right]$$

with $t_\alpha = \frac{1}{9}\left\{4, 1, 1, 1, \frac{1}{4}, \frac{1}{4}, 1, \frac{1}{4}, \frac{1}{4}\right\}$ and $\sigma_\alpha = \frac{1}{3}\left\{-5, 1, 1, 1, \frac{1}{4}, \frac{1}{4}, 1, \frac{1}{4}, \frac{1}{4}\right\}$

$$g_\alpha^{(eq)} = \frac{T}{4}\left[1 + 2\mathbf{e}_\alpha \cdot \mathbf{u}\right] \quad \text{for } \alpha = 1, \dots, 4$$

Forces are applied in y-direction only:

$$F_\alpha = \frac{1}{2}\left(\delta_{i3} - \delta_{i6}\right) \mathbf{e}_i \cdot \mathbf{F}$$

Moments: $\mathbf{u} = \sum_{\alpha > 0} \mathbf{e}_i f_\alpha, \quad p = \frac{1}{4\sigma}\left[\sum_{\alpha > 0} f_\alpha + s_0(\mathbf{u})\right], \quad T = \sum_{\alpha=1}^{4} g_\alpha$

Heated rotating cylinder

- $R = 15$, domain: $[-6R, 16R] \times [-8R, 8R]$
- $\mathrm{Re} = 2U_\infty R/\nu = 200$, $U_\infty = 0.01$
- Peripheral velocity $V = \Omega R$, $V/U_\infty = 0.5$
- Base grid 288×240 refined by three levels with $r_1 = 2$, $r_{2,3} = 4$ using scaled gradients of u, v, T

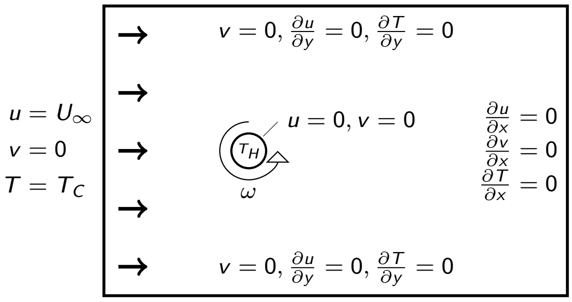

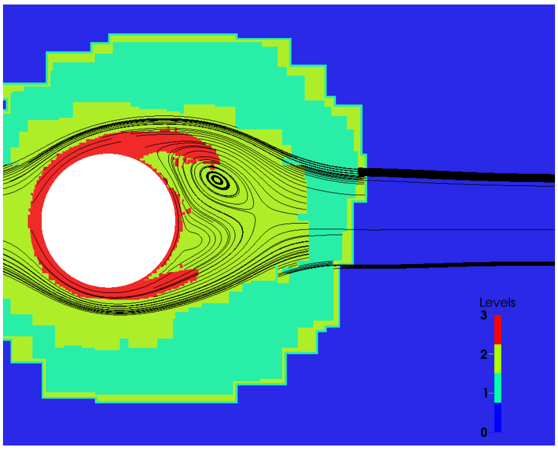

$t = 3$

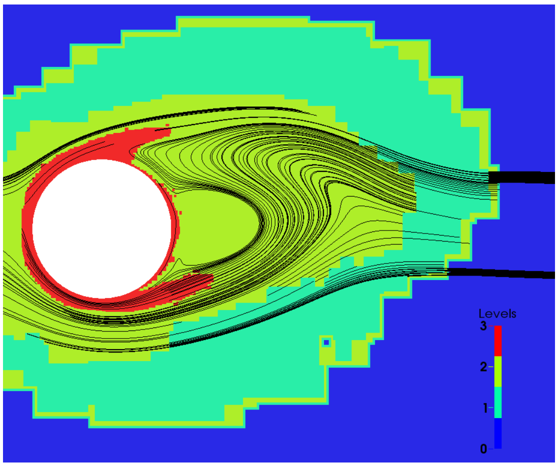

$t = 6$

Natural convection

Characterized by

$$\mathrm{Ra} = \frac{g\beta\Delta T H^3}{\nu\mathcal{D}}$$

a = AMROC-LBM,
b = [Fusegi et al., 1991] (NS - uniform)

	Ref.	$u_{\max}$	$y_{\max}$	$v_{\max}$	$x_{\max}$	$\mathrm{Nu}_{\mathrm{ave}}$
$\mathrm{Ra} = 10^3$	a	0.132	0.195	0.132	0.829	1.099
	b	0.131	0.200	0.132	0.833	1.105
$\mathrm{Ra} = 10^4$	a	0.197	0.194	0.220	0.887	2.270
	b	0.201	0.183	0.225	0.883	2.302
$\mathrm{Ra} = 10^5$	a	0.141	0.152	0.242	0.935	4.583
	b	0.147	0.145	0.247	0.935	4.646

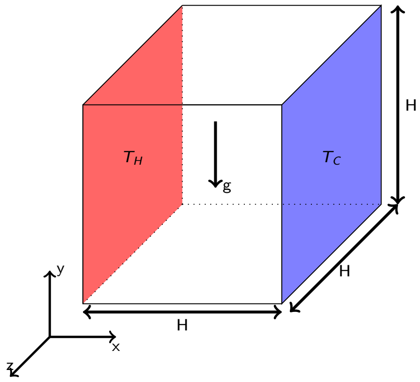

Isosurfaces of temperature and refinement levels

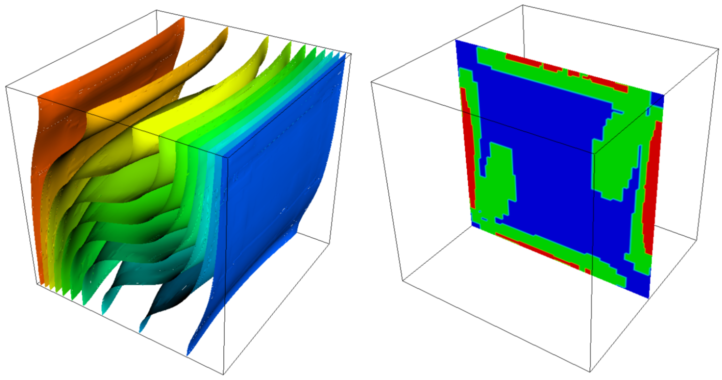

$\mathrm{Ra} = 10^4$

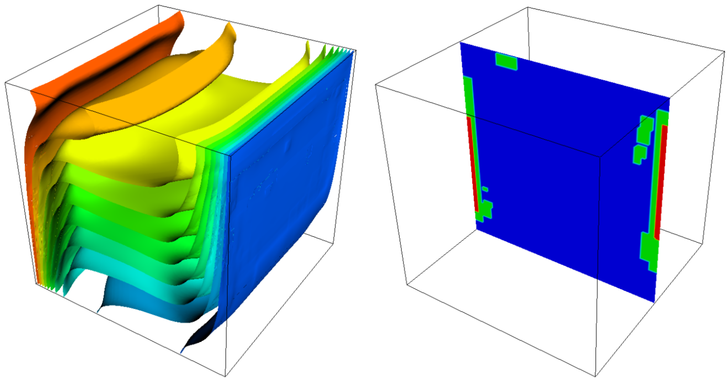

$\mathrm{Ra} = 10^5$

K. Feldhusen, RD, C. Wagner. J. Applied Math. Comp. Science 26(4): 735–747, 2016.

Turbulence modeling

Pursue a large-eddy simulation approach with $\bar{f}_\alpha$ and $\bar{f}^{eq}_\alpha$, i.e.

1.) $\tilde{\bar{f}}_\alpha(\mathbf{x}+\mathbf{e}_\alpha\Delta t, t+\Delta t) = \bar{f}_\alpha(\mathbf{x}, t)$

2.) $\bar{f}_\alpha(\cdot, t+\Delta t) = \tilde{\bar{f}}_\alpha(\cdot, t+\Delta t) + \frac{1}{\tau^\star}\Delta t\left(\tilde{\bar{f}}^{eq}_\alpha(\cdot, t+\Delta t) - \tilde{\bar{f}}_\alpha(\cdot, t+\Delta t)\right)$

Effective viscosity: $\nu^\star = \nu + \nu_t = \frac{1}{3}\left(\frac{\tau_L^\star}{\Delta t} - \frac{1}{2}\right) c\Delta x \quad \text{with} \quad \tau_L^\star = \tau_L + \tau_t$

Use Smagorinsky model to evaluate ν_t, e.g., $\nu_t = (C_{sm}\Delta x)^2|\bar{\mathbf{S}}|$, where

$$|\bar{\mathbf{S}}| = \sqrt{2\sum_{i,j}\bar{S}_{ij}\bar{S}_{ij}}$$

The filtered strain rate tensor $\bar{S}_{ij} = (\partial_j\bar{u}_i + \partial_i\bar{u}_j)/2$ can be computed as a second moment as

$$\bar{S}_{ij} = \frac{\bar{\Sigma}_{ij}}{2\rho c_s^2\tau_L^\star\left(1-\frac{\omega_L\Delta t}{2}\right)} = \frac{1}{2\rho c_s^2\tau_L^\star}\sum_\alpha e_{\alpha i}e_{\alpha j}(\bar{f}^{eq}_\alpha - \bar{f}_\alpha)$$

τ_t can be obtained as [Yu, 2004, Hou et al., 1996]

$$\tau_t = \frac{1}{2}\left(\sqrt{\tau_L^2 + 18\sqrt{2}(\rho_0 c^2)^{-1}C_{sm}^2\Delta x|\bar{\mathbf{S}}|} - \tau_L\right)$$

Further LES models

Dynamic Smagorinsky model (DSMA)

$$C_{sm}(\mathbf{x},t)^2 = -\frac{1}{2}\frac{\langle L_{ij}M_{ij}\rangle}{\langle M_{ij}M_{ij}\rangle}$$

$$L_{ij} = T_{ij} - \widehat{\tau}_{ij} = \widehat{\overline{u}_i\overline{u}_j} - \hat{\overline{u}}_i\hat{\overline{u}}_j \qquad M_{ij} = \widehat{\Delta x}^2|\hat{\overline{\mathbf{S}}}|\hat{\overline{S}}_{ij} - \Delta x^2\widehat{|\overline{\mathbf{S}}|\overline{S}_{ij}}$$

No van Driest damping implemented yet!

Wall-Adapting Local Eddy-viscosity model (WALE)

$$\nu_t = (C_w\Delta x)^2 OP_{WALE}, \quad \text{where } C_w = 0.5$$

WALE turbulence time-scale

$$OP_{WALE} = \frac{(\mathcal{J}_{ij}\mathcal{J}_{ij})^{\frac{3}{2}}}{(\overline{S}_{ij}\overline{S}_{ij})^{\frac{5}{2}} + (\mathcal{J}_{ij}\mathcal{J}_{ij})^{\frac{5}{4}}}$$

$$\mathcal{J}_{ij} = \overline{S}_{ik}\overline{S}_{kj} + \overline{\Omega}_{ik}\overline{\Omega}_{kj} - \frac{1}{3}\delta_{ij}(\overline{S}_{mn}\overline{S}_{mn} - \overline{\Omega}_{mn}\overline{\Omega}_{mn})$$

Effective relaxation time (see previous slide): $\tau_L^\star = \dfrac{(\nu+\nu_t) + \Delta t c_s^2/2}{c_s^2}$

Forced homogeneous isotropic turbulence

- Fourier representation
- Periodic boundaries, uniform mesh
- Use of external forcing term, i.e., result independent of initial conditions

Iso-surface $||\mathbf{u}||/\langle u_{rms}\rangle = 2$

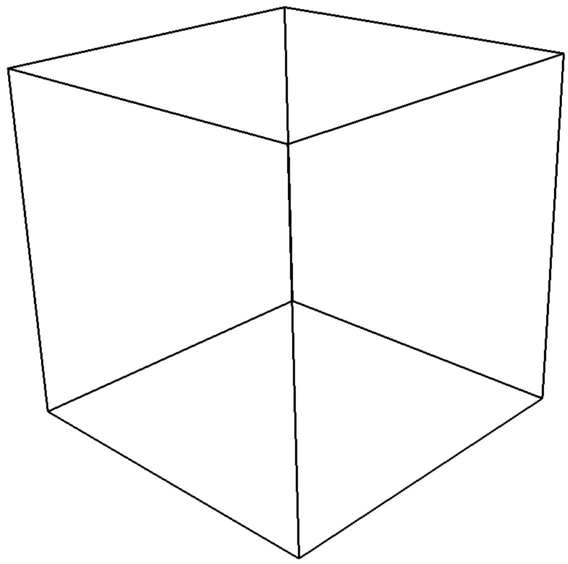

Forcing:

$$F_x = 2A\left(\frac{\kappa_y \kappa_z}{|\kappa|^2}\right) G(\kappa_x, \kappa_y, \kappa_z)$$

$$F_y = -A\left(\frac{\kappa_x \kappa_z}{|\kappa|^2}\right) G(\kappa_x, \kappa_y, \kappa_z)$$

$$F_z = -A\left(\frac{\kappa_x \kappa_y}{|\kappa|^2}\right) G(\kappa_x, \kappa_y, \kappa_z)$$

with phase
$G(\kappa_x, \kappa_y, \kappa_z) = \sin\left(\frac{2\pi x}{L}\kappa_x + \frac{2\pi y}{L}\kappa_y + \frac{2\pi z}{L}\kappa_z + \phi\right)$ for $(0 < \kappa_i \leq 2)$ and ϕ being a random phase value.

Comparison with model spectrum

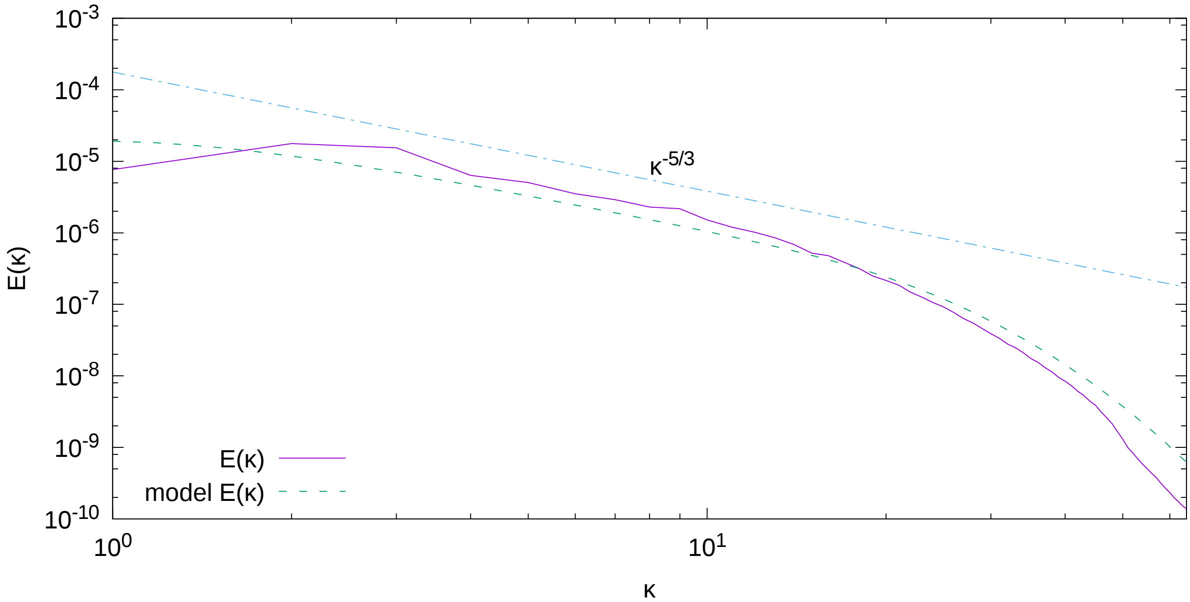

Time-averaged energy spectrum (solid line) [$N = 128^3$ cells, $\nu = 3e^{-5}\ \mathrm{m}^2/\mathrm{s}$] against a modelled one (dashed line and the -5/3 power law (dot-dashed line).

LES model spectra

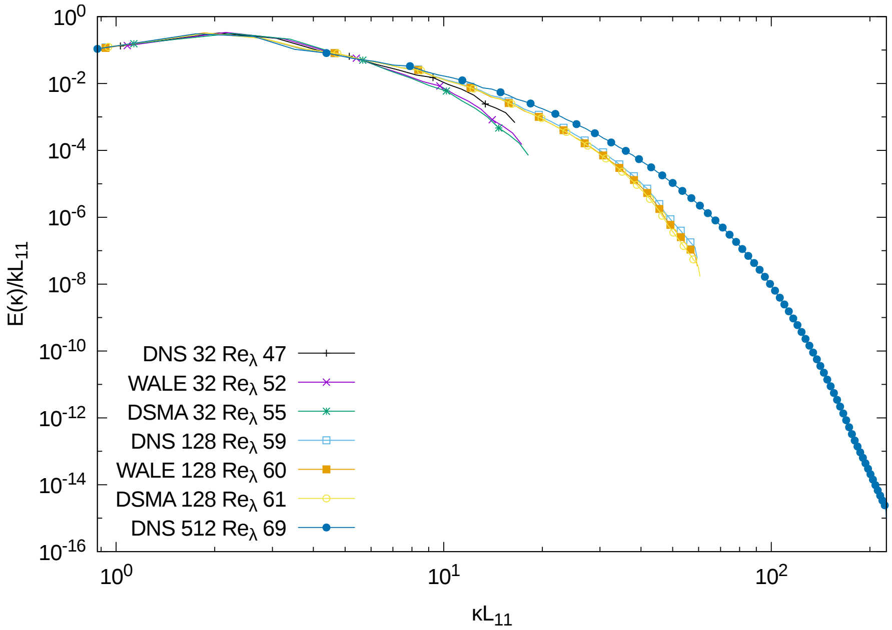

Time-averaged energy spectra normalised by the turbulent kinetic energy k and the integral length scale L_{11} of LBM DNS and LES for two resolutions and DNS of the highest resolution for the viscosity value $\nu = 5 \cdot 10^{-5}$

Decaying homogeneous isotropic turbulence

- Restart DNS of 512^3 resolution without forcing. Volume-averaging to 128^3 cells gives DSMA and WALE initial conditions

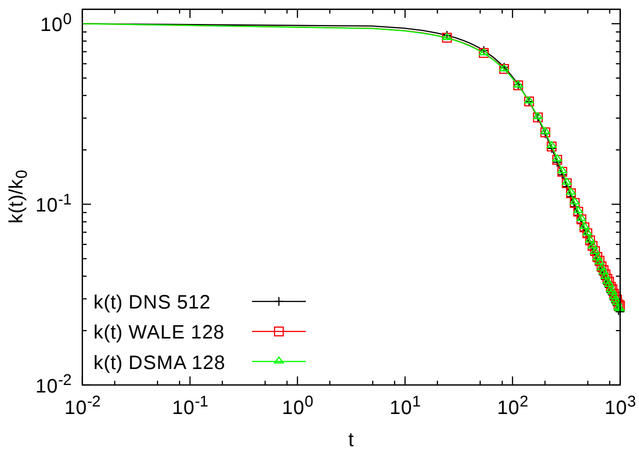

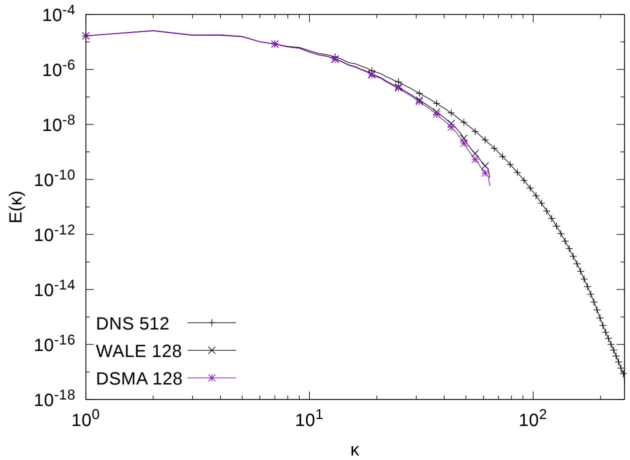

Evolution of the turbulent kinetic energy k (left) and energy spectra at $t = 68.72$ (right) for DNS of 512^3 against DSMA and WALE of 128^3 cells resolution.

Flow field comparison

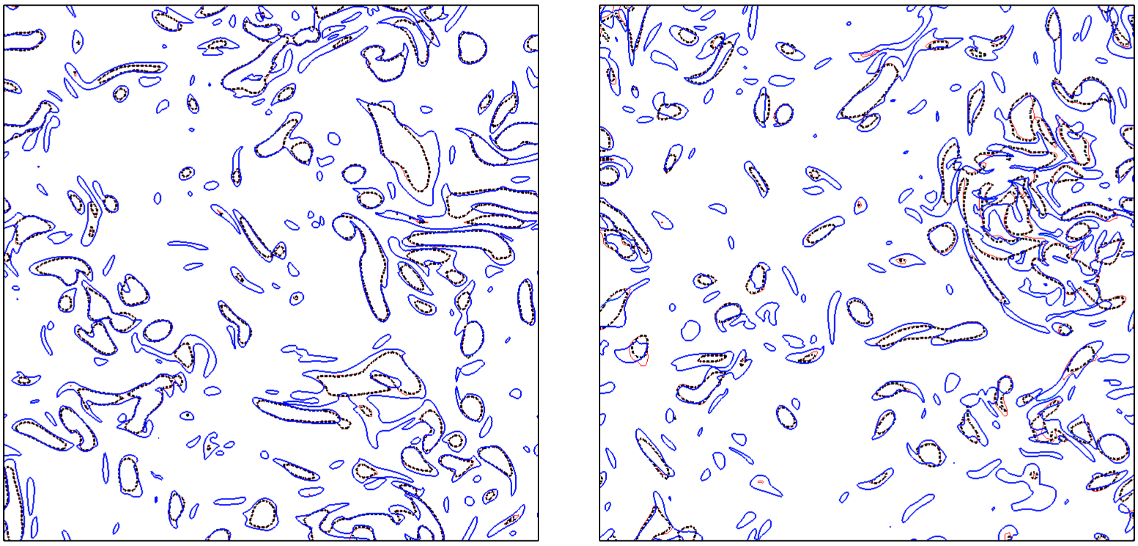

Contours of vorticity magnitude ($|\omega| = 0.18$) at $t = 4.91$ (left) and $t = 68.72$ (right) for DNS (thin blue lines) of 512^3 against DSMA (dotted black lines) and WALE (thick red lines) of 128^3 cells resolution

Outline

Adaptive lattice Boltzmann method
Construction principles
Verification and validation
Thermal LBM

Large-eddy simulation
LES models
Verification for homogeneous isotropic turbulence

Realistic aerodynamics computations
Vehicle geometries
Wind turbine benchmark
Wake interaction prediction

Non-Cartesian lattice Boltzmann method
Construction principles
Verification and validation for 2d cylinder

Summary
Conclusions

Wind tunnel simulation of a prototype car

Fluid velocity and pressure on vehicle

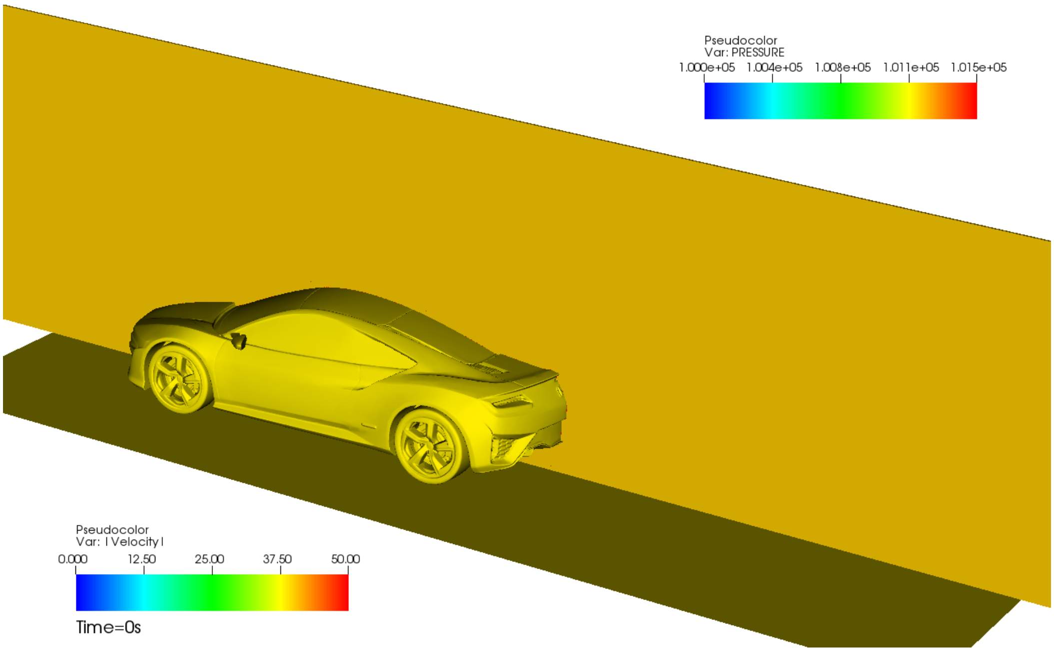

- Inflow 40 $\mathrm{m/s}$. LES model active. Characteristic boundary conditions.
- To $t = 0.5\,\mathrm{s}$ ($\sim$ 4 characteristic lengths) with 31,416 time steps on finest level in $\sim 37\,\mathrm{h}$ on 200 cores (7389 h CPU). Channel: $15\,\mathrm{m} \times 5\,\mathrm{m} \times 3.3\,\mathrm{m}$

Mesh adaptation

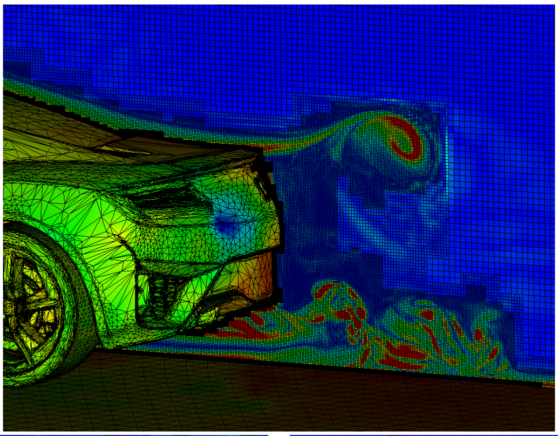

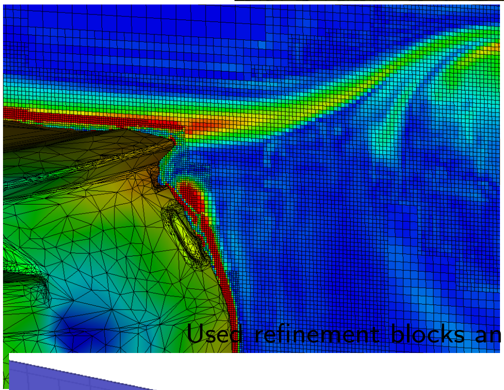

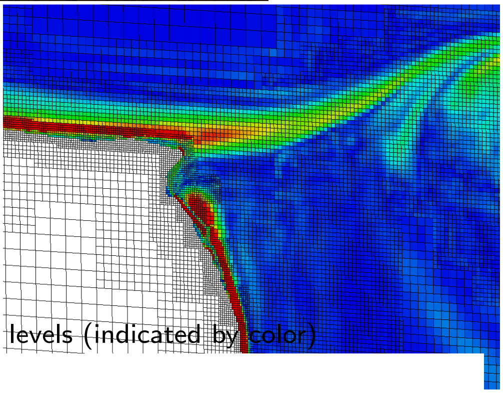

Used refinement blocks and levels (indicated by color)

Flow over a motorcycle

- Inflow $40\,\mathrm{m/s}$. Bouzidi pressure boundary conditions at outflows. CSMA LES model active.
- SAMR base grid $200 \times 80 \times 80$ cells, $r_{1,2,3} = 2$ yielding finest resolution of $\Delta x = 6.25\,\mathrm{mm}$. 23560 time steps on finest level
- Forces in AMROC-LBM are time-averaged over interval $[0.5\mathrm{s}, 1\mathrm{s}]$
- Unstructured STAR-CCM+ mesh has significantly finer as well as coarser cells

AMROC-LBM LES at $t = 1\,\mathrm{s}$

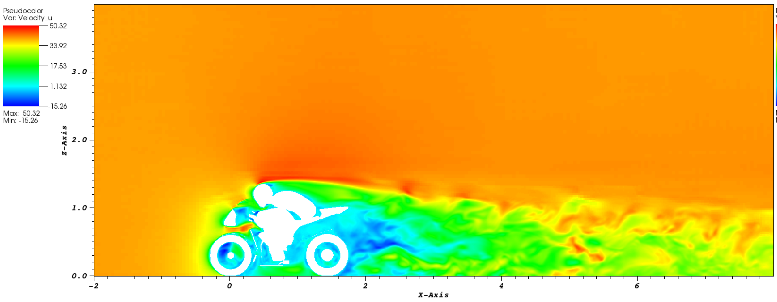

STAR-CCM+ steady RANS

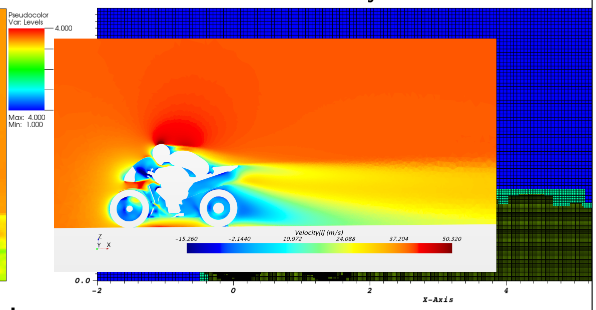

Velocity in flow direction

Variables	Forces (N) Drag	Sideforce	Lift	Total	Cores	Wall Time h	CPU Time h
STAR-CCM+	297	5	9	297	10	4.9	78
AMROC	297	10	23	298	64	10	635

Mexico experimental turbine – 0^o inflow

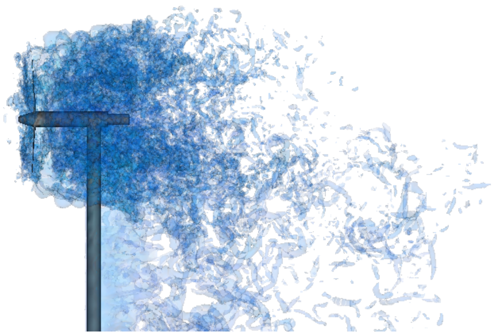

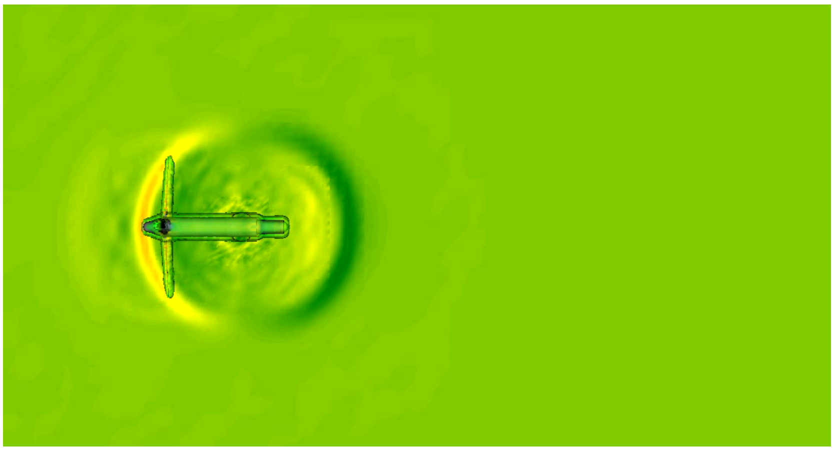

- Setup and measurements by Energy Research Centre of the Netherlands (ECN) and the Technical University of Denmark (DTU) [Schepers and Boorsma, 2012]
- Inflow velocity 14.93 $\mathrm{m/s}$ in wind tunnel of 9.5 m $\times$ 9.5 m cross section.
- Rotor diameter $D = 4.5\,\mathrm{m}$. Prescribed motion with 424.5 rpm: tip speed 100 $\mathrm{m/s}$, $\mathrm{Re}_r \approx 75839$ TSR 6.70
- Simulation with three additional levels with factors 2, 2, 4. Resolution of rotor and tower $\Delta x = 1.6\,\mathrm{cm}$
- 149.5 h on 120 cores Intel-Xeon (17490 h CPU) for 10 s
- Data collected as average during $t \in [5, 10]$. Load on blade 1 as it passes through $\theta = 0^o$ (pointing vertically upwards), 35 rotations

Mexico experimental turbine – 30^o yaw

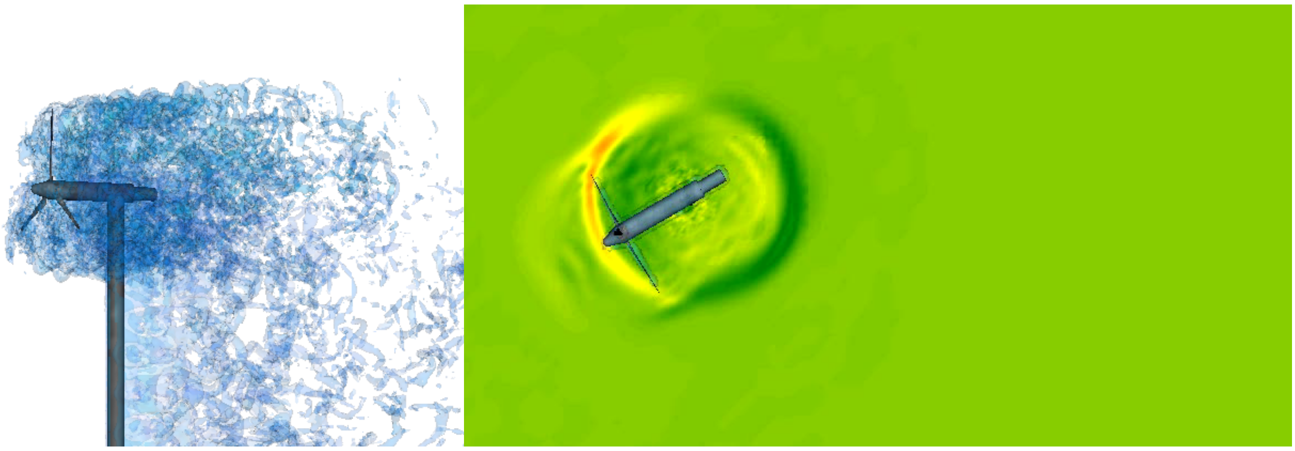

- 157.6 h on 120 cores Intel-Xeon for 10 s (70.75 revolutions) $\longrightarrow$ $\sim$ 22.25 h CPU/1M cells/revolution
- $\sim$ 12 M cells in total – level 0: 768,000, level 1: $\sim$ 1.5 M, level 2: $\sim$ 6.8 M, level 3: $\sim$ 3.0 M
- For comparison [Schepers and Boorsma, 2012]:
- Wind Multi-Block Liverpool University (34 M cells): 209 h CPU/1M cells/revolution
- EllipSys3D (28.3 M cell mesh): $\sim$ 40.7 h CPU/1M cells/revolution, but $\sim$ 15% error in F_x and T_x already for 0° inflow [Sørensen et al., 2014]

Comparison along transects – 30^o yaw

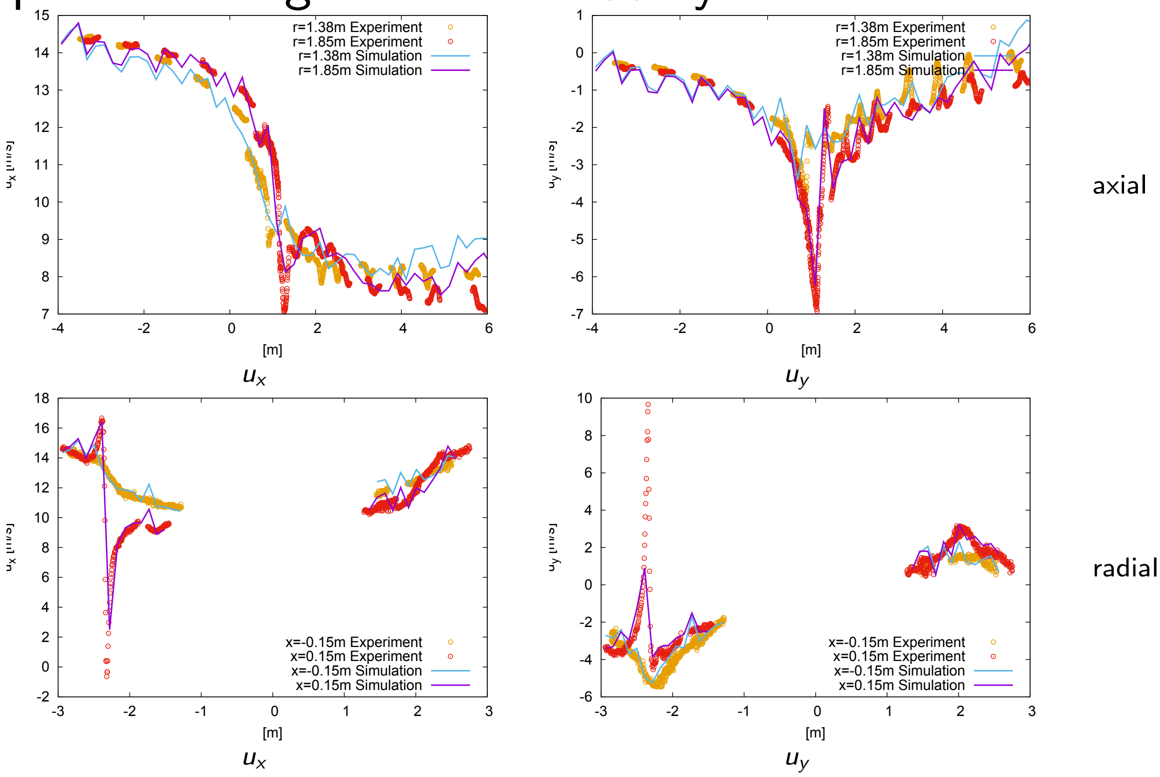

- Blade loads: F_x: $\mathrm{Ref} = 13.66\,\mathrm{N}$, $\mathrm{cur.} = 14.8\,\mathrm{N}$ (8.3%)
- T_x: $\mathrm{Ref} = 7.72\,\mathrm{Nm}$, $\mathrm{cur.} = 8.36\,\mathrm{Nm}$ (8.3%)

RD, S. L. Wood. Proc. of TORQUE 2016. *J. Phys. Conference Series* 753: 082005, 2016.

Single Vestas V27

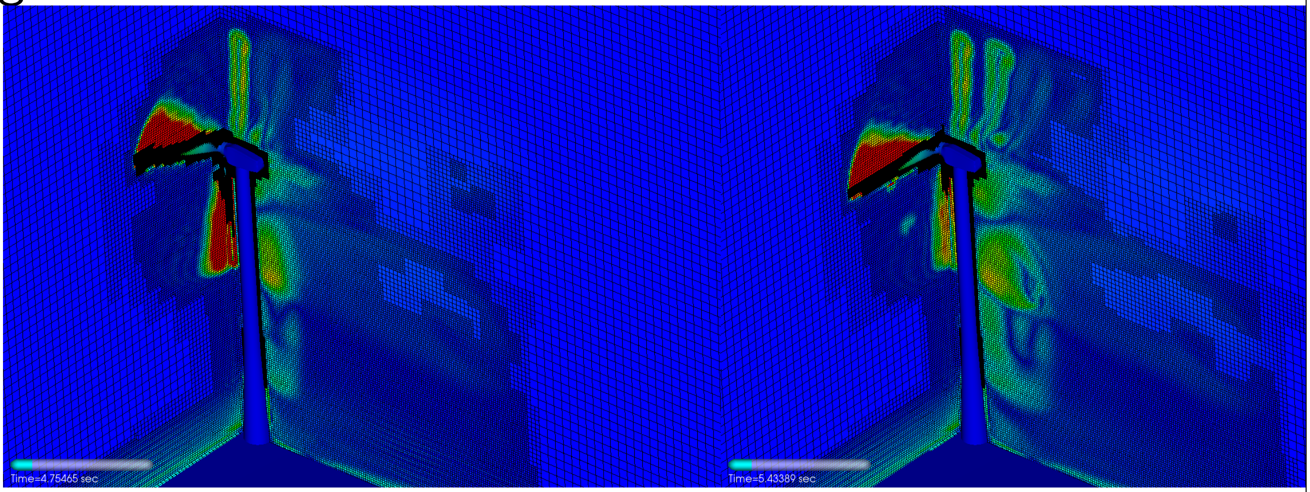

- Inflow velocity $u_\infty = 8\,\mathrm{m/s}$. Prescribed motion of rotor with $n_{\mathrm{rpm}} = 33$, $r = 14.5\,\mathrm{m}$: tip speed $46.7\,\mathrm{m/s}$, $\mathrm{Re}_r \approx 919,700$ TSR 5.84
- Simulation with three additional levels with refinement factors $2, 2, 4$.
- Refinement based on vorticity and level set.
- Sampled rotor and circular regions ($r_c = 1.5r$) every $0.034\,\mathrm{s}$ over $t = [8, 18]\,\mathrm{s}$
- Computing 84,806 highest level iterations to $t_e = 18\,\mathrm{s}$.
- $\sim$ 24 time steps for 1^o rotation

Simulation of the SWIFT array

- Three Vestas V27 turbines (geometric details prototypical). 225 kW power generation at wind speeds 14 to 25 $\mathrm{m/s}$ (then cut-off)
- Prescribed motion of rotor with 33 and 43 rpm. Inflow velocity 8 and 25 $\mathrm{m/s}$
- TSR: 5.84 and 2.43, $\mathrm{Re}_r \approx 919,700$ and 1,208,000
- Simulation domain 448 $\mathrm{m} \times$ 240 $\mathrm{m} \times 100\,\mathrm{m}$
- Base mesh 448 $\times$ 240 $\times$ 100 cells with refinement factors 2, 2,4. Resolution of rotor and tower $\Delta x = 6.25\,\mathrm{cm}$
- 94,224 highest level iterations to $t_e = 40\,\mathrm{s}$ computed, then statistics are gathered for 10 s [Deiterding and Wood, 2016]

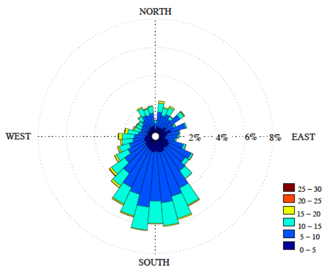

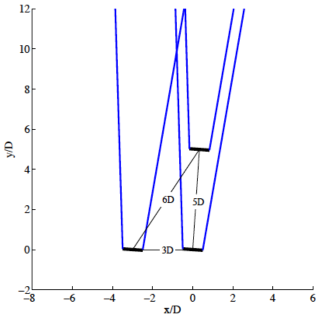

Vorticity – inflow at 30^o, $u = 8\,\mathrm{m/s}$, $33\,\mathrm{rpm}$

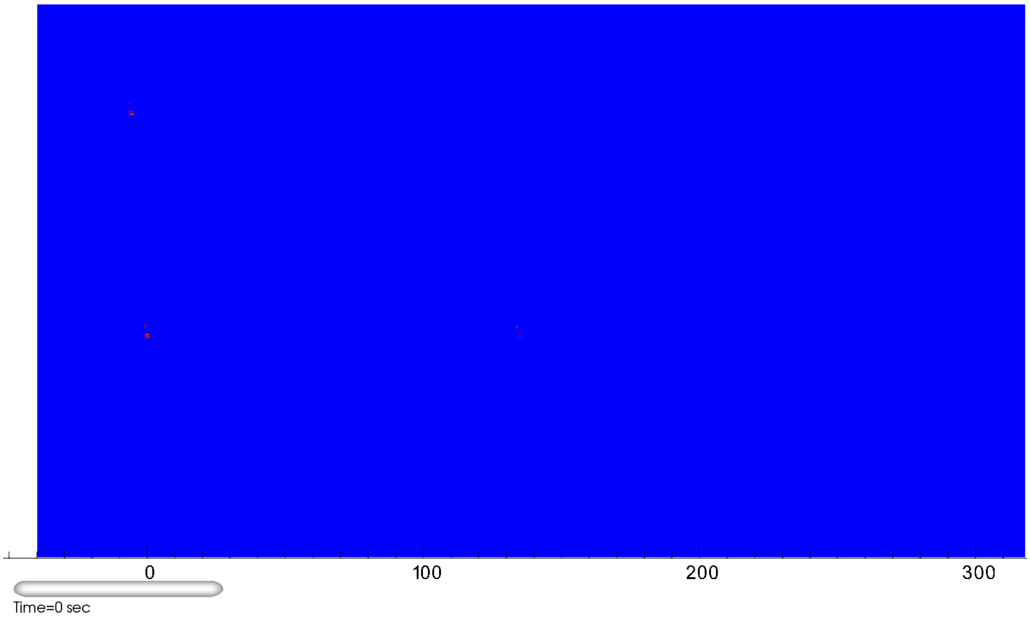

- Top view in plane in z-direction at $30\,\mathrm{m}$ (hub height)
- Turbine hub and inflow at 30^o yaw leads to off-axis wake impact.
- 160 cores Intel-Xeon E5 2.6 GHz, $33.03\,\mathrm{h}$ wall time for interval $[50, 60]\,\mathrm{s}$ (including gathering of statistical data)
- $\sim 6.01\,\mathrm{h}$ per revolution ($961\,\mathrm{h}$ CPU) $\longrightarrow \sim 5.74\,\mathrm{h}$ CPU/1M cells/revolution

Levels – inflow at 30^o, $u = 8\,\mathrm{m/s}$, $33\,\mathrm{rpm}$

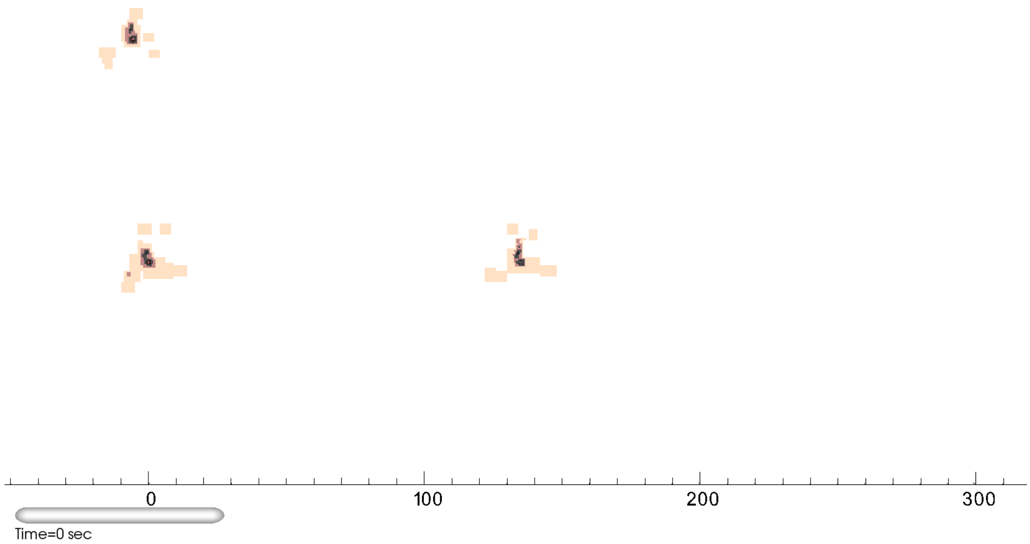

- At $63.8\,\mathrm{s}$ approximately 167M cells used vs. 44 billion (factor 264)
- $\sim 6.01\,\mathrm{h}$ per revolution ($961\,\mathrm{h}$ CPU) $\longrightarrow \sim 5.74\,\mathrm{h}$ CPU/1M cells/revolution

Level	Grids	Cells
0	2,463	10,752,000
1	6,464	20,674,760
2	39,473	131,018,832
3	827	4,909,632

Vorticity development – inflow at 0^o, $u = 8\,\mathrm{m/s}$, $33\,\mathrm{rpm}$

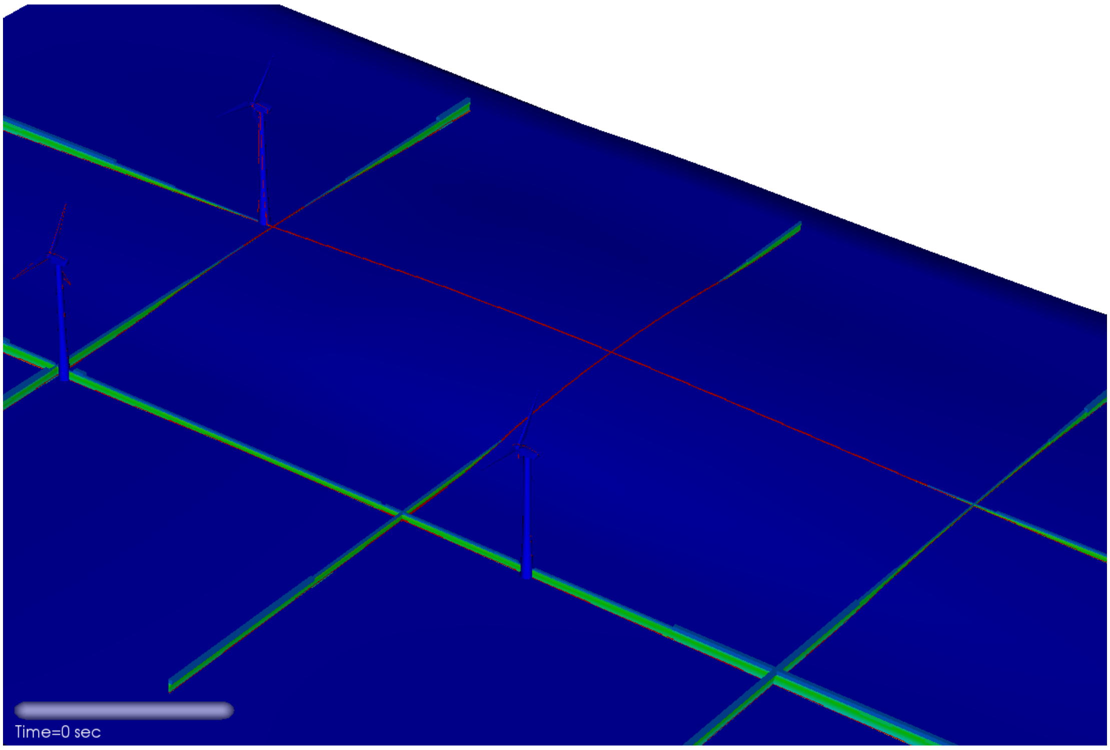

- Refinement of wake up to level 2 ($\Delta x = 25\,\mathrm{cm}$).
- Vortex break-up before 2nd turbine is reached.

Refinement – inflow at 0^o, $u = 8\,\mathrm{m/s}$, $33\,\mathrm{rpm}$

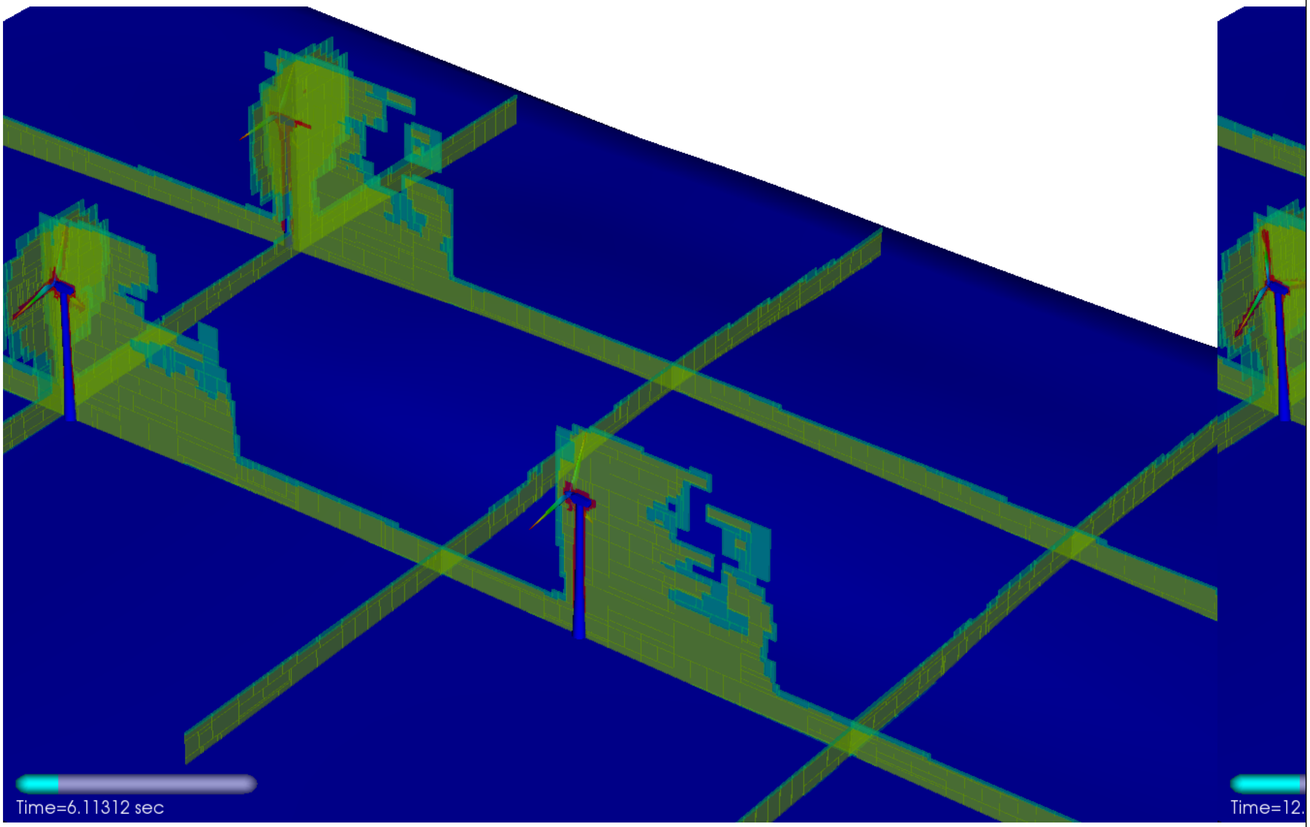

Mean point values – inflow at 0^o,

- Turbines located at $(0, 0, 0)$, $(135, 0, 0)$, $(-5.65, 80.80, 0)$
- Lines of 13 sensors with $\Delta y = 5\,\mathrm{m}$, $z = 37\,\mathrm{m}$ (approx. center of rotor)
- u and p measured over $[40\,\mathrm{s}, 50\,\mathrm{s}]$ (1472 level-0 time steps) and averaged

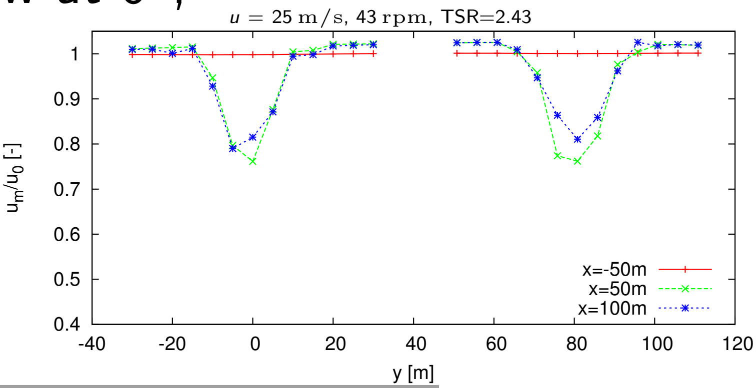

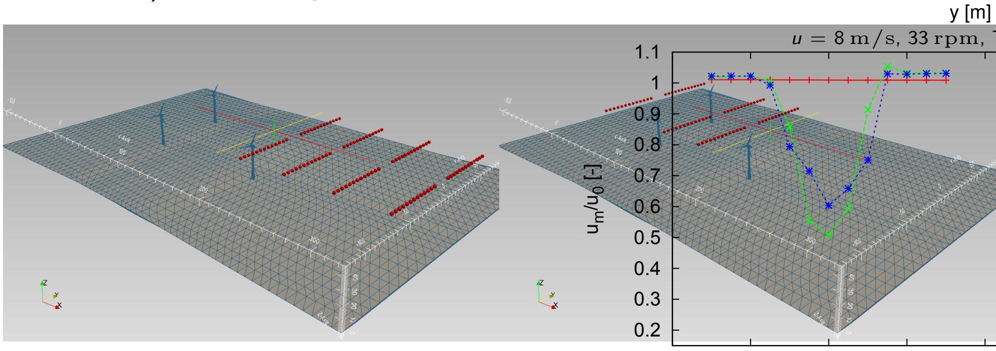

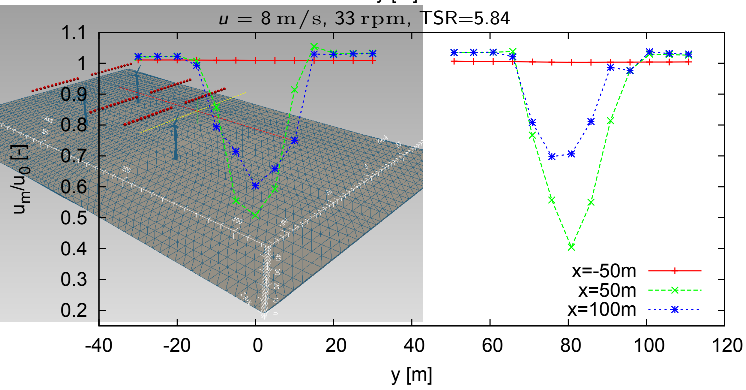

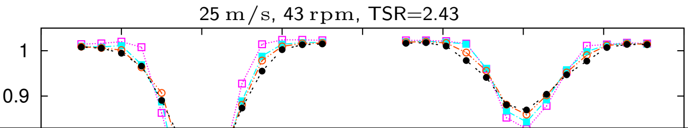

Lattice Boltzmann equation in mapped coordinates

Consider mapping from Cartesian to non-Cartesian coordinates

$$\xi = \xi(x,y),\ \eta = \eta(x,y)$$

with

$$\frac{\partial}{\partial x} = \frac{\partial}{\partial \xi}\frac{\partial \xi}{\partial x} + \frac{\partial}{\partial \eta}\frac{\partial \eta}{\partial x},\ \frac{\partial}{\partial y} = \frac{\partial}{\partial \xi}\frac{\partial \xi}{\partial y} + \frac{\partial}{\partial \eta}\frac{\partial \eta}{\partial y}.$$

Under this transformation the convection term reads

$$\begin{aligned}
\mathbf{e}_\alpha \cdot \nabla f_\alpha &= e_{\alpha x}\frac{\partial f_\alpha}{\partial x} + e_{\alpha y}\frac{\partial f_\alpha}{\partial y} \\
&= e_{\alpha x}\left(\frac{\partial f_\alpha}{\partial \xi}\frac{\partial \xi}{\partial x} + \frac{\partial f_\alpha}{\partial \eta}\frac{\partial \eta}{\partial x}\right) + e_{\alpha y}\left(\frac{\partial f_\alpha}{\partial \xi}\frac{\partial \xi}{\partial y} + \frac{\partial f_\alpha}{\partial \eta}\frac{\partial \eta}{\partial y}\right) \\
&= \left(e_{\alpha x}\frac{\partial \xi}{\partial x} + e_{\alpha y}\frac{\partial \xi}{\partial y}\right)\frac{\partial f_\alpha}{\partial \xi} + \left(e_{\alpha x}\frac{\partial \eta}{\partial x} + e_{\alpha y}\frac{\partial \eta}{\partial y}\right)\frac{\partial f_\alpha}{\partial \eta} \\
&= \tilde{e}_{\alpha\xi}\frac{\partial f_\alpha}{\partial \xi} + \tilde{e}_{\alpha\eta}\frac{\partial f_\alpha}{\partial \eta},
\end{aligned}$$

and hence the lattice Boltzmann equation becomes

$$\frac{\partial f}{\partial t} + \tilde{e}_{\alpha\xi}\frac{\partial f_\alpha}{\partial \xi} + \tilde{e}_{\alpha\eta}\frac{\partial f_\alpha}{\partial \eta} = -\frac{1}{\tau}\left(f_\alpha - f_\alpha^{eq}\right).$$

Scheme construction

Currently using the explicit 4th-order Runge-Kutta scheme

$$f_\alpha^1 = f_\alpha^t,\ f_\alpha^2 = f_\alpha^1 + \frac{\Delta t}{4} R_\alpha^1,$$
$$f_\alpha^3 = f_\alpha^1 + \frac{\Delta t}{3} R_\alpha^2, f_\alpha^4 = f_\alpha^1 + \frac{\Delta t}{2} R_\alpha^3,$$
$$f_\alpha^{t+\Delta t} = f_\alpha^1 + \Delta t R_\alpha^4.$$

with

$$R_{\alpha(i,j)} = -\left(\tilde{e}_{\alpha\xi(i,j)} \frac{f_{\alpha(i+1,j)} - f_{\alpha(i-1,j)}}{2\Delta\xi} + \tilde{e}_{\alpha\eta(i,j)} \frac{f_{\alpha(i,j+1)} - f_{\alpha(i,j-1)}}{2\Delta\eta}\right) - \frac{1}{\tau}\left(f_{\alpha(i,j)} - f^{eq}_{\alpha(i,j)}\right)$$

for the solution, 2nd-order central differences to approximate derivatives.
A 4th-order dissipation term

$$D = -\epsilon \left((\Delta\xi)^4 \frac{\partial^4 f_\alpha}{\partial \xi^4} + (\Delta\eta)^4 \frac{\partial^4 f_\alpha}{\partial \eta^4} \right)$$

is added for stabilization [Hejranfar and Hajihassanpour, 2017].
Prototype implementation is presently on finite difference meshes!

2d cylinder study

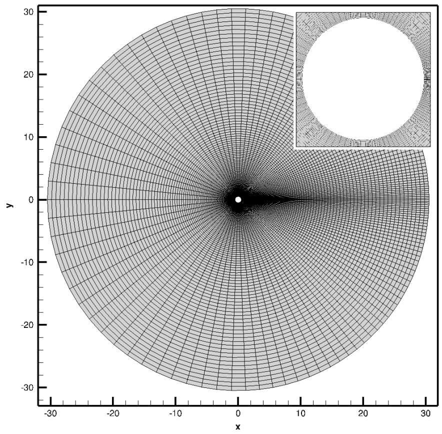

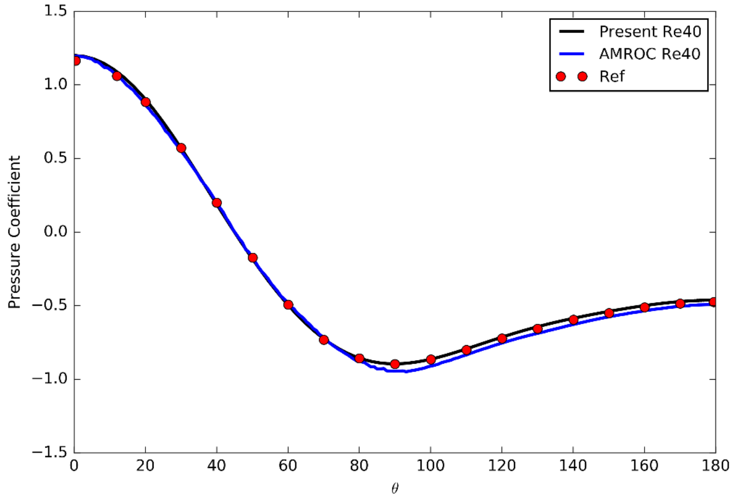

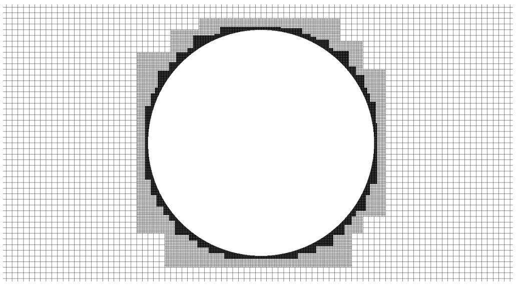

Re	Author(s)	C_d	$C_p(0)$	$C_p(180)$	$2L/D$
20	[Tritton, 1959]	2.20	-	-	-
	[Henderson, 1995]	2.06	-	-0.60	-
	[Dennis and Chang, 1970]	2.05	1.27	-0.58	1.88
	[Hejranfar and Ezzatneshan, 2014]	2.02	1.25	-0.59	1.84
	AMROC-LBM	1.98	1.26	-0.59	1.85
	Present	2.02	1.31	-0.55	1.85
40	[Tritton, 1959]	1.65	-	-	-
	[Henderson, 1995]	1.55	-	-0.53	-
	[Dennis and Chang, 1970]	1.52	1.14	-0.50	4.69
	[Hejranfar and Ezzatneshan, 2014]	1.51	1.15	-0.48	4.51
	AMROC-LBM	1.45	1.19	-0.49	4.66
	Present	1.51	1.19	-0.46	4.60

$2L/D$ is normalized length of wake behind cylinder

2d cylinder study – unsteady flow case

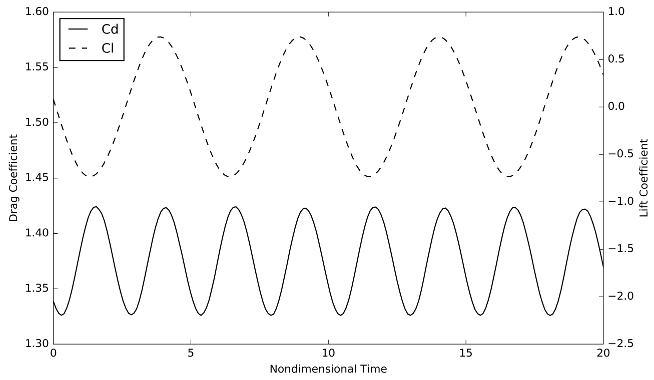

Re	Author(s)	St	$\overline{C_d}$	C_l'
100	[Chiu et al., 2010]	0.167	1.35	0.30
	AMROC-LBM	0.166	1.28	0.32
	Present	0.165	1.36	0.35
200	[Chiu et al., 2010]	0.198	1.37	0.71
	AMROC-LBM	0.196	1.26	0.70
	Present	0.196	1.37	0.73

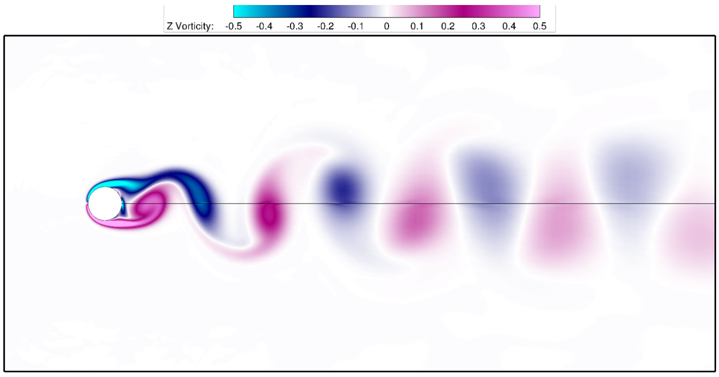

Re		CPU-time	Mesh
20	AMROC-LBM	24:55:21	297796
	Present	06:08:41	65536
40	AMROC-LBM	27:10:08	317732
	Present	05:57:17	65536
100	AMROC-LBM	113:15:37	1026116
	Present	05:58:49	65536
200	AMROC-LBM	130:37:18	1130212
	Present	06:03:42	65536

Conclusions – subsonic aerodynamics with LBM

- Cartesian LBM is a very efficient low-dissipation method for subsonic aerodynamic simulation and especially suitable for DNS and LES
- Cartesian CFD with block-based AMR is faster than cell-cased AMR and tailored for modern massively parallel computer systems
- Fast dynamic mesh adaptation in AMROC makes FSI problems with complex motion easily accessible. Time-explicit approach leads to very tight coupling
- For high Reynolds number flows around complex bodies an LES turbulence model is vital for stability (so are higher-order in- and outflow boundary conditions)
- Currently validating and extending (dynamic) Smagorinsky with wall-near damping and WALE model for realistic problems
- Turbulent wall function boundary condition model under development
- Accurate simulation of thin, wall-resolved boundary layers is dramatically more efficient with the non-Cartesian LBM approach, despite the availability of AMR in AMROC
  - Develop non-Cartesian version of AMROC-LBM as near-term goal
  - Chimera technique within AMROC-LBM might be long-term goal

References I

[Bouzidi et al., 2001] Bouzidi, M., Firdaouss, M., and Lallemand, P. (2001). Momentum transfer of a Boltzmann-lattice fluid with boundaries. *Physics of Fluids*, 13:3452.

[Chen et al., 2006] Chen, H., Filippova, O., Hoch, J., Molvig, K., Shock, R., Teixeira, C., and Zhang, R. (2006). Grid refinement in lattice Boltzmann methods based on volumetric formulation. *Physica A*, 362:158–167.

[Chiu et al., 2010] Chiu, P. H., Lin, R. K., and Sheu, T. W. (2010). A differentially interpolated direct forcing immersed boundary method for predicting incompressible Navier Stokes equations in time-varying complex geometries. *Journal of Computational Physics*.

[Deiterding, 2011] Deiterding, R. (2011). Block-structured adaptive mesh refinement - theory, implementation and application. *European Series in Applied and Industrial Mathematics: Proceedings*, 34:97–150.

[Deiterding and Wood, 2016] Deiterding, R. and Wood, S. L. (2016). An adaptive lattice Boltzmann method for predicting wake fields behind wind turbines. In Dillmann, A., Heller, G., Krämer, E., Wagner, C., and Breitsamter, C., editors, *New Results in Numerical and Experimental Fluid Mechanics X*, volume 132 of *Notes on Numerical Fluid Mechanics and Multidisciplinary Design*, pages 845–857. Springer.

[Dennis and Chang, 1970] Dennis, S. C. R. and Chang, G. (1970). Numerical solutions for steady flow past a circular cylinder at Reynolds numbers up to 100. *Journal of Fluid Mechanics*, 42(03):471.

[Fusegi et al., 1991] Fusegi, T., Hyun, J., Kuwahara, K., and Farouk, B. (1991). A numerical study of three-dimensional natural convection in a differentially heated cubical enclosure. *Int. J. Heat and Mass Transfer*, 34:1543–1557.

[Guo et al., 2002] Guo, Z., Shi, B., and Zheng, C. (2002). A coupled lattice BGK model for the Boussinesq equations. *Int. J. Numerical Methods in Fluids*, 39:325–342.

[Hähnel, 2004] Hähnel, D. (2004). *Molekulare Gasdynamik*. Springer.

[Hejranfar and Ezzatneshan, 2014] Hejranfar, K. and Ezzatneshan, E. (2014). Implementation of a high-order compact finite-difference lattice Boltzmann method in generalized curvilinear coordinates. *Journal of Computational Physics*, 267:28–49.

[Hejranfar and Hajihassanpour, 2017] Hejranfar, K. and Hajihassanpour, M. (2017). Chebyshev collocation spectral lattice Boltzmann method in generalized curvilinear coordinates. *Computers and Fluids*.

References II

[Henderson, 1995] Henderson, R. D. (1995). Details of the drag curve near the onset of vortex shedding. *Phys. Fluids*, 7:2102–2104.

[Hou et al., 1996] Hou, S., Sterling, J., Chen, S., and Doolen, G. D. (1996). A lattice Boltzmann subgrid model for high Reynolds number flows. In Lawniczak, A. T. and Kapral, R., editors, *Pattern formation and lattice gas automata*, volume 6, pages 151–166. Fields Inst Comm.

[Mauch, 2003] Mauch, S. P. (2003). *Efficient Algorithms for Solving Static Hamilton-Jacobi Equations*. PhD thesis, California Institute of Technology.

[Nazarinia et al., 2012] Nazarinia, M., Jacono, D. L., Thompson, M. C., and Sheridan, J. (2012). Flow over a cylinder subjected to combined translational and rotational oscillations. *J. Fluids and Structures*, 32:135–145.

[Schepers and Boorsma, 2012] Schepers, J. G. and Boorsma, K. (2012). Final report of iea task 29: Mexnext (phase 1) – Analysis of Mexico wind tunnel measurements. Technical Report ECN-E-12-004, European research Centre of the Netherlands.

[Schlaffer, 2013] Schlaffer, M. B. (2013). *Non-reflecting boundary conditions for the lattice Boltzmann method*. PhD thesis, Technical University Munich.

[Sørensen et al., 2014] Sørensen, N. N., Bechmann, A., Rethore, P. E., and Zahle, F. (2014). Near wake reynolds-averaged Navier-Stokes predictions of the wake behind the MEXICO rotor in axial and yawed flow conditions. *Wind Energy*, 17:75–86.

[Toomey and Eldredge, 2008] Toomey, J. and Eldredge, J. D. (2008). Numerical and experimental study of the fluid dynamics of a flapping wing with low order flexibility. *Physics of Fluids*, 20(7):073603.

[Tritton, 1959] Tritton, D. (1959). Experiments on the flow past a circular cylinder at low Reynolds numbers. *Journal of Fluid Mechanics*, 6(4):547–567.

[Tsai, 1999] Tsai, L. (1999). *Robot Analysis: The Mechanics of Serial and Parallel Manipulators*. Wiley.

[Wood and Deiterding, 2015] Wood, S. L. and Deiterding, R. (2015). A lattice Boltzmann method for horizontal axis wind turbine simulation. In *14th Int. Conf. on Wind Engineering*.

[Yu, 2004] Yu, H. (2004). *Lattice Boltzmann equation simulations of turbulence, mixing, and combustion*. PhD thesis, Texas A&M University.

Motion solver

Based on the Newton-Euler method solution of dynamics equation of kinetic chains [Tsai, 1999]

$$\begin{pmatrix} \mathbf{F} \\ \boldsymbol{\tau}_\mathrm{P} \end{pmatrix} = \begin{pmatrix} m\mathbf{1} & -m[\mathbf{c}]^\times \\ m[\mathbf{c}]^\times \mathbf{I}_\mathrm{cm} & -m[\mathbf{c}]^\times[\mathbf{c}]^\times \end{pmatrix} \begin{pmatrix} \mathbf{a}_\mathrm{P} \\ \boldsymbol{\alpha} \end{pmatrix} + \begin{pmatrix} m[\boldsymbol{\omega}]^\times[\boldsymbol{\omega}]^\times \mathbf{c} \\ [\boldsymbol{\omega}]^\times(\mathbf{I}_\mathrm{cm} - m[\mathbf{c}]^\times[\mathbf{c}]^\times)\,\boldsymbol{\omega} \end{pmatrix}.$$

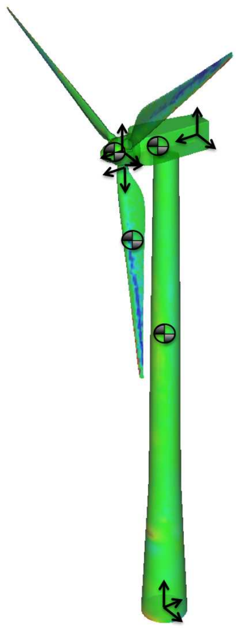

m = mass of the body, 1 = the 4×4 homogeneous identity matrix,
$\mathbf{a}_p$ = acceleration of link frame with origin at $\mathbf{p}$ in the preceding link's frame,
$\mathbf{I}_\mathrm{cm}$ = moment of inertia about the center of mass,
$\boldsymbol{\omega}$ = angular velocity of the body,
$\boldsymbol{\alpha}$ = angular acceleration of the body,
$\mathbf{c}$ is the location of the body's center of mass,
and $[\mathbf{c}]^\times$, $[\boldsymbol{\omega}]^\times$ denote skew-symmetric cross product matrices.

Here, we additionally define the total force and torque acting on a body,
$\mathbf{F} = (\mathbf{F}_{FSI} + \mathbf{F}_{prescribed}) \cdot \mathcal{C}_{xyz}$ and

$\tau = (\tau_{FSI} + \tau_{prescribed}) \cdot \mathcal{C}_{\alpha\beta\gamma}$ respectively.

Where $\mathcal{C}_{xyz}$ and $\mathcal{C}_{\alpha\beta\gamma}$ are the translational and rotational constraints, respectively.